

MEASUREMENT OF DRELL–YAN LONGITUDINAL DOUBLE SPIN
ASYMMETRY IN POLARIZED $p + p$ COLLISIONS AT PHENIX

BY

Gonaduwage Darshana Nadeeshan Perera, B.S., M.S.

A dissertation submitted to the Graduate School

in partial fulfillment of the requirements

for the degree

Doctor of Philosophy

Major Subject: Physics

New Mexico State University

Las Cruces New Mexico

May 2016

“Measurement of Drell-Yan Longitudinal Double Spin Asymmetry in Polarized $p + p$ Collisions at PHENIX,” a dissertation prepared by Gonaduwage Darshana Nadeeshan Perera in partial fulfillment of the requirements for the degree, Doctor of Philosophy, has been approved and accepted by the following:

Loui Reyes
Dean of the Graduate School

Stephen Pate
Chair of the Examining Committee

Date

Committee in charge:

Dr. Stephen Pate, Chair

Dr. Igor Vasiliev

Dr. Michael Engelhardt

Dr. Xiaorong Wang

Dr. David Voelz

ACKNOWLEDGMENTS

First and foremost, I would like to thank my adviser, Dr. Stephen Pate for his continued support during the entire period of my degree program at New Mexico State University. His encouragement, patience, guidance and the time he spent on teaching me were extremely invaluable.

I would like to give my special thanks to Dr. Jin Huang for inspiring me by giving his creative ideas and helping me to solve many problems in data analysis. I think this is the best opportunity to thank everyone in the NMSU nuclear physics group and everyone I worked with in PHENIX for their inputs and help. I am grateful to Nalin Fernando and other friends who helped me in numerous ways during my period of study. I would also like to thank my panel of committee members, Dr. Xiaorong Wang, Dr. Igor Vasiliev, Dr. Michael Engelhardt and Dr. David Voelz for spending their valuable time in evaluating my study.

I can not express in words, how grateful I am to my mother Mallika Abeytrathna and father Dharmaratna Perera for all of the sacrifices that they have made to bring me to this caliber. Further I would like to thank my sister, Kanchna Perera for her words of encouragement which always lifted my spirits. Finally, I would like to thank my wife Nadeepa Jayasundara for her endless love and encouragement throughout this entire journey without whom I would have struggled to find the inspiration and motivation needed to complete this dissertation.

ABSTRACT

MEASUREMENT OF DRELL-YAN LONGITUDINAL DOUBLE SPIN

ASYMMETRY IN POLARIZED $p + p$ COLLISIONS AT PHENIX

BY

Gonaduwage Darshana Nadeeshan Perera, B.S., M.S.

Doctor of Philosophy

New Mexico State University

Las Cruces, New Mexico, 2016

Dr. Stephen Pate, Chair

Analysis of the Drell-Yan process in high energy polarized proton-proton collisions is a unique method for probing the proton spin structure. Measurement of the longitudinal double spin asymmetry (A_{LL}) in the Drell-Yan process provides clean access to the anti-quark helicity distributions without involving quark fragmentation functions. In the PHENIX experiment at RHIC, the Forward Silicon Vertex Detector (FVTX), together with forward muon spectrometers, allows us to study the Drell-Yan process by detecting the muon pairs in the forward region ($1.2 < \eta < 2.4$) while also suppressing backgrounds due to heavy-flavor production. In

this thesis the Drell-Yan A_{LL} measurement for the intermediate mass region ($4.5 \text{ GeV} < M < 8 \text{ GeV}$) using the RHIC 2013 data of proton-proton collisions at a center of mass energy of 510 GeV is presented.

CONTENTS

1	INTRODUCTION	1
1.1	The Standard Model	2
1.2	Historical overview of the nucleon structure	6
1.3	Spin structure of the nucleon	14
1.3.1	Spin Puzzle	16
1.3.2	Semi Inclusive Deep Inelastic Scattering (SIDIS)	18
1.3.3	Hadron collider experiments	19
1.3.4	Spin asymmetry	20
1.3.5	Current sea quark polarization measurements	21
1.4	The Drell-Yan process in proton-proton collisions	24
1.5	Overview of the analysis	28
2	EXPERIMENT SETUP AT PHENIX	29
2.1	RHIC	29
2.1.1	Polarized Ion Source and Accelerator Complex	30
2.1.2	Siberian Snakes and Spin Rotators	32
2.1.3	Polarimetry	34
2.2	PHENIX	40
2.2.1	PHENIX magnets	44

2.2.2	Global detectors	45
2.2.3	Central arm detectors	50
2.2.4	Forward arm detectors	51
2.2.5	Data acquisition (DAQ) and triggering	54
3	FORWARD VERTEX SILICON DETECTOR (FVTX)	60
3.1	Detector overview	61
3.2	Detector components and their functionality	62
3.2.1	Wedges	62
3.2.2	Disks and Cages	65
3.3	FVTX data acquisition system	67
3.3.1	Read Out Card (ROC)	68
3.3.2	Front End Module (FEM)	70
3.4	Tracking	70
3.5	Tracklets for Drell-Yan analysis	74
4	DATA AND SIMULATIONS	78
4.1	Beam polarization and the integrated luminosity	79
4.2	Dimuon spectrum	82
4.3	Quality assurance (QA)	82
4.4	Simulation	84
5	MEASUREMENT OF DRELL-YAN SIGNAL FRACTION	87
5.1	Basic event selection criteria	88

5.2	Distance of closest approach (DCA) Method	89
5.3	Signal fraction from Tracklets Vs. Mass 2-D distributions	92
5.3.1	Template functions	94
5.3.2	Template fitting	100
5.3.3	Monte Carlo test results	106
5.4	Tracklets Vs. Transverse Momentum 2-D template functions . . .	109
5.4.1	Template functions	109
5.4.2	Template fitting	115
5.5	Drell-Yan signal fraction	119
6	MEASUREMENT OF DRELL-YAN A_{LL}	120
6.1	Signal and background fractions	121
6.2	Measuring longitudinal double spin asymmetry	124
6.2.1	Inclusive double spin asymmetry	124
6.2.2	Drell-Yan A_{LL}	128
6.3	Systematic uncertainty and final results	133
7	DISCUSSION AND CONCLUSIONS	136
	REFERENCES	138

LIST OF TABLES

1.1	Variables used in DIS	8
2.1	Some RHIC machine parameters for Run 13	32
3.1	Summary of design parameters	62
4.1	Spin patterns in RHIC Run 2013	80
4.2	Spin patterns in RHIC Run 2013	80
4.3	Bad Run list from FVTX QA	84
4.4	Bad Run list from Spin QA	84
4.5	Total integrated luminosity produced for each simulated sub-processes using reference run 393888.	85
5.1	Constant coefficients of template functions determined from likeli- hood fitting for north arm (for tracklets vs. mass case).	99
5.2	Constant coefficients of template functions determined from likeli- hood fitting for south arm (for tracklets vs. mass case).	99
5.3	Number of signal events and each background events obtained from the tracklets vs. mass template fitting.	105
5.4	Constant coefficients of template functions determined from likeli- hood fitting for north arm (for tracklets vs. pT case).	114

5.5	Constant coefficients of template functions determined from likelihood fitting for south arm (for tracklets vs. pT case)	114
5.6	Number of signal events and each background events obtained from the tracklets vs. pT fitting	117
5.7	Summary of the number of events for signal and backgrounds. . .	119
6.1	Inclusive asymmetries for north arm for tracklets vs. mass case. .	126
6.2	Inclusive asymmetries for south arm for tracklets vs. mass case. .	126
6.3	Inclusive asymmetries for north arm for tracklets vs. pT case. .	127
6.4	Inclusive asymmetries for south arm for tracklets vs. pT case. .	127
6.5	Fitting results for asymmetry measurements for each process for each mass bin and each arm.	129
6.6	Fitting results for asymmetry measurements for each process for each pT bin and each arm.	130

LIST OF FIGURES

1.1	The basic building blocks of visible matter in the universe [3] [4]. . .	3
1.2	Deep inelastic scattering in electron-proton scattering.	7
1.3	Q^2 dependence of $F_2(x, Q^2)$	13
1.4	CT10NNLO parton distribution functions as a function of x for a fixed value of Q [16].	14
1.5	Results of the 1988 EMC experiment [12].	17
1.6	The quark polarizations measured as a function of x from the HERMES inclusive and semi-inclusive asymmetries. Error bars are the statistical uncertainties. The band represents the total systematic uncertainty, where the light gray area is the systematic error due to the uncertainties in the fragmentation model, and the dark gray area is from the contribution of the Born asymmetries [49].	22
1.7	DSSV polarized PDFs of the proton at $Q^2 = 10 \text{ GeV}^2$ [17]. . . .	23
1.8	(a) Drell-Yan Process with quark-antiquark annihilation; (b) DIS Process	25
1.9	Drell-Yan Process in polarized proton-proton collisions.	27
2.1	RHIC for the polarized proton collisions.	30

2.2	The interaction regions and the location of the Siberian Snakes and the spin rotators placed around the collider experiments STAR and PHENIX [33]	35
2.3	(a) p-C polarimeters at RHIC 12clock interaction point, (b) Various asymmetries from different combination of detectors [34].	36
2.4	Schematic representation of the hydrogen jet polarimeter [39].	38
2.5	PHENIX local polarimeter measurement. The raw asymmetry in neutron production divided by the degree of beam polarization is shown vs. azimuthal angle. The solid points are with the spin rotators off (vertical polarization); the open points are with the spin rotators on (longitudinal polarization) [40].	40
2.6	The PHENIX coordinate system.	41
2.7	The PHENIX detector. The upper panel shows a beam view of the PHENIX central arm detectors. The lower panel shows a side view of the PHENIX global and muon arm detectors.	42
2.8	Pseudorapidity(η) and azimuthal angle (ϕ) coverage for the PHENIX detector subsystems.	43
2.9	The PHENIX Central Arm and Muon Arm magnets.	44

2.10 (a) Single Photo Multiplier Tube (PMT) mounted on a 3 cm quartz radiator and (b) An arm of BBC comprising of 64 units (c) The BBC detector as installed in the PHENIX detector behind the central magnet.	46
2.11 (a) Top view of the ZDC location (b) Beam view of the ZDC location.	47
2.12 Mechanical design of a single layer of the ZDC.	49
2.13 Muon Arms, tracking stations within each arm and CSC planes within each tracking station [41].	52
2.14 South MuID [42].	54
2.15 Iarocci streamer tubes in the MuID [42].	55
2.16 Positions of the planned RPC stations, RPC1(a,b), RPC2, and RPC3 [46].	56
2.17 PHENIX DAQ system [47].	57
3.1 Half-detector, with the VTX barrels in the center, and the two FVTX endcaps on either end.	61
3.2 Wedge and schematic diagram of its structure.	63
3.3 Schematic of the HDI stack-up [51].	64
3.4 (a) Exploded view of a disk. (b) A cage with all four disks installed. No wedges have been placed on the disks	66

3.5 (a) Wedges assembled on to a disk (b) Completed North West section of the detector	66
3.6 Read-out electronics block diagram [51].	68
3.7 Block diagram of the ROC board [51].	69
3.8 Block diagram of a FEM board [51].	71
3.9 (a) The cluster size for a distribution of particles thrown over the FVTX acceptance. (b) The resolution of the found cluster centroids for 3 wide clusters (approximately $10 \mu m$).	72
3.10 FVTX + VTX event display for a p+p collision.	73
3.11 (a) FVTX coverage for North Arm. (b) Coverage after combining FVTX and VTX.	74
3.12 Activity around the muon track from jet like event and Drell-Yan event.	75
3.13 The y_0 vs. x_0 graph (a) before and (b) after the $R < 2$ cut.	76
3.14 Tracklet rapidity vs track rapidity graph (a) before and (b) after removing the tracks from tracklets. Green box corresponds to same arm taklets as the tracks while yellow box shows the opposite arm tracklets as the tracks.	77
3.15 Tracklet distribution for J/ψ simulations and J/ψ data.	77
4.1 Fill-by-fill beam polarizations in year 2013 runs for the Blue beam and Yellow beam [54].	79

4.2	(a) Integrated luminosity vs. day for the Run 2013 at PHENIX. (b) Integrated figure of merit metric vs. day for the Run 2013 running period at RHIC.	81
4.3	Dimuon spectrum for PHENIX Run 13.	82
4.4	MUID 2D trigger efficiency for North and South arm separately. .	83
4.5	Stack plot of unlike-sign dimuon invariant mass distributions scaled to a luminosity of 200 pb^{-1} for South arm.	86
5.1	Distance of closest approach (DCA) and its projection to the trans- verse momentum plane (DCAr).	90
5.2	Simulated DCAr distributions for Drell-Yan, $b\bar{b}$ and $c\bar{c}$ with vertex determination from VTX detector.	91
5.3	Simulated DCAr distributions for Drell-Yan, $b\bar{b}$ and $c\bar{c}$ without ver- tex information from VTX detector.	91
5.4	Simulated tracklet distributions for Drell-Yan, $b\bar{b}$ and $c\bar{c}$	93
5.5	Tracklets Vs. Mass, 2-D distributions with fitted template func- tions for Drell-Yan, $b\bar{b}$, $c\bar{c}$ and ψ' simulations for north arm. . . .	96
5.6	Tracklets Vs. Mass, 2-D distributions with fitted template func- tions for Drell-Yan, $b\bar{b}$, $c\bar{c}$ and ψ' simulations for south arm. . . .	96
5.7	2-D histogram projections to mass axis for north arm simulations (for tracklets vs. mass case).	97

5.8	2-D histogram projections to mass axis for south arm simulations (for tracklets vs. mass case)	97
5.9	2-D histogram projections to tracklet axis for north arm simulations (for tracklets vs. mass case)	98
5.10	2-D histogram projections to tracklet axis for south arm simulations (for tracklets vs. mass case)	98
5.11	North arm template fitting (for tracklets vs. mass case)	103
5.12	South arm template fitting (for tracklets vs. mass case)	103
5.13	Template fitted final histogram projections to mass axis and track- lets axis for north arm.	104
5.14	Template fitted final histogram projections to mass axis and track- lets axis for south arm.	104
5.15	The number of events for each process determined from Monte Carlo test for north arm.	107
5.16	The number of events for each process determined from Monte Carlo test for south arm.	107
5.17	2-D distributions of coefficient of Drell-Yan vs. coefficient of $b\bar{b}$ and coefficient of $c\bar{c}$ vs. coefficient of $b\bar{b}$ obtained from Monte Carlo test fittings.	108
5.18	Tracklets Vs. pT, 2-D distributions with fitted template functions for Drell-Yan, $b\bar{b}$, $c\bar{c}$ and ψ' simulations for north arm.	111

5.19 Tracklets Vs. pT, 2-D distributions with fitted template functions for Drell-Yan, $b\bar{b}$, $c\bar{c}$ and ψ' simulations for south arm.	111
5.20 2-D histogram projections to pT axis for north arm simulations (for tracklet vs. pT case).	112
5.21 2-D histogram projections to pT axis for south arm simulations (for tracklet vs. pT case).	112
5.22 2-D histogram projections to tracklets axis for north arm simula- tions (for tracklet vs. pT case).	113
5.23 2-D histogram projections to tracklets axis for south arm simula- tions (for tracklet vs. pT case).	113
5.24 North arm template fit using tracklets vs. pT distributions.	116
5.25 South arm template fit using tracklets vs. pT distribution.	116
5.26 Template fitted final histogram projections to to pT axis and track- lets axis for north arm.	118
5.27 Template fitted final histogram projections to pT axis and tracklets axis for south arm.	118
6.1 North arm signal and background fractions for four tracklet regions (0–5, 5–10, 10–15 and 15–50) for tracklets vs. mass case.	122
6.2 South arm signal and background fractions for four tracklet regions (0–5, 5–10, 10–15 and 15–50) for tracklets vs. mass case.	122

6.3	North arm signal and background fractions for four tracklet regions (0–5, 5–10, 10–15 and 15–50) for tracklets vs. pT case.	123
6.4	South arm signal and background fractions for four tracklet regions (0–5, 5–10, 10–15 and 15–50) for tracklets vs. pT case.	123
6.5	PHENIX Measurement of the $J/\psi A_{LL}$ from Run 13 Data [60] . .	125
6.6	Asymmetry values plotted in to a graph where x axis is heavy flavor fraction and y axis is combinatorial fraction for south arm (mass 4.5 - 5 GeV).	129
6.7	Drell-Yan A_{LL} in two mass bins	130
6.8	Drell-Yan A_{LL} in two pT bins	131
6.9	Drell-Yan A_{LL} after combining two bins for both methods	131
6.10	Heavy flavor background A_{LL} from two methods	132
6.11	Combinatorial background A_{LL} from two methods	132

1 INTRODUCTION

The development of the Standard Model [1] of elementary particle physics has been driven by the curiosity of understanding the structure of matter and the fundamental laws that control the physical universe. Complex and powerful machinery and tools have been built in order to test the Standard Model predictions and develop the theory. Relativistic heavy Ion Collider (RHIC), a proton-proton and heavy ion collider-accelerator at Brookhaven National Laboratory in USA, is one of such powerful machines.

The proton is one of the most studied particle at different scales with a wide variety of probes and experimental techniques. However some of the fundamental properties of the proton such as the intrinsic angular momentum which is also called the “spin” of the proton is not sufficiently explained by any theoretical model. One of the main concerns of this thesis is to address the so called “Spin Puzzle” which is discussed in section 1.3.1.

In this Chapter, an overview of the Standard Model, proton spin structure and the theoretical foundations and predictions needed for the Drell-Yan measurements are discussed. Chapter two describes the experimental setup at PHENIX experiment while chapter three describes the Forward vertex Detector which is the main detector used for this analysis. Data and simulations used for this analysis are described in the chapter four and the analysis procedure is described in

detail in chapter five and chapter six. Final chapter, the chapter seven gives the discussion and conclusions of this study.

1.1 The Standard Model

The Standard Model, a theoretical framework which was developed during the second half of the 20th century describing the structure of matter and the strong, weak and electromagnetic interactions among fundamental particles [2]. Gravity is not considered here since there is no enough theoretical description and experimental clues of the boson called as Graviton, which mediates the gravitational interaction. Standard Model has successfully explained most of the experimental results and precisely predicted a wide variety of phenomena.

According to Standard Model, any natural matter is made up of twelve basic building blocks called fundamental particles which can be categorized in three generations of quarks and three generations of leptons which interacts via four fundamental forces. The force carrier particles are called the fundamental bosons which can be categorized as gauge bosons and the Higgs boson. Figure 1.1 shows the basic building blocks of matter with their properties.

All the elementary matter particles are fermions (spin 1/2) and for each of them there is a corresponding antifermion with same mass, spin and opposite charge. Bound states of quarks are called hadrons and they have integer electric charge. Hadrons are further classified into three categories called baryons, antibaryons and

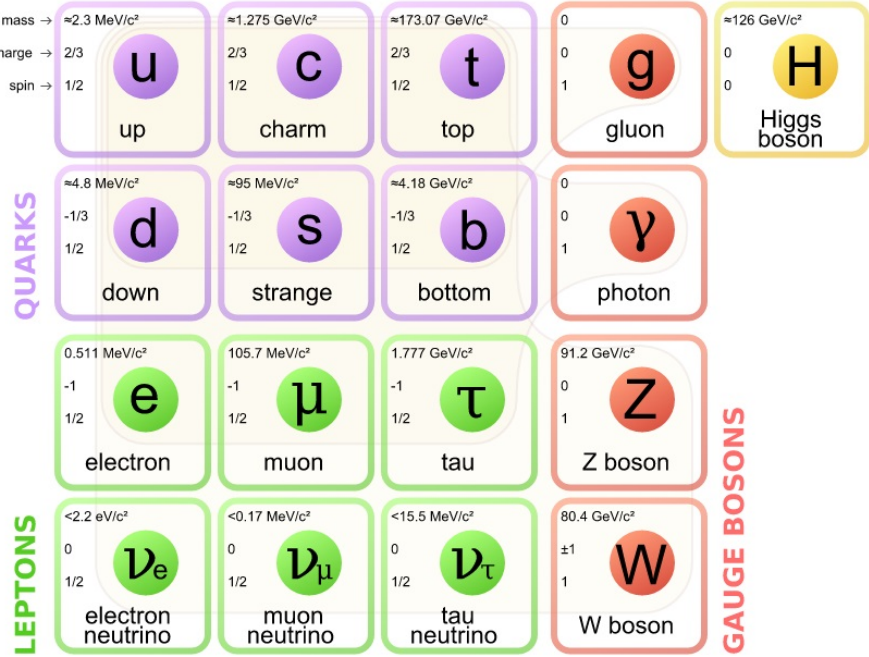


Figure 1.1: The basic building blocks of visible matter in the universe [3] [4].

mesons. The baryons (antibaryons) are bound states of three quarks (antiquarks) and mesons are bound states of a quark and an antiquark.

Mathematically the Standard Model is a quantum field theory which is invariant under local transformations of the gauge symmetry group $SU(3)_C \otimes SU(2)_L \otimes U(1)_Y$. C, L and Y stands for color, weak isospin and hypercharge in order. $SU(3)$ describes the gauge group of the theory of strong interaction mediated by eight gluons known as “Quantum ChromoDynamics” (QCD). $SU(2)_L \otimes U(1)_Y$ is the symmetry group of electromagnetic interaction (EM) mediated by photons and electroweak interaction (EW) mediated by the neutral Z and charged W bosons. This theory is called “Quantum ElectroDynamics” (QED).

QCD is very important in hadron collisions since it describes the strong interaction among the quarks and gluons, the constituents of protons. A quark can carry one of three possible color charges (red, green, or blue) and its antiquark carries the corresponding anticolor. The term color is simply a name to a quantum number which introduces a new internal degrees of freedom to the quarks [5]. All naturally occurring particles are colorless (white color). Therefore the possible colorless combinations are mesons consisting of q (color) \bar{q} (anticolor), and baryons consisting of q (red) q (blue) q (green). A gluon carries one unit of color and one unit of anticolor.

Color-charged particles (quarks and gluons) cannot be found individually and they are grouped with other quarks. This phenomena is called the confinement. The color force strengthens with distance and is responsible for the confinement of quarks. A quark-antiquark pair is produced by the color-force field before quarks can be separated. The energy in this process is conserved because the energy of the color-force field is converted into the mass of the new quarks.

Another property of the color force is that it appears to exert little force at short distances or at high energy or momentum transfers. Therefore the quarks behave like free particles within the confining boundary of the color force. They experience the strong confining force when they begin to get too far apart. This phenomena is called the asymptotic freedom.

It was observed in high energy scattering processes between leptons with pro-

tons that, the virtual photon starts resolving gluons and quark-antiquark fluctuations as the proton is hit harder and harder. That implies, with sufficiently high momentum transfers, quarks behave like free or weakly bound particles. Accordingly asymptotic freedom and confinement are specific features that determines the behavior of quarks and gluons in particle reactions at different energy scales.

The strength of the strong force is given by the strong coupling constant(α_S) [6].

$$\alpha_S(Q^2) = \frac{12\pi}{(33 - 2n_f)\ln\frac{Q^2}{\Lambda_{QCD}^2}} \quad (1.1)$$

The quantity n_f is the number of quark flavors effectively contributing to interaction loops. The fundamental Λ_{QCD} parameter, called ‘Lambda-QCD’ is obtained from experimentally measured dependence of α_S on $|Q^2|$. Its values for three and four excited quarks are

$$\Lambda_{QCD}(3) \approx 400 \text{ MeV}, \Lambda_{QCD}(4) \approx 200 \text{ MeV}$$

Lambda-QCD is important as it separates two energy regimes. For energies less than Λ_{QCD} the coupling constant is large. Therefore a perturbative development of the physical quantities is impossible. When the quarks are very close, where the momentum transfer is large, their interaction is feeble (asymptotic freedom).

All the particles in the Standard Model have already been observed and the latest observation is the Higgs boson. Even though the standard model explains most of the particle physics phenomena, there are few shortcomings of this model.

One of them is that it does not account for the gravitational force. And also it does not explain the existence of dark matter and dark energy. It also fails to explain the asymmetry between the matter and antimatter.

1.2 Historical overview of the nucleon structure

Initially at the beginning of the 20th century, protons and neutrons were considered as point-like particles with spin 1/2 described by the Dirac equation. At that time low energy particle beams with few MeV were used in particle physics experiments which were insufficient to resolve the nucleons. In late 1930s, the magnetic moment of the proton and the neutron were independently measured showing the existence of the anomalous magnetic moment of the nucleons [13]. Since the electric charge of the neutron is zero, the existence of the magnetic moment implied the substructural “electric current” inside the nucleons.

In 1964, M. Gell-Mann and K. Nishijima proposed a model to describe nucleons with constituent spin 1/2 Dirac particles (“quarks”) which have fractional number of electric charges as well as the degree of freedom of color charges [14, 15]. The Nobel Prize for Physics in 1969 was awarded to M. Gell-Mann “for his contributions and discoveries concerning the classification of elementary particles and their interactions” [8].

The first experimental evidence for the nucleons having a structure came from the Deep Inelastic Scattering (DIS) experiment done in Stanford Linear Acceler-

ator Center (SLAC) at the end of the 1960s and the beginning of the 1970s. The Nobel Price for Physics in 1990 was awarded to Jerome I. Friedman, Henry W. Kendall and Richard E. Taylor for their experiment which led to the development of the quark model in particle physics [9].

In DIS process, a quark in the proton gets knocked out by the virtual photon from the interacting electron and the proton gets disintegrated into fragments as can be seen in Figure 1.2. The common variables used in DIS experiments are given in Table 1.1.

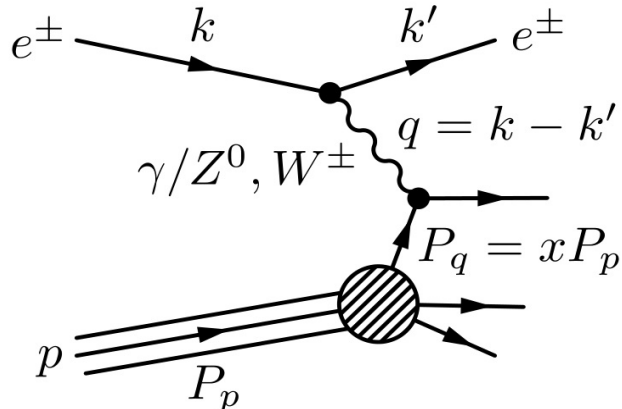


Figure 1.2: Deep inelastic scattering in electron-proton scattering.

Deep inelastic regime is defined as scattering with a Q^2 larger than roughly 1 GeV and W^2 , the mass of the final state of nucleon greater than 4 GeV 2 where the perturbative QCD (pQCD) provides reliable calculations [10]. Each constituent of a proton carries a momentum fraction x of the the proton. The possible values of the momentum fraction of a constituent can be between 0 and 1 during every

Table 1.1: Variables used in DIS

Variable Name	Invariant Form	Lab Frame	Description
E		E	Lab Frame initial electron energy
M		M	Rest mass of target nucleon
k^μ		$(E, 0, 0, \vec{k})$	Initial 4 momentum of electron
s^μ		$1/m(k, 0, \vec{0}, E)$	Initial spin vector of electron
E'		E'	Lab frame final electron energy
k'^μ		(E', \vec{k}')	Final 4-momentum of electron
θ		θ	Lab frame electron scattering angle
p^μ		$(M, 0, 0, 0)$	Initial 4 momentum of nucleon
S^μ			Initial spin vector of nucleon
q^μ		$k - k'$	4 momentum of virtual photon
ν	$p \cdot q/M$	$E - E'$	Lab frame energy of virtual photon
Q^2	$(k - \vec{k})^2$	$4EE' \sin^2(\theta/2)$	Virtual photon four momentum squared
x	$Q^2/2p \cdot q$	$Q^2/2M \cdot \nu$ or $2EMxy$	Fraction of nucleon momentum carried by the struck quark
y	$(p \cdot q)/(p \cdot k)$	ν/E	Fraction of energy lost by electron
W^2	$(p + q)^2$	$M^2 + Q^2(\frac{1-x}{x})$	Invariant mass squared of hadronic final state

scattering process. We can denote the probability to find the constituent f with momentum fraction between x and dx as $\phi_f(x, Q^2)dx$. The probability functions $\phi_f(x, Q^2)$ are called parton distribution functions (PDFs). PDFs should be determined by experiments since they are not calculated with the pQCD. However it should be able to get the total momentum p of the proton by adding all of the momentum fractions carried by partons. Therefore PDFs satisfy the condition

$$\sum_f \int_0^1 x\phi_f(x, Q^2)dx = 1 \quad (1.2)$$

The **cross section** (σ) which quantify the production rates of a given particle in a scattering experiment is one of the quantities used to compare the theory and experiments. Cross section is measured by counting the number of produced particles using their observed properties such as mass, momentum and charge. The differential cross section ($d\sigma/d\Omega$) quantifies the particle production rates in a manner that is independent of the experimental apparatus. Ω is the solid angle.

The electron-proton DIS cross section to leading order in α_s (the strong coupling constant) is given as

$$\begin{aligned} \sigma(e(k) + p(P) \rightarrow e(k') + X) = \\ \int_0^1 dx \sum_f \phi_f(x, Q^2) \cdot \sigma(e(k) + f(xP) \rightarrow e(k') + f(p')) . \end{aligned} \quad (1.3)$$

The equation 1.3 separates the cross section to contributions from soft partonic structure which should be determined from experiments and contributions from

hard elastic process of $e + f \rightarrow e + f$ which should be determined from pQCD theory.

The differential cross for the DIS interaction depicted in Figure 1.2 can be written as

$$\frac{d\sigma}{d\Omega dE'} = \frac{\alpha^2}{2Mq^4} \frac{E'}{E} L_{\mu\nu} W^{\mu\nu} \quad (1.4)$$

where $L_{\mu\nu}$ is the lepton tensor which describes the electron - photon vertex and $W^{\mu\nu}$ is the hadronic tensor which represents the virtual photon - nucleon interaction. α is the electromagnetic coupling constant, and $q^2 \equiv (k - k')^2$ is the momentum transfer.

Since the electron is a fundamental Dirac particle, the lepton tensor can be written using spinors (u) and gamma (γ) matrices as

$$L_{\mu\nu} = [\bar{u}(k', s') \gamma_\mu u(k, s)]^* [\bar{u}(k', s') \gamma_\nu u(k, s)] \quad (1.5)$$

After taking the sum over all possible spin states s' of the final state lepton (ignoring the spin of final state electrons), the leptonic tensor can be split into a symmetric (S) and an antisymmetric (A) part (by interchanging the Lorentz indices μ and ν) as

$$L_{\mu\nu}(k, s; k') = 2 [L_{\mu\nu}^S(k; k') + iL_{\mu\nu}^A(k, s; k')] \quad (1.6)$$

Where, spin-independent symmetric term $L_{\mu\nu}^S$ can be given as

$$L_{\mu\nu}^S = k_\mu k'_\nu + k'_\mu k_\nu - g_{\mu\nu}(k \cdot k' - m^2) \quad (1.7)$$

and the asymmetric spin dependent term $L_{\mu\nu}^A$ as

$$L_{\mu\nu}^A = m\epsilon_{\mu\nu\rho\sigma}s^\rho(k - k')^\sigma. \quad (1.8)$$

Here $\epsilon_{\mu\nu\rho\sigma}$ is the totally-antisymmetric Levi-Civita tensor (with $\epsilon_{0123} = +1$) and m is the lepton mass. An expression for the hadronic tensor can not be directly written since the nucleon is not a fundamental particle. However it must be Lorentz invariant transforming as a rank 2 tensor and it must be invariant under parity and time reversal. Further it should conserve the hadronic electromagnetic current. Therefore $W^{\mu\nu}$ can be written by summing over all final hadronic states and spins as

$$\begin{aligned} W^{\mu\nu} = & F_1(x, Q^2)(-g^{\mu\nu} + \frac{q^\mu q^\nu}{q^2}) \\ & + \frac{F_2(x, Q^2)}{p \cdot q}(p^\mu - \frac{p \cdot q}{q^2}q^\mu)(p^\nu - \frac{p \cdot q}{q^2}q^\nu) \\ & + i \frac{g_1(x, Q^2)}{p \cdot q}\epsilon^{\mu\nu\sigma\rho}S_\sigma q_\rho \\ & + i \frac{g_2(x, Q^2)}{(p \cdot q)^2}\epsilon^{\mu\nu\sigma\rho}[(p \cdot q)S_\sigma - (S \cdot q)p_\sigma]q_p \end{aligned} \quad (1.9)$$

F_1, F_2, g_1, g_2 , are known as structure functions of the nucleon. F_1 and F_2 are the unpolarized structure functions and contribute to all scattering cross sections. g_1, g_2 are polarized structure functions and contribute only for cross-sections with polarized electron and polarized struck nucleon. Structure functions also can be described as functions of x_B and Q^2 . x_B is called Bjorken- x , and this is identical to the momentum fraction of the parton (x).

$$x_B \equiv -\frac{q^2}{2P \cdot q} = -\frac{q^2}{2M\nu}, \quad Q^2 \equiv -q^2 \quad (1.10)$$

F_1 and F_2 are measured independently in experiments which verified the parton model [7]. F_1 and F_2 are approximately independent of Q^2 at $x \simeq 0.25$ which is called Bjorken scaling. It means the structure of the parton which interacts with the scattering electron does not change no matter how strong the force used.

In order to relate the structure functions to the quark content (PDFs) in the nucleon, the Quark Parton Model (QPM) must be considered. QPM was developed by Bjorken and Feynman in the late 1960's, which provided an intuitive explanation for the observed Bjorken scaling [22, 23, 24, 25]. In the QPM, the basic assumption is that at large Q^2 and ν , the photon interacts incoherently with the free spin 1/2 point constituents inside the nucleon. These constituents, called "partons", were later recognized to be the quarks, whose existence had been proposed a few years earlier by Gell-Mann and Zweig using the symmetry properties of the mesons and baryons multiplets. The basic assumption is valid at high energies at a reference frame where the nucleon is moving with infinite momentum in z direction. In such a frame the transverse momentum components and the rest mass of the partons and the nucleon can be neglected.

In parton model, one can express the unpolarized structure functions as

$$F_1(x, Q^2) = \frac{1}{2x} \sum_f \phi_f(x, Q^2) e_f^2 \quad (1.11)$$

$$F_2(x, Q^2) = \sum_f \phi_f(x, Q^2) e_f^2 \quad (1.12)$$

Therefore unpolarized PDFs can be determined from the unpolarized structure

functions. The structure function F_2 has been measured extensively at HERA (H1 and ZEUS), SLAC, CERN, and BCDMS as shown in the Figure 1.3. However the Q^2 dependence of the F_2 structure function at fixed x_B violates the Bjorken scaling, implying the existence of the gluons. The PDFs determined in the CT10 analysis are shown in Figure 1.4 and described in detail in reference [11].

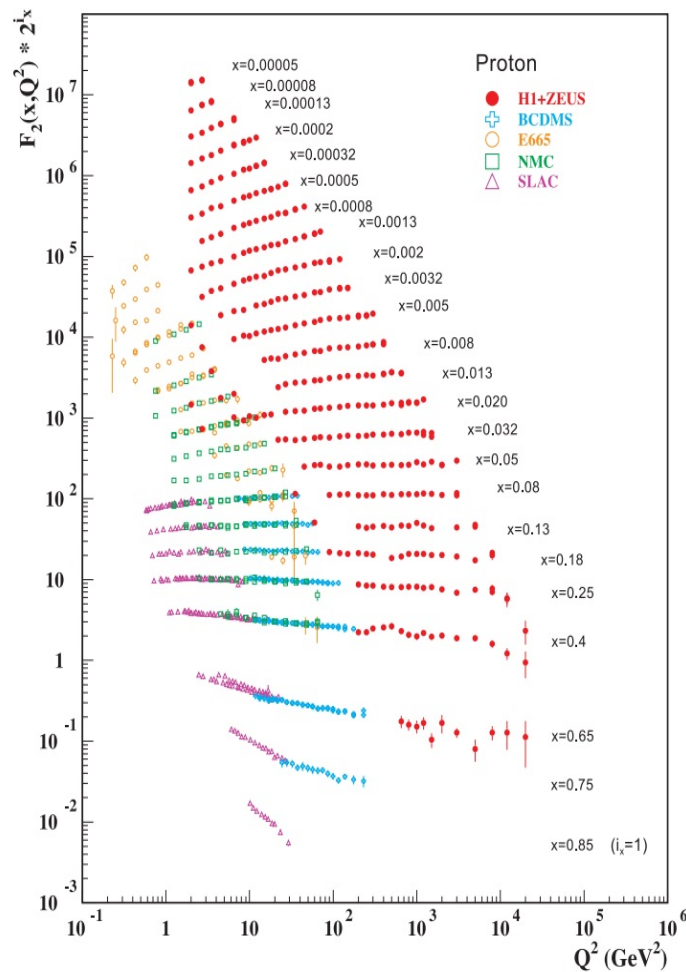


Figure 1.3: Q^2 dependence of $F_2(x, Q^2)$ at various x obtained by many experiments [16].

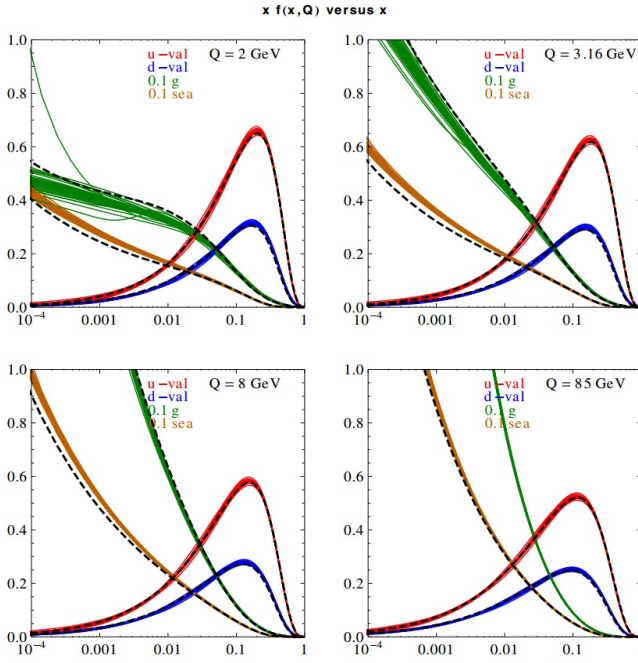


Figure 1.4: CT10NNLO parton distribution functions as a function of x for a fixed value of Q [16].

1.3 Spin structure of the nucleon

In order to probe the Nucleon spin structure using the DIS experiments, the beam and the target protons should be polarized (polarized DIS). For the longitudinally polarized electron-proton collisions we can write the difference of the cross section by either flipping the electron polarization or flipping the proton polarization as

$$\begin{aligned} \frac{d\Delta\sigma}{d\Omega dE'} &\equiv \frac{d\sigma^{(\rightarrow\Rightarrow)}}{d\Omega dE'} - \frac{d\sigma^{(\rightarrow\Leftarrow)}}{d\Omega dE'} \\ &= -\frac{4\alpha^2}{Q^2 M \nu} \frac{E'}{E} [(E + E' \cos\theta) g_1(x, Q^2) - 2x g_2(x, Q^2)] \quad (1.13) \end{aligned}$$

The single arrow (\rightarrow) denotes the direction of electron polarization and the double arrow (\Rightarrow) denotes the direction of proton polarization. Right arrows denote pos-

itive helicities and left arrows denote negative helicities. $d\sigma^{(\rightarrow\Rightarrow)} = d\sigma^{(\leftarrow\leftarrow)}$ and $d\sigma^{(\rightarrow\leftarrow)} = d\sigma^{(\leftarrow\rightarrow)}$ stands due to the parity conservation in electromagnetic interactions. Thus it is possible to measure the two spin dependent hadron structure functions, $g_1(x, Q^2)$ and $g_2(x, Q^2)$ using the longitudinally polarized DIS measurements.

For a given quark in a proton, it can be considered two possible helicity components. One component is helicity-positive component (“+”) and the other component is helicity-negative component (“-”). For example,

$$q_+^\Rightarrow(x, Q^2) \quad (1.14)$$

is the helicity-positive (“+”) component of PDF when the proton’s helicity (\Rightarrow) is positive.

The unpolarized PDFs are given by summing up the quarks helicity-positive and negative components (those corresponding to the proton’s positive helicity \Rightarrow).

$$q_+^\Rightarrow(x, Q^2) + q_-^\Rightarrow(x, Q^2) = q^\Rightarrow(x, Q^2) = q(x, Q^2) \quad (1.15)$$

$$q_-^\Leftarrow(x, Q^2) = q_+^\Rightarrow(x, Q^2), \quad q_+^\Leftarrow(x, Q^2) = q_-^\Rightarrow(x, Q^2) \quad (1.16)$$

The polarized PDFs are defined as

$$\begin{aligned} \Delta q(x, Q^2) &\equiv q_+^\Rightarrow(x, Q^2) - q_+^\Leftarrow(x, Q^2) \\ &= q_+^\Rightarrow(x, Q^2) - q_-^\Rightarrow(x, Q^2). \end{aligned} \quad (1.17)$$

The antiquark polarized PDFs, $\Delta\bar{q}(x, Q^2)$, can also be defined in a similar way.

In parton model, one can express the spin dependent hadron structure functions as

$$g_1(x, Q^2) = \frac{1}{2} \sum_f e_f^2 (\Delta q_f(x, Q^2) + \Delta\bar{q}_f(x, Q^2)) \quad (1.18)$$

$$g_2(x, Q^2) = 0 . \quad (1.19)$$

$g_2(x, Q^2)$ is zero, since it is related to the transverse degrees of freedom of the quarks within the nucleon. In QPM all the partons are assumed to move collinearly to the nucleon.

1.3.1 Spin Puzzle

In 1988 the European Muon Collaboration (EMC) conducted a polarized DIS experiment with a beam of muons scattered off of a proton target. Prior to this experiment, it was believed that the spin composition of the three valence quarks within the nucleon account for the whole of the spin polarization of the proton. But the results of the EMC experiment found that the $g_1(x)$ structure function of the proton is much smaller than necessary for the valence quark spin to account for the proton spin. The sum of the quark and antiquark polarized PDFs $\frac{1}{2}\Delta\Sigma$ contribute only about 20 to 35 % of the total proton spin S_p . This surprising and puzzling result was termed the “proton spin puzzle”. The $g_1(x)$ distribution plot from the EMC experiment is shown in Figure 1.5. Therefore, the remaining spin

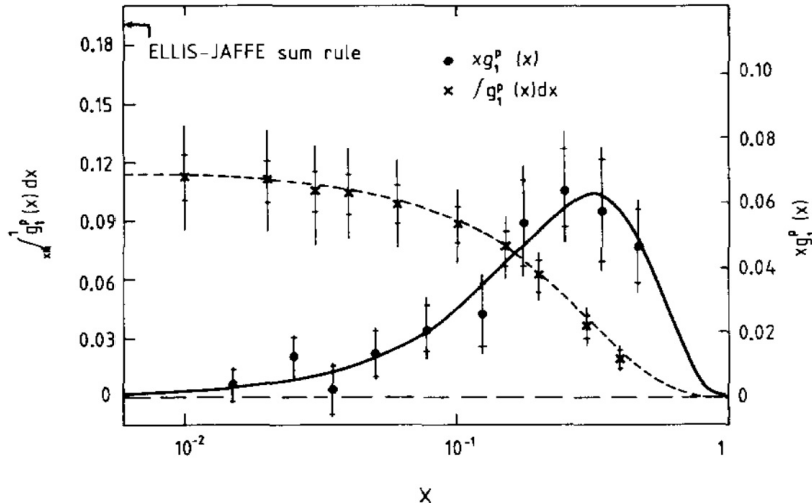


Figure 1.5: Results of the 1988 EMC experiment [12].

polarization must derive from one of the other possible sources within the nucleon as described by

$$S_p = \frac{1}{2} = \frac{1}{2} \Delta \Sigma + \Delta G + L_q + L_g \quad (1.20)$$

where ΔG is gluon polarization, L_q is orbital angular momenta of quarks and L_g is orbital angular momenta of gluons.

Generally, polarized DIS experiments have determined the polarization of quark + antiquark distributions with fairly small uncertainties. However, inclusive DIS measurements are incapable of flavor decomposition (identify quark form anti-quark) since it does not have the information about the parent quark except the charge. Therefore semi inclusive deep inelastic scattering (SIDIS) was introduced in order to access the quark flavors separately.

1.3.2 Semi Inclusive Deep Inelastic Scattering (SIDIS)

In semi-inclusive DIS (SIDIS), scattered lepton as well as the leading hadron are detected simultaneously. Although the fundamental scattering process of the SIDIS is the same as that of the DIS, the detection of the leading hadron (the hadron with highest momentum which is believed to contain the struck quark) offers additional insights into the nucleon structure. In the simple quark-parton model, the cross section of the SIDIS process can be expressed as:

$$\sigma^h \propto \sum_f e_f^2 q_f(x) \cdot D_{qf}^h(z) \quad (1.21)$$

The function $D_{qf}^h(z)$ is called the fragmentation function, which represents the probability of a quark flavor f fragmenting into a hadron h with the partons momentum fraction $z = E_h/\nu$. Similarly to the PDFs, $D_{qf}^h(z)$ also should be measured in experiments since they cannot be treated using perturbative QCD since the strong coupling constant α_s becomes too large at low energy, which is exactly where fragmentation occurs.

$D_{qf}^h(z)$ offers additional information about the struck quark such as differentiate the quark flavor (eg. u quark and the \bar{u} quark) which the DIS is incapable of. Similar to the PDFs, fragmentation function $D_{qf}^h(z)$ also depends on the scale Q^2 and satisfy the following momentum sum rule:

$$\sum_h \int_0^1 z D_{qf}^h(z) dz = 1 \quad (1.22)$$

The semi-inclusive structure functions can be defined as

$$g_1^h(x, z) = \frac{1}{2} \sum_f e_f^2 \delta q_f(x) \cdot D_{qf}^h(z) \quad (1.23)$$

$$F_1^h(x, z) = \frac{1}{2} \sum_f e_f^2 q_f(x) \cdot D_{qf}^h(z) \quad (1.24)$$

1.3.3 Hadron collider experiments

In hadron collider experiments, two opposite high energy beams of hadrons are collided. Most of the collisions involve only soft interactions of the constituent quarks and gluons which cannot be treated using perturbative QCD, because α_s is large when the momentum transfer is small. However in some collisions two quarks or gluons will exchange a large momentum where the elementary interaction takes place very rapidly compared to the internal time scale of the hadron wave functions. These collisions can be identified as hard collisions.

Polarized proton-proton collisions provide an alternative way of measuring polarized PDFs without requiring the knowledge of fragmentation functions through the W , Z/γ^* productions for which the final states are only leptons. Therefore the relatively large uncertainties of the antiquark polarized PDFs due to the limited knowledge of fragmentation functions of hadrons in SIDIS experiments can be reduced. The cross section and the spin asymmetry for Drell-Yan process in a collider experiment are described in Section 1.4.

1.3.4 Spin asymmetry

When expressing the difference of two small cross sections as in equation 1.13, the relative errors can be quite large. Therefore asymmetry of the cross section is often discussed. It is defined as the difference of the cross section divided by their sum which cancel the common factors along with their associated uncertainties. For a longitudinally polarized beam and target, the parallel asymmetry can be defined as

$$A_{||}(x, Q^2) = \frac{\frac{d\sigma^{(\rightarrow\rightarrow)}}{d\Omega dE'} - \frac{d\sigma^{(\rightarrow\leftarrow)}}{d\Omega dE'}}{\frac{d\sigma^{(\rightarrow\rightarrow)}}{d\Omega dE'} + \frac{d\sigma^{(\rightarrow\leftarrow)}}{d\Omega dE'}} \quad (1.25)$$

At the vertex where nucleon is longitudinally polarized and the virtual photon is circularly polarized, the difference between parallel and antiparallel cross sections of the interaction can be measured as a parallel asymmetry which is denoted as A_1 . Hence for inclusive DIS, longitudinal asymmetry can be derived in the quark parton model as

$$A_1(x) = \frac{g_1(x)}{F_1(x)} = \frac{\sum_f e_f^2 \delta q_f(x)}{\sum_f e_f^2 q_f(x)} \quad (1.26)$$

In analogy to the inclusive one, the semi-inclusive asymmetries can be expressed in the quark parton model as

$$A_1^h(x)|_z = \frac{\int_Z dz g_1^h(x, z)}{\int_Z dz F_1^h(x, z)} = \frac{\int_Z dz \frac{1}{2} \sum_f e_f^2 \delta q_f(x) \cdot D_{qf}^h(z)}{\int_Z dz \frac{1}{2} \sum_f e_f^2 q_f(x) \cdot D_{qf}^h(z)} \quad (1.27)$$

Similarly for longitudinally polarized hadron-hadron collisions, it can be defined the longitudinal double spin asymmetry A_{LL} as

$$A_{LL} = \frac{\sigma_{++} + \sigma_{--} - \sigma_{+-} - \sigma_{-+}}{\sigma_{++} + \sigma_{--} + \sigma_{+-} + \sigma_{-+}} \quad (1.28)$$

where + and - denotes the helicity crossings.

Further A_{LL} in terms of the spin dependent yields (N_{ij}) can be defined as

$$A_{LL} = \frac{1}{P_B P_Y} \frac{N_{++} - RN_{+-}}{N_{++} + RN_{+-}} \quad (1.29)$$

where P_B and P_Y are the polarization of the two beams and R is the relative luminosity between like (++) and unlike (+-) helicity crossings ($R = L_{++}/L_{+-}$). Experimentally the spin asymmetries are measured in order to obtain the PDFs through the global fits.

1.3.5 Current sea quark polarization measurements

Dedicated measurements of the quark and anti-quark polarizations have been made in polarized semi-inclusive DIS experiments by identifying hadrons in the final state. Data have been obtained by the SMC, HERMES, and COMPASS collaborations at scales, Q^2 ranging from 1 to 50 GeV [18]. The quark polarizations measured as a function of x from the HERMES inclusive and semi-inclusive asymmetries are given in Figure 1.6.

DSSV [17] is one of the theoretical groups working on calculating the polarized gluon and antiquark PDFs using the experimental data including the RHIC data.

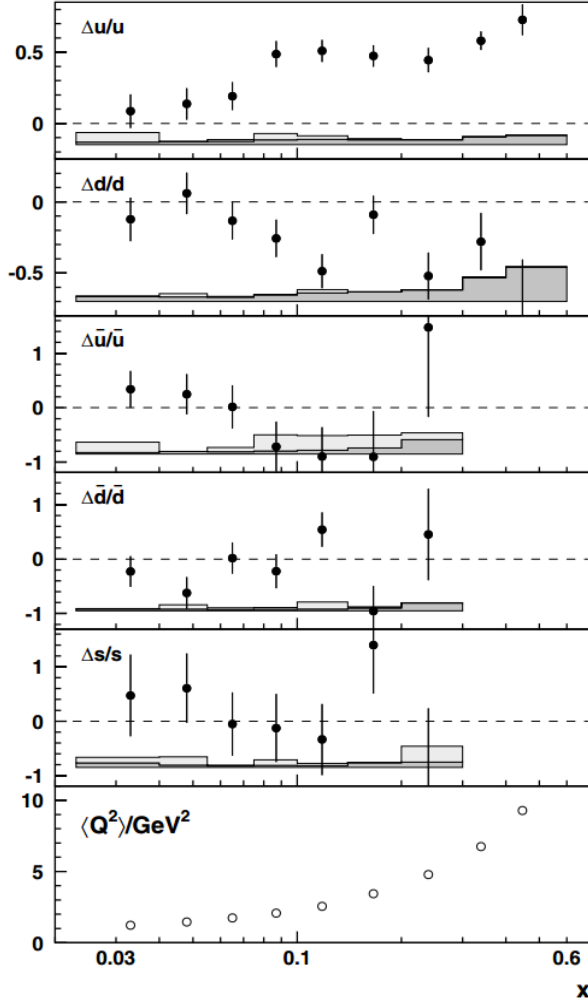


Figure 1.6: The quark polarizations measured as a function of x from the HERMES inclusive and semi-inclusive asymmetries. Error bars are the statistical uncertainties. The band represents the total systematic uncertainty, where the light gray area is the systematic error due to the uncertainties in the fragmentation model, and the dark gray area is from the contribution of the Born asymmetries [49].

A complete summary of all of the polarized PDFs as determined in the latest global analysis by DSSV group are shown in Figure 1.7.

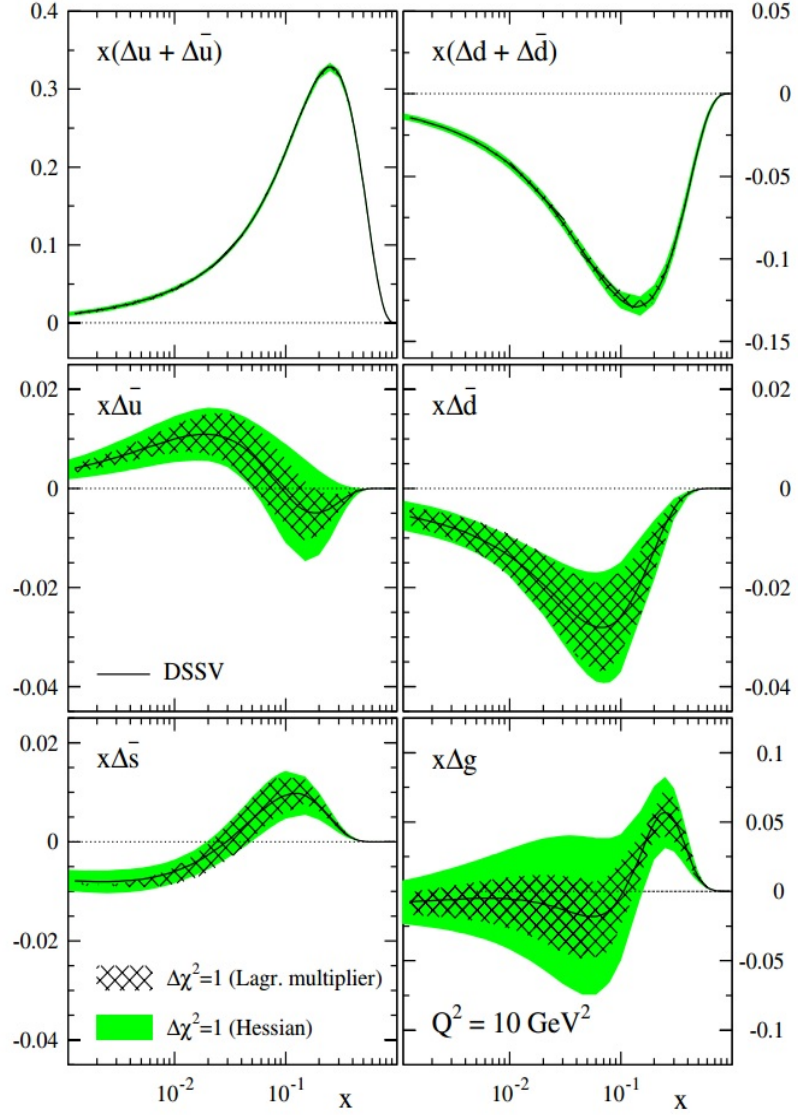


Figure 1.7: DSSV polarized PDFs of the proton at $Q^2 = 10 \text{ GeV}^2$ [17].

As can be seen in Figure 1.7, total quark densities are well constrained. But the anti-quark and gluon distributions are measured with relatively large uncer-

tainties. In RHIC, attempts are being made to improve the understanding of the light sea quark polarizations in the nucleon with W and Drell-Yan asymmetry measurements. Further to constrain the $\Delta g(x)$ and its integral, π^0 and Jet asymmetries are measured.

1.4 The Drell-Yan process in proton-proton collisions

The Drell-Yan process (DY) is the virtual photon production due to the quark-antiquark annihilation ($q\bar{q} \rightarrow \gamma^* \rightarrow l^+l^-$) as illustrated in Figure 1.8(a). The decay product of the photon which is a lepton pair (l^+l^-) is observed in the experiment. This process was first discussed by Sidney Drell and Tung-Mow Yan in 1970 [19] in order to describe the production of lepton - antilepton pairs in high-energy hadron collisions. Today the Drell-Yan process which provides valuable information about the parton distribution functions (PDFs) is studied in both fixed-target and collider experiments. This process was first observed in proton - uranium collisions at the Alternating Gradient Synchrotron at Brookhaven National Laboratory.

In addition to the DIS experiments, the Drell-Yan process is also a very powerful tool that utilizes the Electromagnetic probe to study the nucleon structure. Figure 1.8 shows that both DIS and Drell-Yan are similar processes. Drell-Yan process is considered as a clean probe to access quark and antiquark information inside the nucleon and the Drell-Yan production in proton-proton collisions at

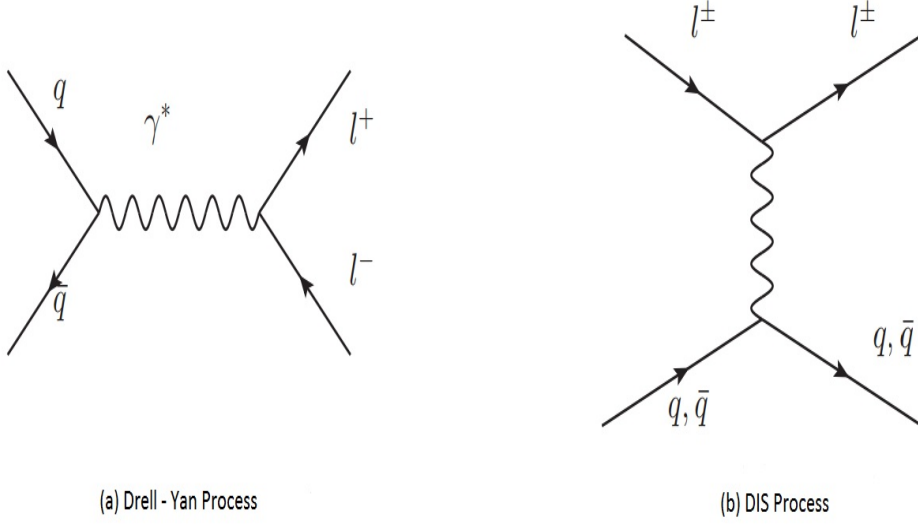


Figure 1.8: (a) Drell-Yan Process with quark-antiquark annihilation; (b) DIS Process

collider experiments are robust in theoretical understanding.

In this thesis, production of muon pair ($\mu^+ \mu^-$) through a virtual photon from annihilation of a quark from one proton and an antiquark from another proton in high energy collisions is studied.

At the leading order, the differential cross section of the Drell-Yan process can be expressed as:

$$\frac{d\sigma^2}{dx_1 dx_2} = \frac{4\pi\alpha^2}{9sx_1 x_2} \sum_i e_i^2 [q_i(x_1)\bar{q}_i(x_2) + \bar{q}_i(x_1)q_i(x_2)] \quad (1.30)$$

where x_1 and x_2 are the fraction of nucleon momentum carried by each of the colliding quark and antiquark, respectively and $q_i(x)$ is the corresponding quark probability density distribution. s is the square of the center of mass energy of two

colliding hadrons and e_i is the charge of quark flavor i . The Feynman variable(x_F) can be defined as $x_F = x_1 - x_2$, which is a scaled variable that describes hadron production in $p + p$ collisions. x_1 and x_2 can be calculated for a given collider experiment by using the following relationships.

$$\tau = x_1 \cdot x_2 = \frac{M^2}{s} \quad (1.31)$$

$$y = \frac{1}{2} \ln \frac{E + p_{||}}{E - p_{||}} \quad (1.32)$$

$$\eta = -\ln[\tan \frac{\theta}{2}] = \frac{1}{2} \ln \frac{|P| + p_{||}}{|P| - p_{||}} \quad (1.33)$$

M is the invariant mass of the lepton pairs and y is the rapidity, defined as a function of the energy of the particle (E) and the projection of the momentum parallel to the beam axis ($p_{||}$). η is the pseudorapidity describing the angle (θ) between particle three-momentum and the positive direction of the beam axis. For relativistic particles with $P \gg m$, pseudorapidity becomes equal to (true) rapidity.

Then the x_1 and x_2 can be calculated as

$$x_{1,2} = \sqrt{\tau} e^{\pm y} \quad (1.34)$$

As we discussed section 1.3.5, the spin structure of the nucleon has been extensively investigated by polarized (SI)DIS experiments. Since the finding that quarks contribute a surprisingly small fraction to the nucleons total helicity, physicists had a considerable interest centered on QCD processes in hadronic collisions,

where polarized gluon and antiquark effects are directly manifested. The Drell-Yan process at leading order in polarized proton proton collisions is given in Figure 1.9

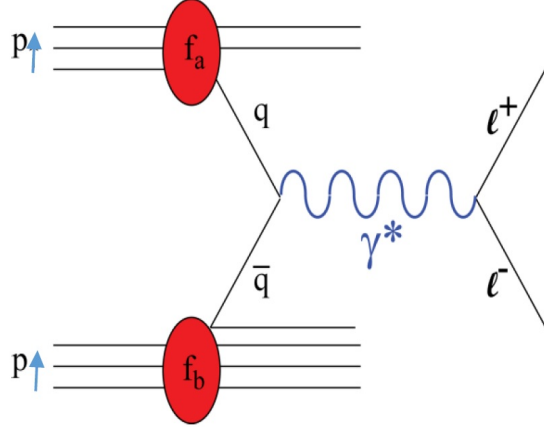


Figure 1.9: Drell-Yan Process in polarized proton-proton collisions.

At the leading order, the longitudinal double spin asymmetry (requiring polarization of both protons) in the DY process is, given by [20],

$$A_{LL}^{DY}(x_1, x_2) = \frac{\sum_i e_i^2 [\Delta q_i(x_1) \Delta \bar{q}_i(x_2) + \Delta \bar{q}_i(x_1) \Delta q_i(x_2)]}{\sum_i e_i^2 [q_i(x_1) \bar{q}_i(x_2) + \bar{q}_i(x_1) q_i(x_2)]} \quad (1.35)$$

where Δq_i and $\Delta \bar{q}_i$ are the polarized PDFs whereas q_i and \bar{q}_i are the unpolarized PDFs. This equation can be simplified by choosing the kinematic region, where a the term, $u(x_1)\bar{u}(x_2)$, dominates the denominator of Equation 1.35. Then the equation becomes [21],

$$A_{LL}^{DY}(x_1, x_2) = \frac{\Delta u(x_1)}{u(x_1)} \frac{\Delta \bar{u}(x_2)}{\bar{u}(x_2)} \quad (1.36)$$

As stated earlier in this section, by using Equations 1.31, 1.32, 1.33 and 1.34, x_1

and x_2 can be calculated for Drell-Yan experiment at a given beam energy, rapidity and invariant mass of a lepton pair. In this study x_1 is calculated approximately as 5×10^{-2} and x_2 as 2×10^{-3} . Consequently, the Drell-Yan analysis at RHIC, provides the opportunity to study anti quark helicity distributions at very low x where no other experiment has ever accessed.

1.5 Overview of the analysis

In this thesis, a measurement of Drell-Yan fraction and longitudinal double spin asymmetry (A_{LL}) at forward rapidity ($\eta = 1.2$ to $\eta = 2.4$) in $p + p$ collisions at $\sqrt{s} = 510$ GeV is considered. The total integrated luminosity $\sim 50 \text{ pb}^{-1}$ of data collected by the PHENIX detector is used for this analysis. The invariant mass range of the muon pair used in this study is $4.5 < M < 8$ GeV where other known physics processes have minimal contributions.

2 EXPERIMENT SETUP AT PHENIX

In order to analyze particles which are produced in high energy scattering events, major accelerator facilities with sophisticated and massive arrays of detectors are needed. This analysis is based on the data taken at the Relativistic Heavy Ion Collider (RHIC) with the PHENIX detector during the year 2013 (Run 13). In the first section of this chapter, RHIC is briefly described with respect to polarized proton collisions and in the the second section, the PHENIX detector system is described. The third section describes the triggering and the data acquisition (DAQ).

2.1 RHIC

RHIC is an accelerator facility at Brookhaven National Laboratory (BNL) in Long Island, New York, USA. It is capable of creating symmetric and asymmetric collisions with heavy ions such as gold, deuteron, copper and lead. Quark-gluon plasma (QGP), a new state of matter at very high temperature is studied through heavy ion collisions. Although its called as Heavy Ion Collider, it is the world's first, and the only collider capable of providing polarized proton-proton collisions which provides a unique opportunity to study the spin property of proton through strong and weak interactions. For the heavy ion collisions the center of mass energy of a nucleon-nucleon collision pair (taking one nucleon from one nucleus

and one nucleon from the other nucleus) ranges from 7.7 to 200 GeV. For proton-proton collisions the center of mass energy ranges from 62.4 to 510 GeV. The schematic diagram of RHIC with the essential components required to produce polarized proton collisions is drawn in Figure 2.1.

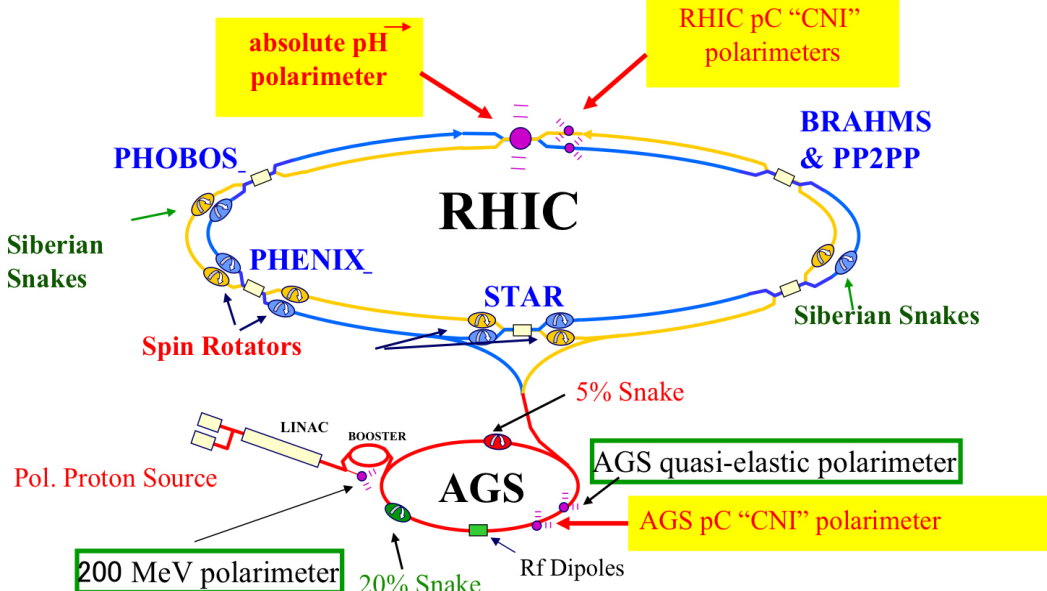


Figure 2.1: RHIC for the polarized proton collisions.

2.1.1 Polarized Ion Source and Accelerator Complex

Optically-Pumped Polarized Ion Source (OPPIS) [26] generates the polarized proton beam with $\sim 10^{12}$ nuclearly polarized H^- ion bunches in $400 \mu s$ long pulses. The polarization of H^- ion bunches is about 80% and the kinetic energy is 35 keV. These ions are extracted and accelerated to 750 keV by RFQ and transferred to the 200 MHz Linear Accelerator (LINAC) where they are accelerated to 200 MeV.

The electrons are also striped off from the ion beam at the end of LINAC and a pulse of protons are captured into a single bunch in the BOOSTER which is a fast cycling synchrotron. At the BOOSTER, the proton beam is brought up to the injection energy of 2.35 GeV for the Alternating Gradient Synchrotron (AGS). AGS accelerates polarized protons to 24.3 GeV and delivers them to the RHIC for further acceleration.

Relativistic Heavy Ion Collider (RHIC) is a double-ring superconducting collider which accelerates proton beams up to 255 GeV in order to achieve a center of mass energy (\sqrt{s}) ranging from 62.4 GeV to 510 GeV. It is 2.4 miles in circumference and the world's highest energy accelerator for studying spin-polarized proton structure.

The clockwise beam is called as “Blue beam” and the counterclockwise beam is called as “Yellow beam”. Each of them can fill up to 120 proton bunches with a bunch crossing time period of 106 ns. Some of the RHIC machine parameters achieved in Run 13 are given in Table 2.1

Accelerated protons from the AGS are sent through the AGS-to-RHIC transfer line which makes vertical and horizontal shifts to reach the RHIC plane. The beams collide at four different collision points around the ring after they are accelerated to the desired energy. The DX dipole magnets are used to merge the two beams in order to have head-on collisions at the interaction points.

Table 2.1: Some RHIC machine parameters for Run 13

Parameters	Value
Type of collision	proton-proton
Energy of the beam	255 GeV
Ions per bunch	165×10^9
Peak luminosity	$1.45 \times 10^{32} \text{ cm}^{-2}\text{s}^{-1}$
Average luminosity	$0.90 \times 10^{32} \text{ cm}^{-2}\text{s}^{-1}$
Typical lifetime of a fill	8 hours

Currently PHENIX [27] and STAR [28] are the only experiments actively taking data. The smaller experiments PHOBOS [29] and BRAHMS [30] were decommissioned in 2005 after achieving their goals.

2.1.2 Siberian Snakes and Spin Rotators

In order to achieve high energy polarized proton beams, an greater understanding of the evolution of spin during acceleration and the tools to control it is required. The evolution of the spin direction of a beam of polarized protons in external magnetic fields in a circular accelerator is governed by the Thomas-BMT equation given as,

$$\frac{d\vec{P}}{dt} = -\left(\frac{e}{\gamma m}\right)[G_\gamma \vec{B}_\perp + (1+G)\vec{B}_\parallel] \times \vec{P} \quad (2.1)$$

where $\gamma = E/m$ is the Lorentz factor of the accelerated particle, G is the anomalous magnetic moment and \vec{P} is the polarization vector expressed in the frame that moves with the particle. This precession equation is very similar to the Lorentz force equation for the orbital motion in an external magnetic field which is given as,

$$\frac{d\vec{v}}{dt} = -\left(\frac{e}{\gamma m}\right)[\vec{B}_\perp] \times \vec{v} \quad (2.2)$$

Therefore it can be seen that, in a pure vertical field, the spin rotates G_γ times faster than the orbital motion by comparing these two equations. G_γ then gives the number of full spin precessions for every full revolution. For an ideal planar accelerator G_γ is called the spin tune ν_{sp} . For a proton with energy of 250 GeV, G_γ is approximately 478 [33].

Due to the intrinsic spin resonance from spin precession around the radial field components in the focusing magnets and the imperfection of dipole and quadrupole magnetic field from mis-alignment, maintaining beam polarization could be a difficult task during acceleration. The stable spin direction close to a resonance is perturbed away from the vertical direction by the resonance driving fields.

Siberian Snakes [31, 32] which can rotate the polarization direction of the proton beam were introduced to RHIC in order to overcome these depolarization resonances. The stable spin direction is unperturbed as long as the spin rotation

from the Siberian Snake is much larger than the spin rotation due to resonance fields. Two full Snakes which rotates the polarization of the proton by 180° are installed in RHIC and partial Snake that rotates the polarization of the proton by 9° is installed in AGS. Further each STAR and PHENIX uses two upstream and two downstream spin rotating magnets which are called "spin rotators" that bring stable transversely polarized protons into longitudinal collisions and then to rotate the remaining protons in the bunch back into transverse polarization. Schematic diagram of the configuration of the Siberian Snakes and rotators is shown in Figure 2.2.

2.1.3 Polarimetry

Polarimeters are one of the most crucial instrumentation in RHIC for polarized proton collisions which ensures the maximization of the number of ions in the bunches polarized in the needed direction. In RHIC two different polarimeters: Proton-Carbon (p-C) polarimeter and the Hydrogen-Jet (H-Jet) polarimeter are installed for responsive and precise measurements of the polarization. Both types of polarimeters are designed to measure the transverse spin asymmetry A_N and its raw asymmetry ε_N which are defined as follows.

$$\varepsilon_N \equiv PA_N \equiv \frac{N_L - N_R}{N_L + N_R} \quad (2.3)$$

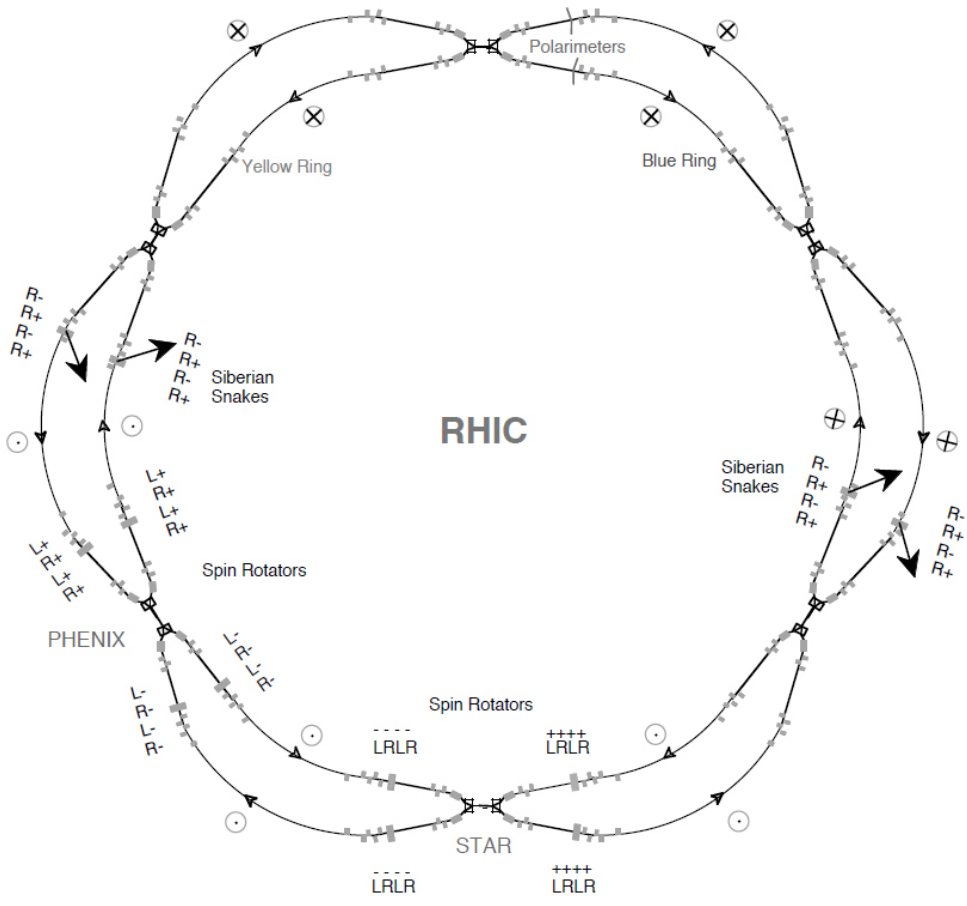


Figure 2.2: The interaction regions and the location of the Siberian Snakes and the spin rotators placed around the collider experiments STAR and PHENIX [33]

where P is the polarization of either the beam or the target, and $N_{L(R)}$ is the number of events detected at the left(right)-side detector with respect to the beam direction. The polarization of the beams in RHIC is determined within a systematic uncertainty $\Delta P/P \approx (\mathcal{O})5\%$.

Proton-Carbon (p-C) polarimeter measures the polarization profile of the beam at RHIC by utilizing elastic proton-Carbon scattering in the Coulomb-Nuclear Interference (CNI) region. Therefore it is known as the CNI polarimeter. In each RHIC ring, as shown in Figure 2.3, a thin($10\ \mu m$) ribbon of Carbon is placed in the path of the beam and the asymmetry of recoiled carbon is measured using six silicon detectors surrounding the beam path [33, 36]. The six detectors

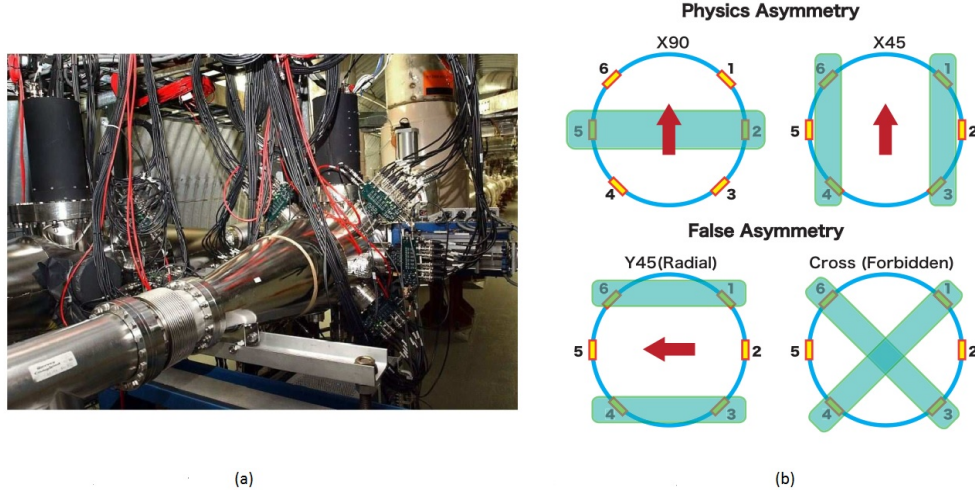


Figure 2.3: (a) p-C polarimeters at RHIC 12clock interaction point, (b) Various asymmetries from different combination of detectors [34].

are placed at 18.5 cm from the carbon ribbon target and aligned 45° , 90° , 135°

azimuthally in both left and right sides with respect to the beam. Figure 2.3 (b) shows that certain combinations of detectors (X90 or X45) provide physics asymmetries coming from vertical spin state protons and other combinations reveal the existence of radial spin direction (Y45) or forbidden asymmetries.

Due to the large cross section of proton-carbon elastic scattering, the CNI polarimeter collects about 4×10^6 recoil carbons per one scanning approximately in one minute. Therefore per fill, two or three times of polarization measurements are possible which monitors the long-term polarization decrease during the fill.

The polarization of the beam can be written as,

$$P_{beam} = -\frac{\varepsilon_N^{pC}}{A_N^{pC}} \quad (2.4)$$

where ε_N^{pC} is the raw asymmetry in the detected recoil carbon nuclei. The CNI polarimeter measures polarization relatively because the true transverse asymmetry A_N for proton-carbon elastic scattering is not known.

Hydrogen jet polarimeter (H-jet polarimeter) provides an independent measurement of the absolute polarization and calibrates the p-C polarimeter [37, 38]. The H-jet polarimeter uses a polarized hydrogen gas jet stream as a target acrosses RHIC in the vertical direction. The polarization of the jet is well known at $P_{Hjet} \sim 97\%$ [38]. The physics measurement at PHENIX and STAR are not affected as the density of the hydrogen gas is not high and the event rate of H-jet polarimetry is about 5 Hz. Thus the H-jet measurement is continuously taking

during the fill since the interaction rate is quite low. Similarly to the p-C polarimeter,

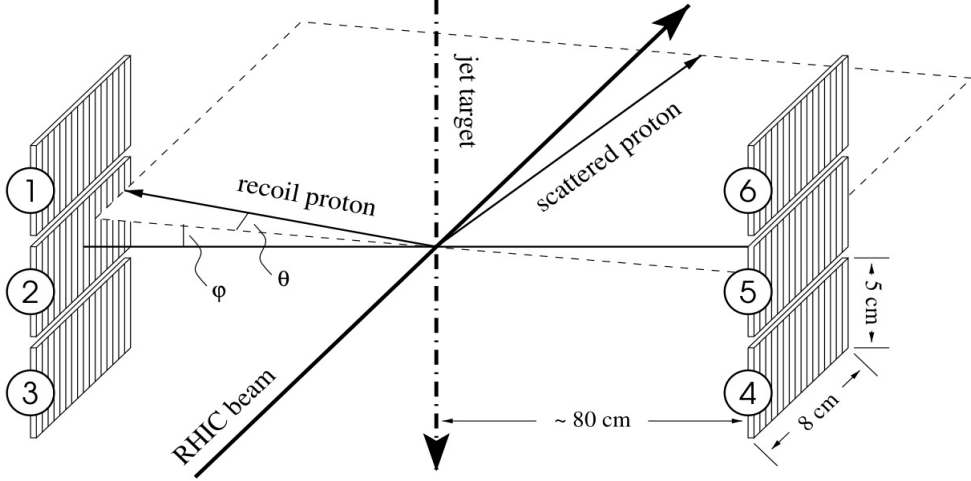


Figure 2.4: Schematic representation of the hydrogen jet polarimeter [39].

ter, the elastic scattering of the proton beam and the proton target is measured with silicon detectors as shown in Figure 2.4. Since both the beam and the target are protons, the physics asymmetry will be the same for both beam and target. As a result it can be measured the raw transverse asymmetry for both the beam and the target as,

$$A_N = \frac{\varepsilon_N^{\text{beam}}}{P_{\text{beam}}} = \frac{\varepsilon_N^{\text{target}}}{P_{\text{target}}} \quad (2.5)$$

Hence it can be obtained the following formula,

$$P_{\text{beam}} = \frac{\varepsilon_N^{\text{beam}}}{\varepsilon_N^{\text{target}}} \cdot P_{\text{target}} \quad (2.6)$$

After determining the beam polarization with the H-jet polarimeter, it is possible to measure the physics asymmetry A_N^{pC} . Therefore p-C polarimeter also can be used to supply an absolute measurement of the polarization.

PHENIX local polarimeter is used to monitor the spin direction of polarized protons at the experiment as a cross check with the other two polarimeters and to validate if the spin direction is appropriately rotated by the spin rotator in the longitudinally polarized collisions. Shower Maximum Detector (SMD) combined with Zero Degree Calorimeter (ZDC) located at very forward region at the PHENIX detectors are used as the PHENIX local polarimeter. More details about ZDC is discussed in Section 2.2.2.

ZDCs mainly detect neutrons produced by collisions. The neutron production in proton-proton collision has a non-zero transverse single spin asymmetry up to $A_N \sim 10\%$. Thus we can measure the residual transverse polarization with ZDCs while taking the data where deviations from pure vertical/radial transverse polarization can be detected (Figure 2.5). For the longitudinally polarized collisions, the local polarimeter is used for measuring the remaining transverse polarization of the beam which could be a source of systematic uncertainties of the spin asymmetry measurement [35].

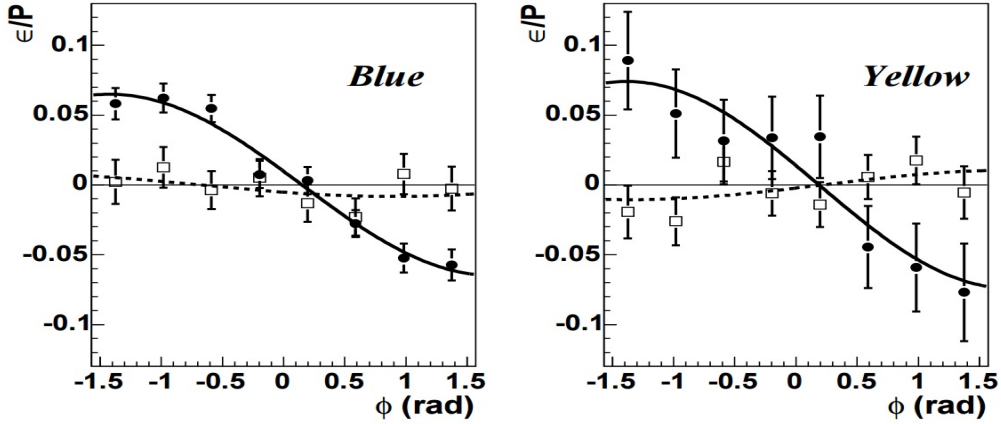


Figure 2.5: PHENIX local polarimeter measurement. The raw asymmetry in neutron production divided by the degree of beam polarization is shown vs. azimuthal angle. The solid points are with the spin rotators off (vertical polarization); the open points are with the spin rotators on (longitudinal polarization) [40].

2.2 PHENIX

The Pioneering High Energy Nuclear Interaction eXperiment (PHENIX) is the largest active experiment at RHIC located at the 8 o'clock intersection point (IP8). It consists of a collection of specialized detector subsystems designed specifically for the efficient detection of photons, leptons, and hadrons with excellent particle identification capability. It also deals with both high-multiplicity heavy-ion collisions and high event-rate pp collisions.

Figure 2.6 shows the definition of global coordinate system used in the PHENIX experiment. The geometrical center of the interaction region is defined as the origin $(0; 0; 0)$ and the beam-line is taken as z-axis (North : positive z direction). The beam pipe which is made of Beryllium has the dimensions of 20 mm in radius

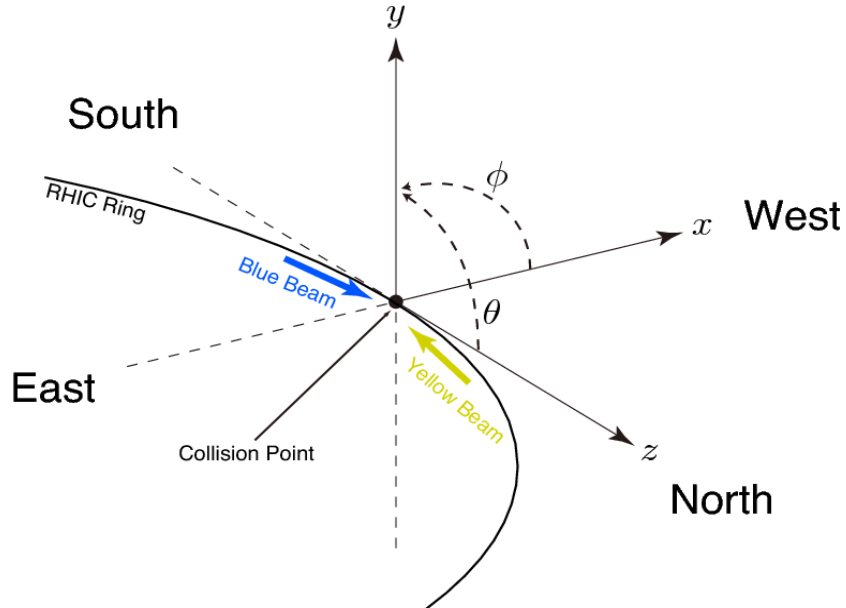


Figure 2.6: The PHENIX coordinate system.

and $500\ \mu\text{m}$ in thickness. x-axis is defined in the direction of West arm whereas y-axis is defined in upward. Thus the resulting coordinate system is right-handed. The azimuthal angle ϕ is measured counter-clockwise relative to the positive x direction and the polar angle θ is defined as the angle relative to z-axis. Using the polar angle, the pseudo-rapidity variable can be expressed as:

$$\eta = -\ln[\tan(\theta/2)]. \quad (2.7)$$

The PHENIX detector subsystems are categorized into three main groups namely, global detectors, central arm detectors and muon arm detectors. Global detectors are used for event characterization and triggering. Two central arms, East and West arms covering $2 \times (\pi/2)$ in azimuthal angle ϕ in the rapidity region of $|\eta| < 0.35$ are mainly used on the study of photons, electrons and hadrons.

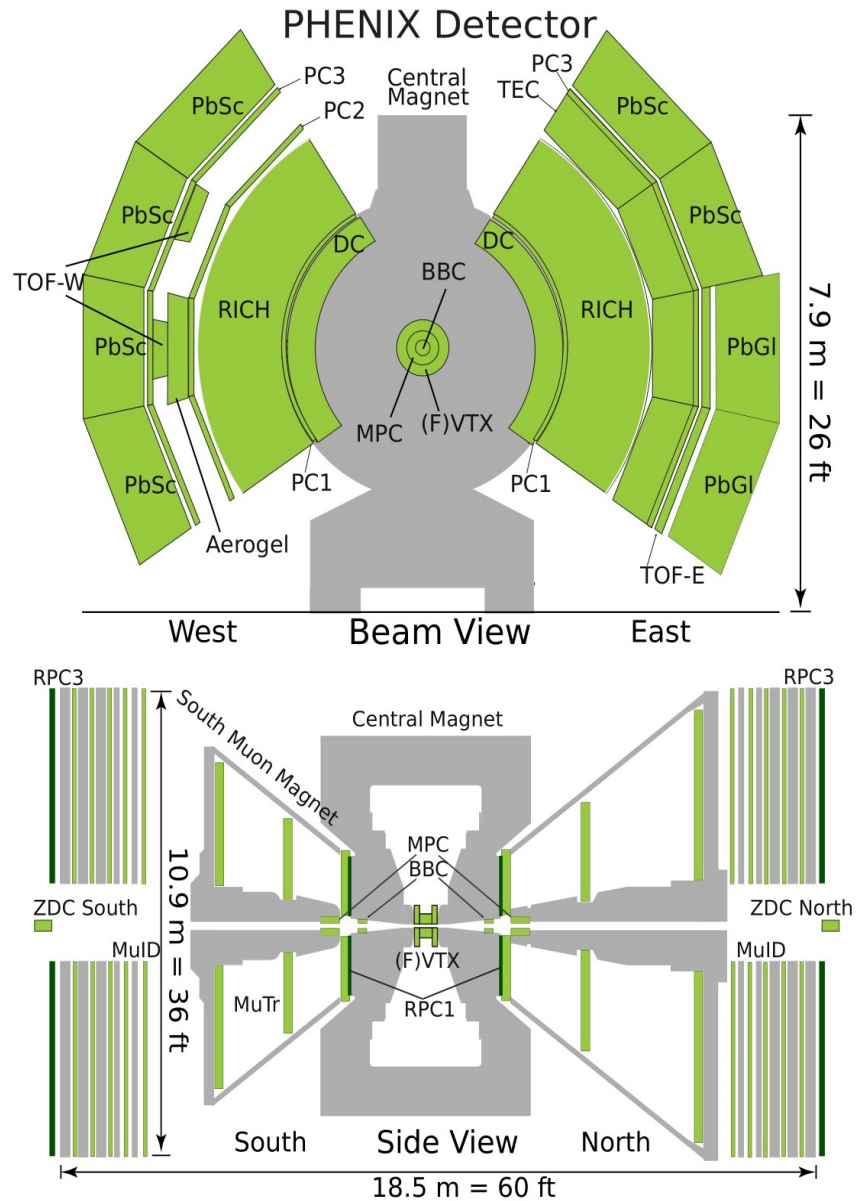


Figure 2.7: The PHENIX detector. The upper panel shows a beam view of the PHENIX central arm detectors. The lower panel shows a side view of the PHENIX global and muon arm detectors.

Two muon arms, north and south arms, covering a full azimuthal coverage and the rapidity region of $1.2 < \eta < 2.4$ and $-2.2 < \eta < -1.2$ are mainly study muons in the forward rapidities. In addition to these large spectrometers, the PHENIX has recently installed the Muon Piston Calorimeters (MPC) which cover forward rapidity region of $3.1 < |\eta| < 3.7$. As it can be seen Figure 2.8 PHENIX experiment sacrifices hermetic 4π coverage in order to achieve greater precision and data acquisition speed in an attempt to study rare processes. Apart from these subsystems PHENIX has three magnets: central magnet and two muon magnets which provide magnetic fields for momentum measurement of charged particles.

Figure 2.7 displays a schematic view of the PHENIX detector setup.

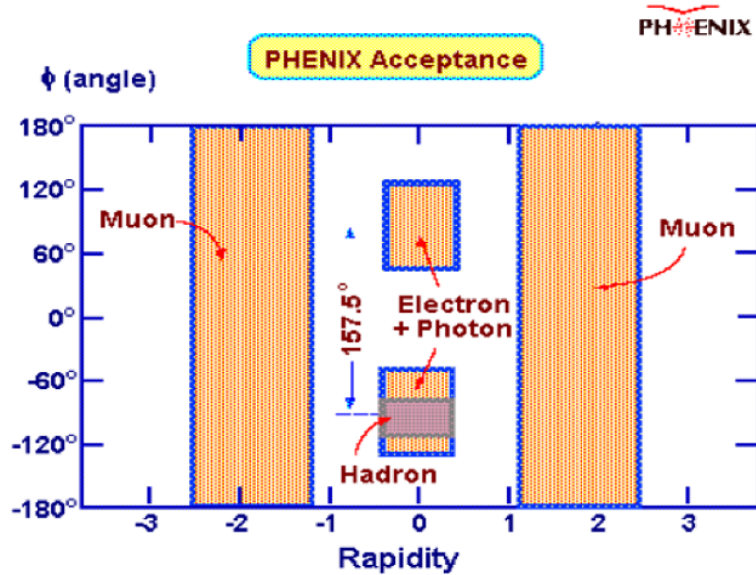


Figure 2.8: Pseudorapidity(η) and azimuthal angle (ϕ) coverage for the PHENIX detector subsystems.

2.2.1 PHENIX magnets

The Central Magnet (CM), North Muon Magnet (MMN) and South Muon Magnet (MMS) of the the PHENIX magnet system are shown in Figure 2.9. The Central Magnet creates the magnetic field parallel to the beam axis (z -direction) by two, inner and outer pairs of concentric coils resulting the charged particles to bend in the azimuthal direction. The coils can be operated separately, with the same polarities or opposite polarities. The integrated axial magnetic field of the Central Magnet is $0.78 \text{ T} \cdot \text{m}$ at $\theta = \pi/2 \text{ rad}$. The Central Magnet also works as a hadron absorbers for forward rapidity. The North and South Muon Magnets produce a

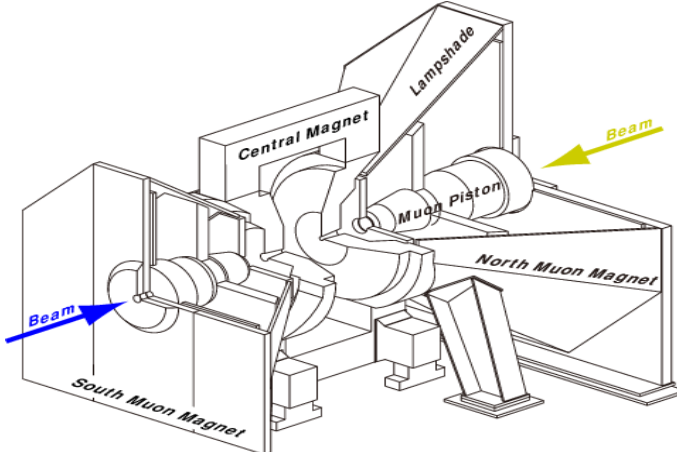


Figure 2.9: The PHENIX Central Arm and Muon Arm magnets.

radial magnetic field. Each magnet consists of two solenoidal coils in the tapered core of the Muon Arm called the Muon Piston in order to produce the radial field. The integrated magnetic field for Muon Magnets at $\theta = 15^\circ$ is $0.72 \text{ T} \cdot \text{m}$.

2.2.2 Global detectors

The Beam Beam Counters (BBC) and the Zero Degree Calorimeters (ZDC) are categorized as the global detectors since they are commonly used by all measurements in PHENIX for event characterization and triggering. Both detectors provide the essential role information for determining whether or not, within a given crossing, a collision has occurred.

Beam Beam Counters (BBC) detector is used for the purposes of triggering, monitoring the luminosity, determining event vertex along beam direction and timing calibrations for time of flight calculations. It is composed of two arms mounted on south and north arms of PHENIX. Both arms locate at 144 cm from the interaction point around the beam axis with the 10 cm of inner diameter and 30 cm of outer diameter. In each arm there are 64 photo multiplier tubes located radially around the beam pipe equipped with 3 cm quartz crystals on the head of PMT as a Cherenkov radiator. They are sensitive to charged particles with $\beta > 0.7$. Figure 2.10 shows a diagram of an arm of BBC, Photo Multiplier Tube and a picture where the BBC is located in the PHENIX detector behind the central magnet. The coverage of the detector is very forward with pseudorapidity of approximately $3.0 < |\eta| < 3.9$ and full azimuthal coverage.

The BBC provides the information of collision point and the time of interaction from time of flight measurement. BBC has an RMS timing resolution of 54 ps.

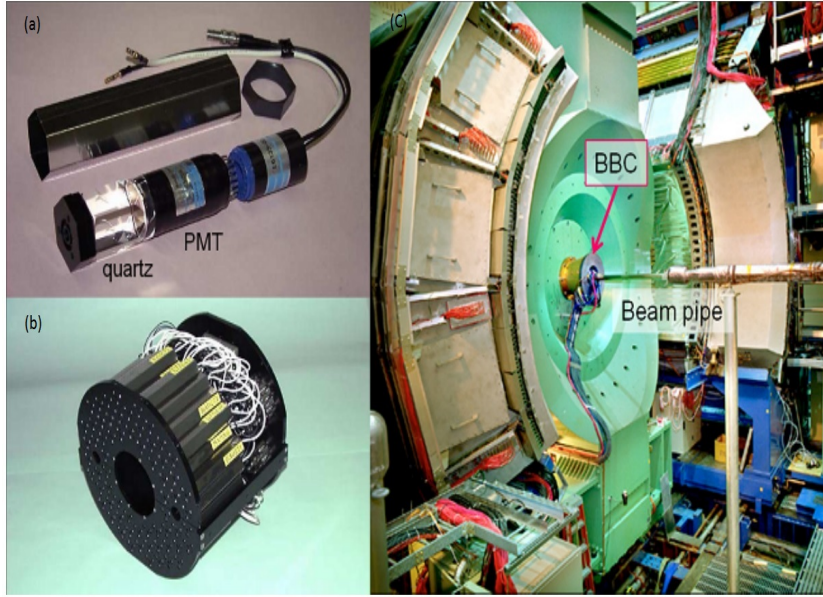


Figure 2.10: (a) Single Photo Multiplier Tube (PMT) mounted on a 3 cm quartz radiator and (b) An arm of BBC comprising of 64 units (c) The BBC detector as installed in the PHENIX detector behind the central magnet.

The time of interaction (t_0) and the beam-beam collision point along beam axis (z vertex) are calculated from the average time of arrival at the north (t_N) and south (t_S) arms and their differences according to the following relation

$$z_{BBC} = c(t_N - t_S)/2 \quad (2.8)$$

$$t_0 = (t_N + t_S)/2 \quad (2.9)$$

The vertex calculation is performed both offline and online where the online vertex calculation is used to issue the minimum bias triggers. For online measurements spatial resolution of BBC z_{vtx} vertex measurement is about 5 cm and for

offline measurements it is about 2 cm.

Zero Degree Calorimeter (ZDC) is a hadronic calorimeter used for neutron tagging at very forward cone angle of less than 2.8 mrad (pseudo-rapidity range $\eta \geq 6$). ZDC also consists of two arms like the BBC. But they are located much farther from the interaction point which is approximately ± 18 m with a horizontal acceptance of ± 5 cm and sit behind the DX dipole magnet as shown in Figure 2.11. The DX magnets sweep away most of the charged particles, and neutral particles with long life, which are mainly neutrons and photons, hit the ZDCs.

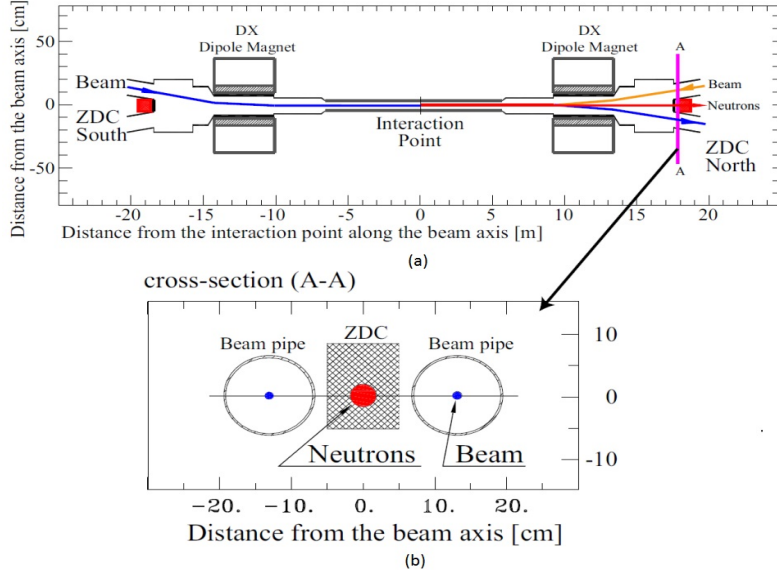


Figure 2.11: (a) Top view of the ZDC location (b) Beam view of the ZDC location.

Each layer of ZDC is consisting of an absorber composed of copper-tungsten

and a PMT which collects light guided along optical fibers that are sandwiched behind the absorber. Since ZDC measures neutrons, it has an additional charged particle identifier and veto in the form of an additional layer of scintillator placed between the front of the ZDC and the interaction point. A secondary detector called Shower Maximum Detector(SMD) is located between the first two layers of the ZDC and is composed of horizontal and vertical scintillator strips of 15 mm or 20 mm widths. To maximize energy resolution, the SMD strips are inclined at 45° . They are capable of providing position resolutions of approximately 1 cm in the transverse plane. The timing resolution of the ZDC detector is approximately 100 ps and provides a second vertex measurement. However the reduced timing resolution and the larger distance from the interaction point causes the ZDC to have a much poorer vertex resolution (10-30 cm). Consequently the ZDC is typically not used for vertex determination purposes. But it still can be used as a local level-1 triggering detector and luminosity monitor. Mechanical design of a single layer of the ZDC is shown in the Figure 2.12.

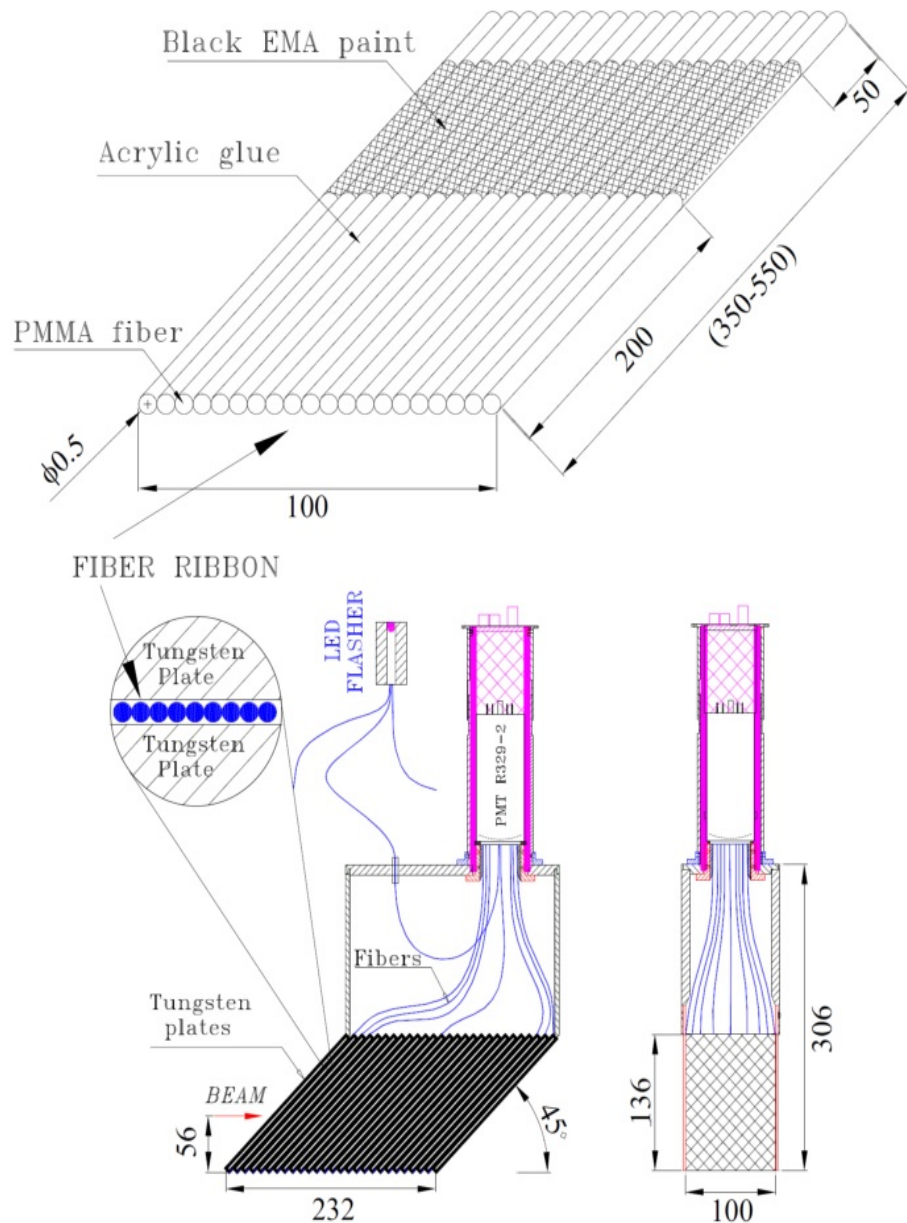


Figure 2.12: Mechanical design of a single layer of the ZDC.

2.2.3 Central arm detectors

The central arm detectors consists of two arms called East Arm and the West Arm. They are located at central rapidity covering $-0.35 < \eta < 0.35$ and the tracking coverage is available from the Drift Chamber and Pad Chamber which covers approximately $\pi/2$ azimuthally in each of the two arms. Particle identification is done using rich imaging Cerenkov detector as well as precision time of flight detectors (ToF) with resolutions of approximately 100 ps. Further two electromagnetic calorimeters consisting of lead glass (PbGl) and lead scintillator(PbSc) technologies provide a better control of systematic uncertainties. The barrel precision silicon pixel vertex tracker (VTX) matches and exceeds the coverage of the original tracking detectors and provides a high resolution primary vertex measurement. It enables the discrimination of prompt or short lived intermediate particles and longer lived intermediates such as B or D mesons.

The main focus of the central arm detectors is to provide high resolution tracking using finely segmented electromagnetic calorimetry which is suitable for the high occupancy found in heavy ion collisions. The typical channels studied by the central arm are two photon decays of π^0 , direct photons and electron pairs from J/ψ decays. The central arm subsystems consists of Silicon Vertex Tracker (VTX), Drift Chambers (DC), Pad Chambers (PC1, 2, and 3), Ring Imaging Cerenkov detectors (RICH), Aerogel Cherenkov detectors, Time Expansion Chamber (TEC)

and Electromagnetic Calorimeters (EMCal) are shown in the upper panel of Figure 2.7.

2.2.4 Forward arm detectors

As can be seen in Figure 2.7 the forward arm detectors are Muon Tracker, Muon ID, RPC and FVTX. In this section details on Muon Tracker, Muon ID and RPC are discussed. FVTX is discussed in the next chapter.

Muon Tracker The Muon Tracker (MuTr) system is a high resolution forward spectrometer located at the forward (North) and backward (South) regions of PHENIX. Each MuTr arm has a full 2π coverage in ϕ . The South MuTr covers a pseudorapidity range of $(-2.2 < \eta < -1.1)$, and the North MuTr covers $(1.1 < \eta < 2.4)$. MuTr operates in a radial magnetic field and function as the main tracking detector of the Muon Arms. Each MuTr arm is composed of three stations called Station - 1, 2, 3 counting from inner to outer. South arm three stations are located 1.80, 3.00, 4.60 m in z-direction from the interaction point whereas the North arm stations are located at 1.80, 3.47, 6.12 m z locations. As can be seen in Figure 2.13, each station consists of eight segments called “octants”. The first two stations are composed of three cathode strip readout tracking chambers (CSC) and two in the final station as shown in Figure 2.13. CSC is also called as gaps and each gap has two cathode planes which are read out. Two cathode

Muon Tracking Nomenclature

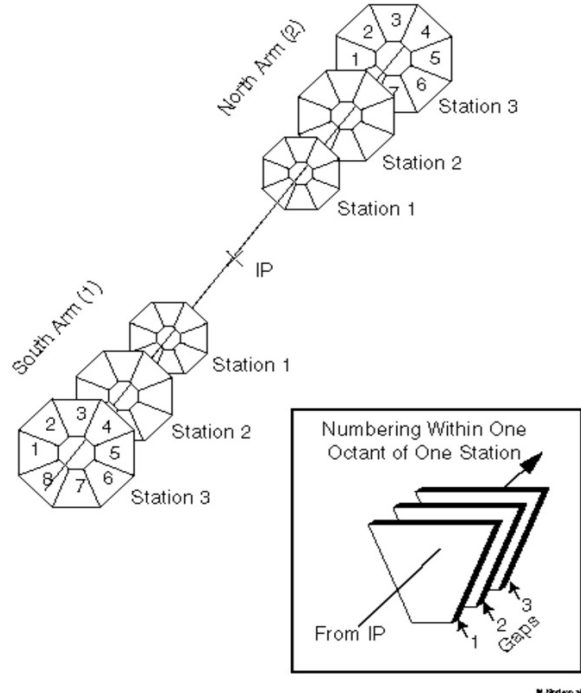


Figure 2.13: Muon Arms, tracking stations within each arm and CSC planes within each tracking station [41].

planes of the gap are placed at a 6.4 mm distance and are held at approximately 1.85 kV below the anode wires. The chambers are filled with a mixture of Ar , CO_2 , and CF_4 gases. Charged particles passing through the gas deposits charge onto the anode wires, creating an image charge on the cathode strips, which is digitized and translated into known positions, or coordinates, within the detector. Pattern recognition algorithm convert these information into tracks. The azimuthal bending of the tracks with knowledge of the magnetic field strength provide momentum information. Series of absorbers in the muon arms reduce the hadronic background and identify muons by their highly penetrating nature.

Muon Identifier (MuID) is a trigger detector of the Muon Arm and located behind the MuTr detector (Figure 2.7). It also provides the seed of the offline tracking. MuID system comprises of steel absorber walls interleaved with five layers of Iarocci tubes (Figure 2.15) which are arrays of nine 9×9 mm wire cells with either 2.5 or 5.6 m length and 8.4 cm width [43]. Iarocci tubes are arranged both horizontally and vertically to provide two dimensional position information. Each cell has an anode wire surrounded by a square cathode and the gas in the cell is the mixture of 92 % CO₂ and 8 % isobutane. In both arms there are 6340 tubes and the applied high voltage is 4300 - 4500 V, which achieves the multiplication of $\sim 2 \times 10^4$.

The detector layer between steel absorbers is also called as “gap”. To reach the final gap of the MuID, a muon must have an energy of at least 2.7 GeV, while the probability for a pion with 4 GeV to reach the same depth is 3% or less [44]. Therefore it greatly increase the purity of muons within the sample of all tracks in the MuTr.

Resistive Plate Chambers(RPC) provides a dedicated trigger for W measurement by providing excellent timing resolution with fast time response and high efficiency. First the RPC3 was installed right behind MuID in 2009 and RPC1 was installed right before MuTr Station 1 in 2011 as shown in Figure 2.16. However the construction of the RPC2 was not approved. Since the collision rate

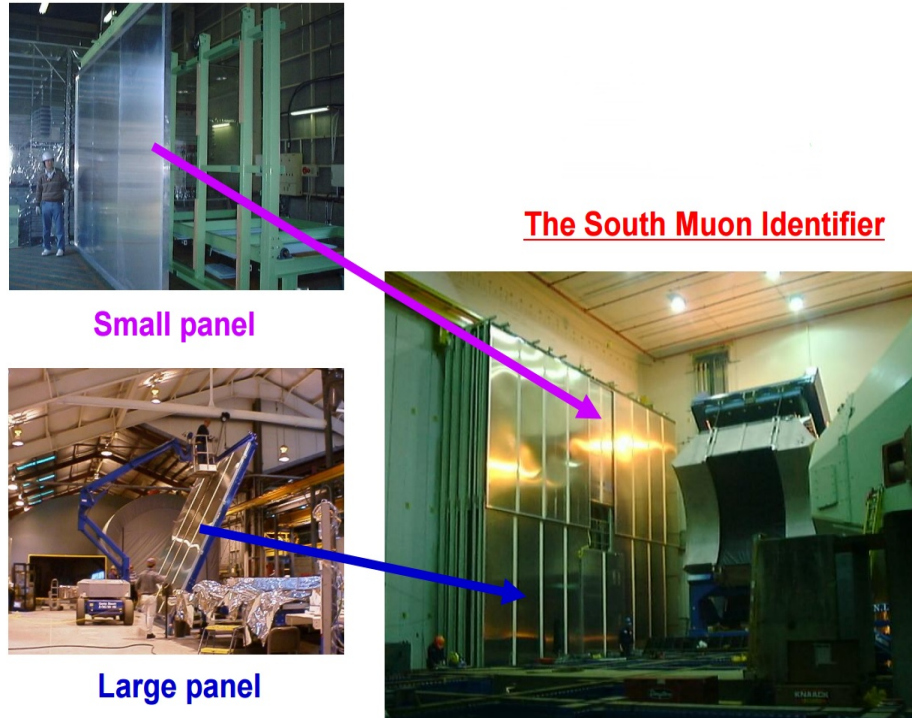


Figure 2.14: South MuID [42].

was very high for PHENIX run 13 proton-proton collisions, it is important to have fast timing to avoid recording hits from adjacent bunch crossings. Therefore RPCs provide the required fast timing resolutions to differentiate bunch crossings. More information on MuTr, MuID and RPC can be found in Reference [45].

2.2.5 Data acquisition (DAQ) and triggering

PHENIX detector system is designed to make measurements on a variety of colliding systems such as proton-proton (p-p) and Au-Au. The detector occupancy for p-p interactions is to approximately 10% of all detector channels in central Au-Au

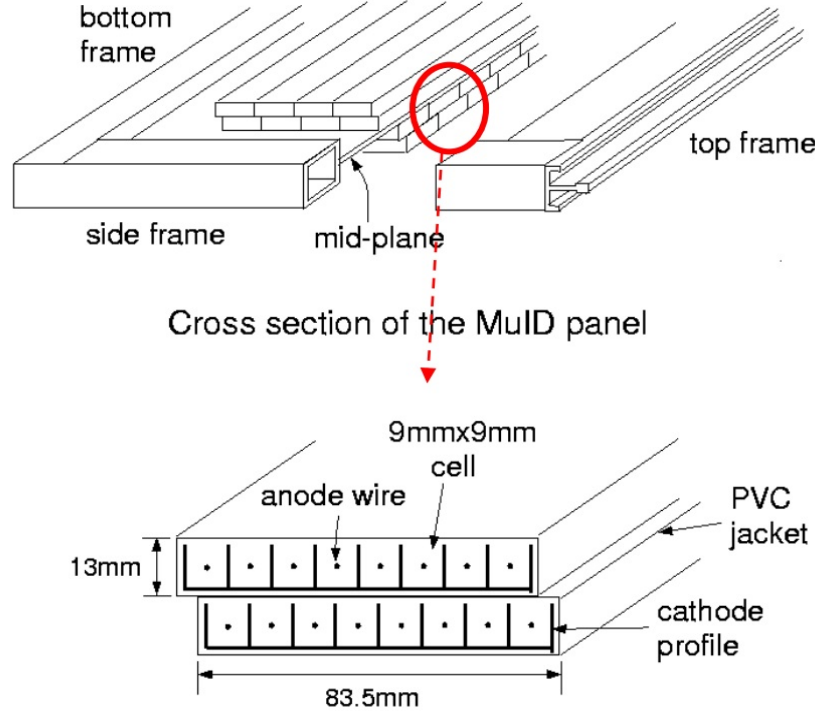


Figure 2.15: Iarocci streamer tubes in the MuID [42].

interactions. For Au-Au central collisions, the luminosity is few kHz whereas for the minimum bias p-p collisions it is approximately 500 kHz [47]. Therefore the PHENIX DAQ is compatible to the different collision rates and track multiplicities. Figure 2.17 shows the overview of PHENIX DAQ system.

However it is impossible to obtain data from the maximum collision rate of RHIC of collisions (RHIC clock ~ 9.4 MHz) to disks due to bandwidth and storage constraints. Even if we could record all the data, most of the events would be uninteresting for the particular physics analysis. Therefore the purpose of triggering subsystems is to reduce the large amount of data down to rates that can be prac-

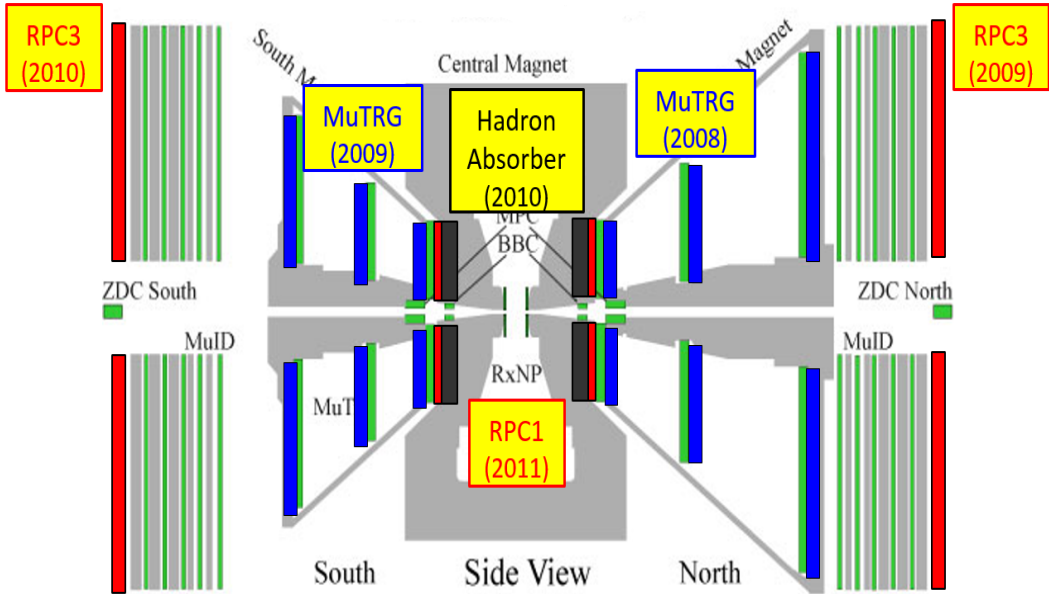


Figure 2.16: Positions of the planned RPC stations, RPC1(a,b), RPC2, and RPC3 [46].

tically stored to disk without blindly rejecting events that have a high probability of being interested rare process with a certain event topology. The PHENIX data acquisition system is capable of committing event data to disk approximately at 6 kHz rates where roughly 1.2 GB of data storing to disk every second and leads to multiple petabyte data sets.

Front End Electronics (FEE) process signals from the various PHENIX subsystems and convert detector signals into digital event fragments by analog-to-digital conversion (ADC) and timing-to-digital conversion (TDC). As shown in Figure 2.17, the RHIC clock is received by the PHENIX Master Timing Module (MTM). Then MTM distributes the clock to Global Level-1 Module (GL1) and Granule

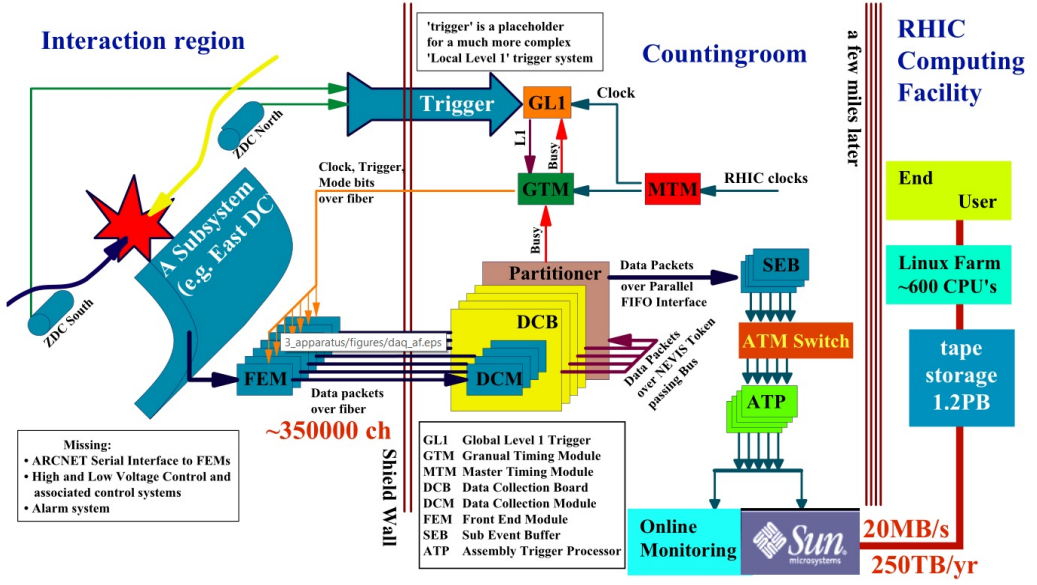


Figure 2.17: PHENIX DAQ system [47].

Timing Modules (GTM) which forwards the clock to FEMs. GL1 manages Local Level1 triggers (LL1) which are provided by user to determine if an event is interesting for a given subsystem. Once the clocks are synchronized, if LL1 conditions are satisfied and GTM is not busy , GL1 issues a trigger signal to the GTMs. Each GTM transmits to its FEMs. FEM digitizes the corresponding timing event data and sends it to the Data Collection Module (DCM).

Parallel DCM signals are passed to the Sub Event Builder (SEB) and onto the Assembly and Trigger Processors (ATP) after quality assurance and signal reprocessing are done in DCM. Data passing all the above conditions are then passed to the PHENIX On-line Control System (ONCS), where it is further processed and stored for eventual offline analysis. More details of the data taking procedure

are outlined in Reference [47] and [48].

Minimum bias triggers (MBtrig) provide the minimum requirement to record the data from a given beam crossing to disk that ensures a collision has occurred. Both the BBC and ZDC are capable of such a detection. The BBC minimum bias trigger requires a hit recorded at least one PMT in each arms on either side of the interaction point in order to issue the trigger bit. Further selection can be done on the roughly determined vertex position of the collision. Three triggers are provided by BBC according to the vertex position of the collision. They are called BBCLL1(> 0 tubes) novertex, BBCLL1(> 0 tubes) and $|z_{\text{vtx}}| < 30$ cm and BBCLL1(> 0 tubes) and $|z_{\text{vtx}}| < 15$ cm. PHENIX central and muon arms only have a nominally stable acceptance when the collision occurs within 30 cm of the interaction point. The minimum bias (MB) triggers are used to monitor the luminosity and assign the collision to its timing.

MuID Local Level 1 Trigger (MuIDLL1) provides the ability to trigger in the presence of highly penetrating charged particle tracks. The most probable trajectory of the particle follows the line connecting a collision vertex to a hit at gap-1 logical tube. The logical tubes in the other gaps which intersect with the line are grouped as a set called *symset*. Two symset logic conditions are provided namely “1D (one-deep)”, which is used for identifying muons, and the “1H (one-hadron)”, which is used for identifying hadrons. 1D algorithm requires at least

one hit in the MuID gap-3 or the gap-4, while the 1H algorithm requires no hits in the gap-4. To trigger on the possible presence of a dimuon, 2D (two-deep) condition is formed that requires two separate logical subsets of the MuID trigger subsystem to have 1-D condition. However 2D trigger also considers the opening angle between the two tracks. Generally, the MuID triggers are used with a BBC trigger which will correctly identify the crossing with a collision since the timing window of MuID only is two beam crossings wide. However, if two collisions occur in two adjacent crossings then there will be ambiguity as the BBC will fire for both crossings even though only one will contain the true muon trigger. Therefore by using RPC and MuID trigger combinations can remove such ambiguities since RPC detector add precision timing information. In addition to the MuID and RPC, the MuTr is also used as a trigger to select muon candidates having a particular sagitta, or deviation from a straight track at an intermediate tracking station. Hence MuTr adds momentum selection to the trigger.

3 FORWARD VERTEX SILICON DETECTOR (FVTX)

FVTX detector was designed and installed at PHENIX Experiment as a result of the forward upgrade programme. It was designed to have the same acceptance coverage as the muon arms which covers over a pseudorapidity range $1.2 \leq |\eta| \leq 2.2$ with full azimuthal coverage.

A hadron absorber is located in front of the Muon Tracker detector (MuTr) which removes most of the initial particles before reaching the MuTr which is the main tracking detector. This severely limited the event information. But now FVTX allows us to measure all particles near vertex since it is located very close to the interaction point and before the absorbers. Further FVTX can ensure track origins and can cleanly identify source of single leptons. Before the FVTX was installed, it was difficult to identify mis-reconstructed tracks since we were observing a minimal track hits in Muon Tracker. However now FVTX provides more track hits for track reconstruction along flight path which substantially reduce the mis-reconstructed tracks. Further FVTX can be used to determine Event vertex and monitor the Luminosity.

In this chapter, detector overview, electronic and mechanical design of the detector, data acquisition procedure and tracking method are discussed for the FVTX detector. Further tracklet activity, which is one of the main tools used for Drell-Yan analysis is discussed in this chapter.

3.1 Detector overview

The FVTX detector system is composed of two identical endcap sections as shown in Figure 3.1. Each of them are located on either end of a four-layer barrel silicon vertex detector (VTX) [50] and in front of the north and south muon spectrometer arms. Four layers of active silicon sensors are arranged in disks (also known as stations) around the beryllium beam pipe for each endcap. Wedge is the basic

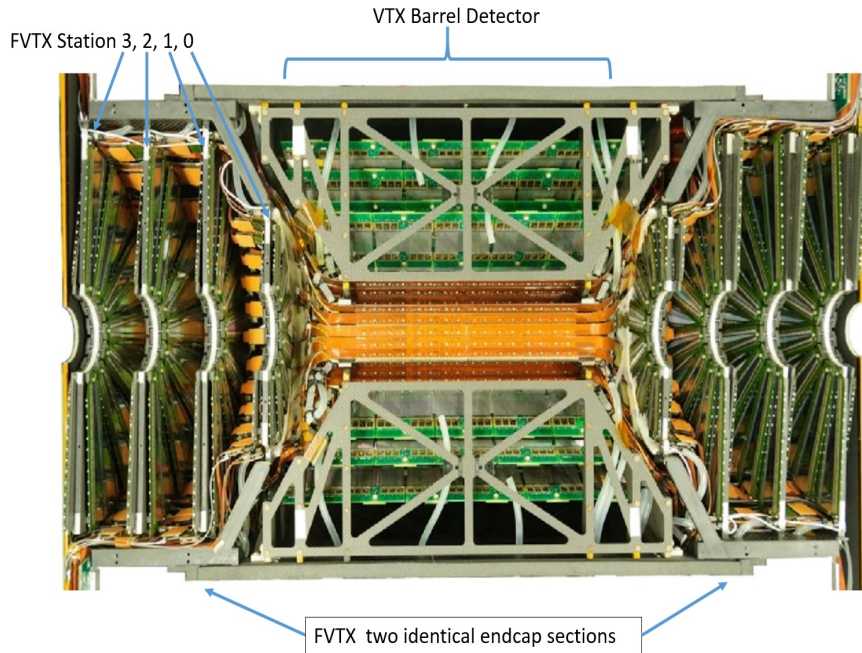


Figure 3.1: Half-detector, with the VTX barrels in the center, and the two FVTX endcaps on either end.

unit of construction. Wedges are mounted on half-disks, and fitted with extension cables. As can be seen in Figure 3.1, each cage has one small and three large disks. The smaller disks are simply truncated versions of the larger disks [51]. The disks

are mounted into cages, and the extension cables are connected to Read-Out Cards (ROC boards). A summary of the FVTX design parameters is given in Table 3.1.

Table 3.1: Summary of design parameters

Variable Name	Value
Silicon sensor thickness	$320 \mu m$
Strip pitch	$75 \mu m$
Nominal operating sensor bias	+70 V
Strips per column for small, large wedges	640, 1664
Inner radius of silicon	44 mm
Strip columns per half-disk (2 per wedge)	48
Mean $z-$ position of stations (mm)	$\pm 201.1, \pm 261.4$ $\pm 321.7, \pm 382.0$
Silicon mean z offsets from station center (mm)	$\pm 5.845, \pm 9.845$

3.2 Detector components and their functionality

This section describes the electrical and mechanical components and the read out system of FVTX detector.

3.2.1 Wedges

As mentioned in Section 3.1, wedge is the basic construction unit of the FVTX detector. Figure 3.2 shows a picture of the wedge in the left side and a schematic diagram of the exploded view of a single wedge assembly in the rightside. A wedge consists of a silicon mini-strip sensors, FPHX read-out chips, a high-density inter-connect bus (HDI) and a carbon support backplane. All the wedges were assembled at the SiDet Facility at Fermilab. Each wedge comprises of two individual

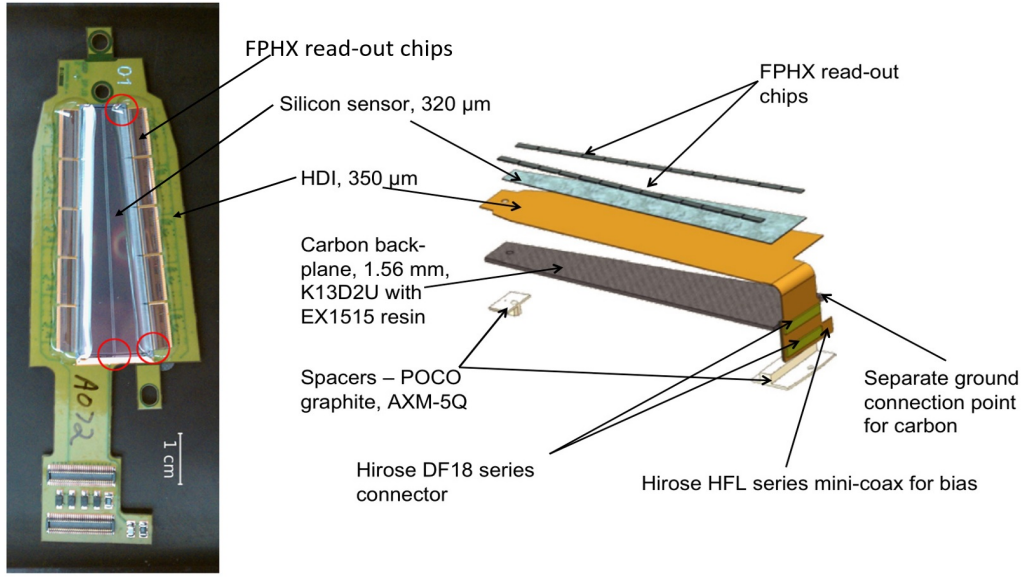


Figure 3.2: Wedge and schematic diagram of its structure.

columns of Silicon mini-strip sensors that are mirror images about the center line on the same sensor. The centerline gap between columns is $100 \mu\text{m}$ and it is completely active. At the outer edges of the sensor, wire bond connections between the strips and read-out chips (FPHX) are located. The strip length increases from inner radius of the sensor to outer radius from 3.4 mm to 11.5 mm with a pitch of $75 \mu\text{m}$ in the radial direction. Each sensor covers 7.5° in ϕ where 48 wedges cover the whole azimuth.

FPHX is a application-specific integrated circuit (ASIC) with 128-channels designed by Fermilab for the FVTX detector. The chip was fabricated by the Taiwan Semiconductor Manufacturing Company (TSMC) with $0.25 \mu\text{m}$ CMOS technology [51]. FPHX chips are optimized for fast trigger capability, a trigger-less

data push architecture, and low power consumption. They can be programmed via an LVDS serial slow control line with the setup parameters. The FPHX chip was designed to process up to four hits within four RHIC beam crossings where each hit contains a 7-bit time stamp, a 7-bit channel identifier, and a 3-bit ADC value. The signal-to-noise ratio can be greatly optimized for different operating conditions by only accepting hits above a certain (programmable) ADC threshold. Further, the ADC information from strips in an FVTX hit cluster is used to determine the center of the track using a weighted average of the charge in each strip.

FPHX read-out chips and the sensor are assembled on High-density interconnects (HDI). HDI provides the slow control, power and bias input lines and the data output lines.

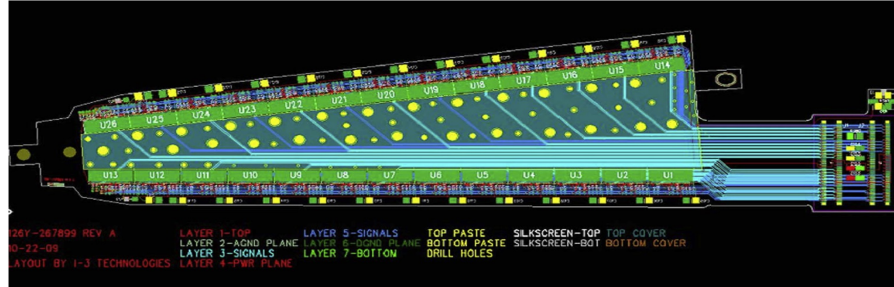


Figure 3.3: Schematic of the HDI stack-up [51].

As shown in Figure 3.3, HDI stack-up consists of seven layers of single sided ($20 \mu m$) and double sided ($50 \mu m$) copper coated polyamide bonded together with a $25 \mu m$ sheet adhesive for a total thickness of approximately $350 \mu m$ [51]. The

layout of the wedge, chip, and HDI can impact the system noise. Therefore the electrical layout of the wedge assembly was designed to minimize any additional noise using two noise canceling loops by employing bypass capacitors connected to the bias ground and the digital ground. All signals from the HDI are brought to ROC board by the extension cables. Extension cables are also designed to bring power from the ROC board to the wedge, and have a similar stack-up design to the HDIs.

3.2.2 Disks and Cages

As can be seen in Figure 3.4 (a), disks are flat sheets of 0.4 mm thick thermally conductive carbon fiber on both sides of a carbon-loaded PEEK plastic frame. The PEEK at the outer radius contains a cooling channel which removes the heat generated by the FPHX chips. Precision alignment pins are located along the inner and outer radii of both sides of the disks in order to mount the wedges on both sides of the disks. Adjacent wedges on a disk overlap in the azimuthal direction by 0.5 mm to give hermetic coverage in the azimuthal direction as shown in Figure 3.5 (a). Mounting wedges on both sides of the disks is required to have a continuous azimuthal coverage by the sensors as the HDI is significantly wider than the silicon sensor. The positions of the wedges were precisely measured by Hexagon Metrology in Rhode Island after each disk was fully populated with wedges. Disk cooling tubes, bias voltage coaxial cables and the extension cables

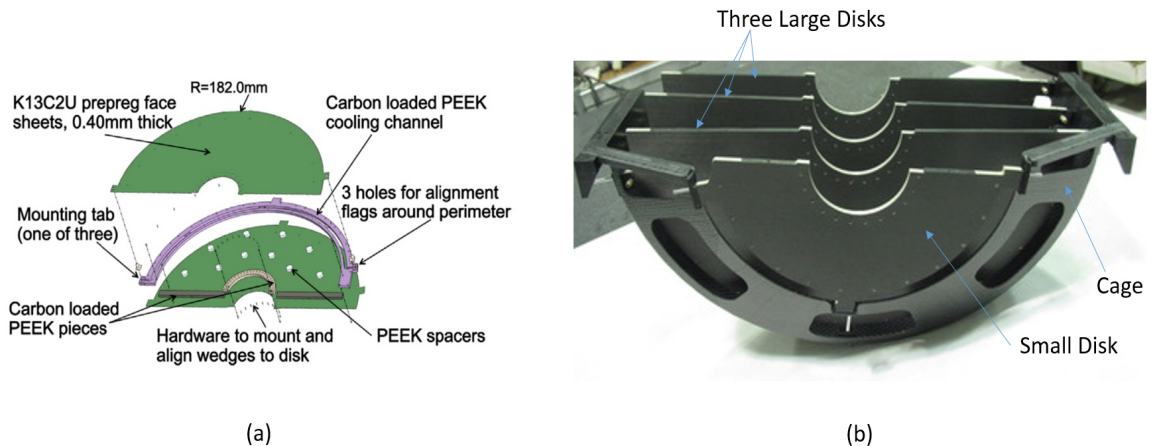


Figure 3.4: (a) Exploded view of a disk. (b) A cage with all four disks installed. No wedges have been placed on the disks

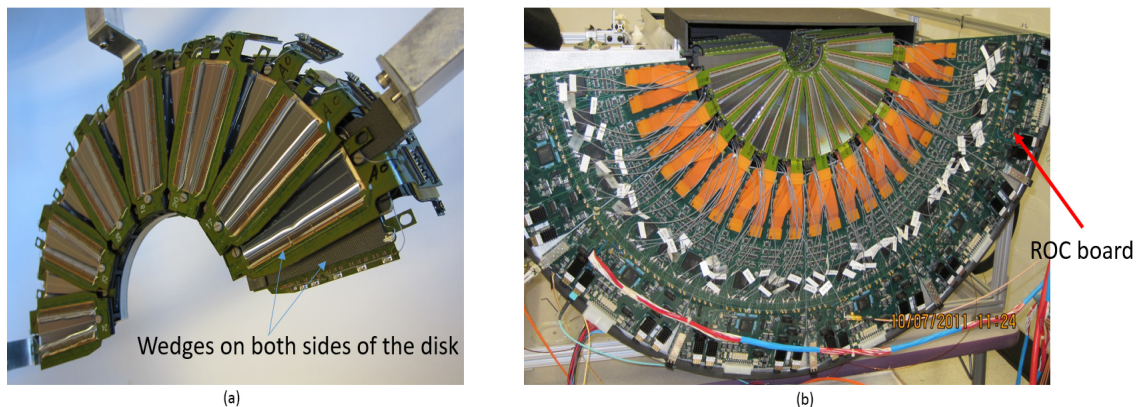


Figure 3.5: (a) Wedges assembled on to a disk (b) Completed North West section of the detector

were connected before a disk was mounted into a cage. Then the disks were mounted into a cage on the three precision mount points located on the outer radius of the disk. To maximize the detector's ϕ resolution, each of the four disks are mounted into the cage offset in ϕ by an angle $3.75^\circ/4$ with respect to the neighboring disk [51].

A cage as shown in Figure 3.4 (b), is a carbon composite structures fabricated from CN60 carbon fabric (Nippon Graphite Fiber) with EX1515 resin. As can be seen on Figure 3.5 (a), a cage was mounted in an assembly structure that also supported the aluminum cooling plate onto which the ROC boards are mounted. A soft material which is approximately 1/8 inches thick, is placed between the ROC board and the cooling plate to improve heat transfer.

3.3 FVTX data acquisition system

As shown in Figure 3.6, data from the silicon sensor and FPHX read-out chips are sent through HDI data output lines and the extension cables to the ROC board. The design of the read-out electronics for the FVTX detectors is based on three major constraints. They are large instantaneous bandwidth (3.38 Tb/s), radiation hardness of read-out components near the interaction point and the large number of I/O lines (21000 LVDS pairs). Therefore the read-out electronics are logically divided into two independent blocks, module which is located close to the detector (ROC) and module which is located in the Counting House (Front End Module).

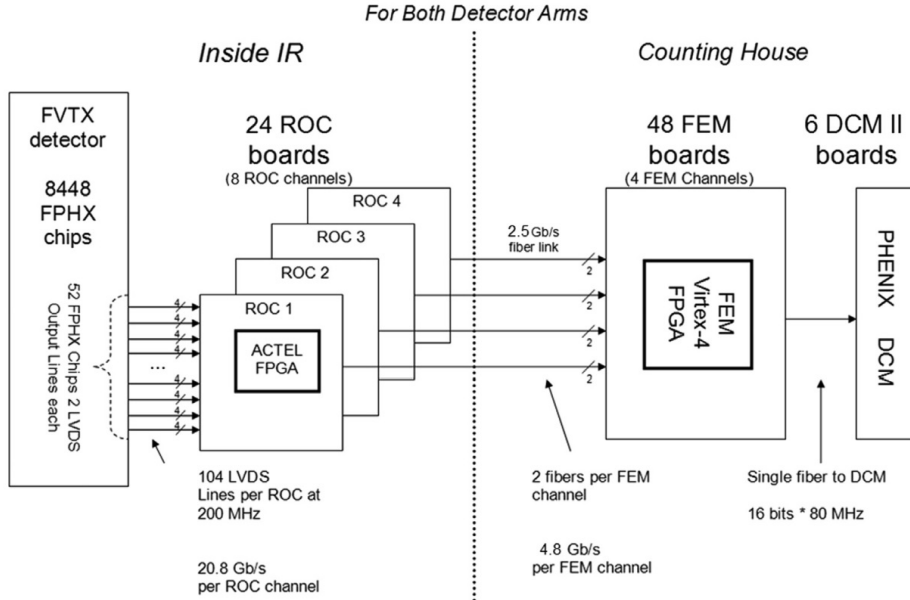


Figure 3.6: Read-out electronics block diagram [51].

The output of the Front End Module (FEM) connects to the standard PHENIX DAQ board called Data Collection Module (DCM). From this point on the data stream becomes a part of the standard PHENIX DAQ.

3.3.1 Read Out Card (ROC)

The ROC boards receive data via LVDS pairs from the silicon read-out chips and combine and synchronize the data streams from multiple FPHX chips. The ROC hold an on-board calibration system for the FPHX chips and on-board JTAG FPGA which allows for remote programming of the slow control and data FPGAs.

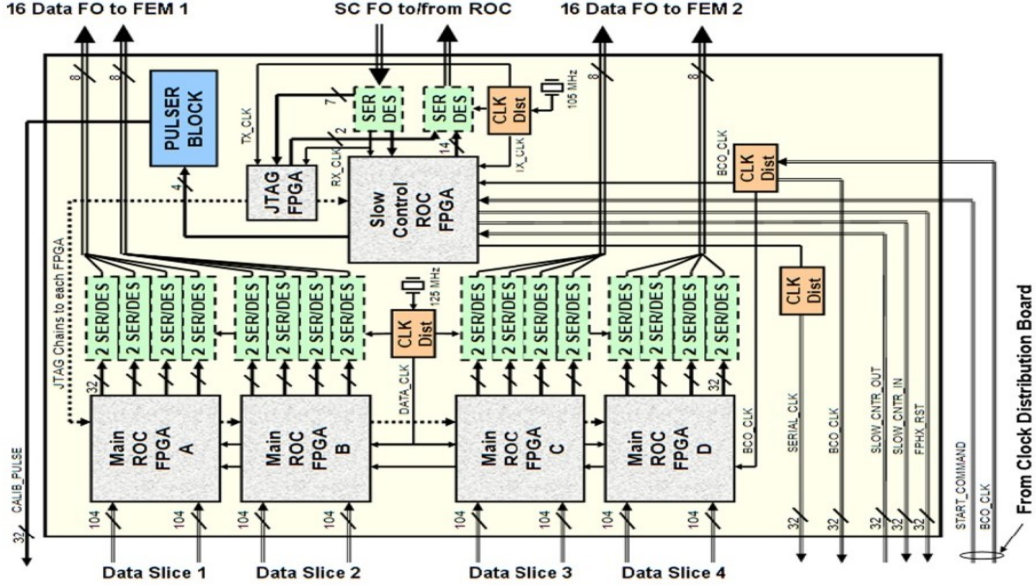


Figure 3.7: Block diagram of the ROC board [51].

A block diagram of a ROC board is shown in Figure 3.7. Each board contains 4 large-scale radiation-hard FLASH-based ACTEL A3PE3000-FG896 FPGAs to process the data from the read-out chips, 33 16-bit Serializer/Deserializer chips (TLK2711) and four 12-channel optical fiber transmitters (HFBR-772BEZ) to send the data to 2 FEM boards. Each ROC FPGA holds two completely independent ROC channels, for a total of 8 ROC channels per board, which send out 32-bit data at the output clock frequency of 125 MHz. The Beam Clock (9.4 MHz) arrives at the ROC board as an LVDS signal and is distributed to all the FPGAs on the board as well as to all the FPHX chips. A Serial Clock of $20 \times$ the Beam Clock frequency is generated by a PLL on the slow control FPGA. The output data from the FPHX chips are phase latched to a similarly generated $20 \times$

clock inside the Main FPGAs, which avoids distribution of the fast clock between FPGAs and simplifies the design [51].

3.3.2 Front End Module (FEM)

The FEM boards are located in the counting house which is a shielded location \sim 50 meters from the detector where radiation levels are negligibly small. Hence SRAM-based FPGAs can be used. The FEM boards are functionally designed to receive data from the ROC boards over fiber links and sort the incoming data according to the Beam Clock Counter. Further it buffers the data from the last 64 beam clocks and ship the data from the Beam Clock of interest to the output buffer, which then ships data to the PHENIX Data Collection Modules (DCM) upon the Level-1 trigger decision. FEM Distribute and receive slow control data to/from the ROC cards. The online slow control interface is made through the FEM Interface Board and the interface to the ROC cards is made through an optical fiber. The FEM board architecture is shown in Figure 3.8.

3.4 Tracking

Charged particle tracks typically traverse the silicon planes at angles of 10° to 30° with respect to the normal and the charge deposited in the silicon is shared between strips according to the track length under each strip. Usually a track traverses a cluster of 1 to 4 adjacent strips since the silicon is $300 \mu m$ thick with

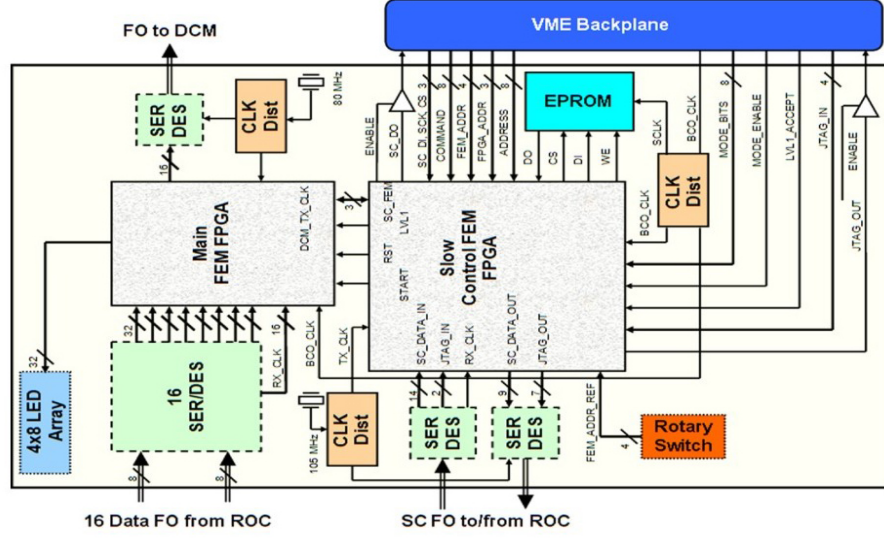


Figure 3.8: Block diagram of a FEM board [51].

segments of $75 \mu m$ strips. The cluster size distribution for particles thrown into the acceptance of the FVTX is shown in Figure 3.9 (a).

The average number of tracks in each endcap for proton-proton collisions is only about 2.4 (hit occupancy .008%). Thus the probability that hit clusters could overlap from different tracks is exceedingly small. A hit location within a cluster is calculated from the mean of the strip locations in a cluster of hit strips. The resolution of 3 wide clusters is approximately $10 \mu m$ as shown in Figure 3.9(b).

In order to filter the recorded hit information into tracks passing through the detector, the pattern recognition algorithms are used. The ideal algorithm would associate all of the hits deposited by a single charged particle into a track and leave unrelated hits to the track. But ideal algorithms are not practically feasible due

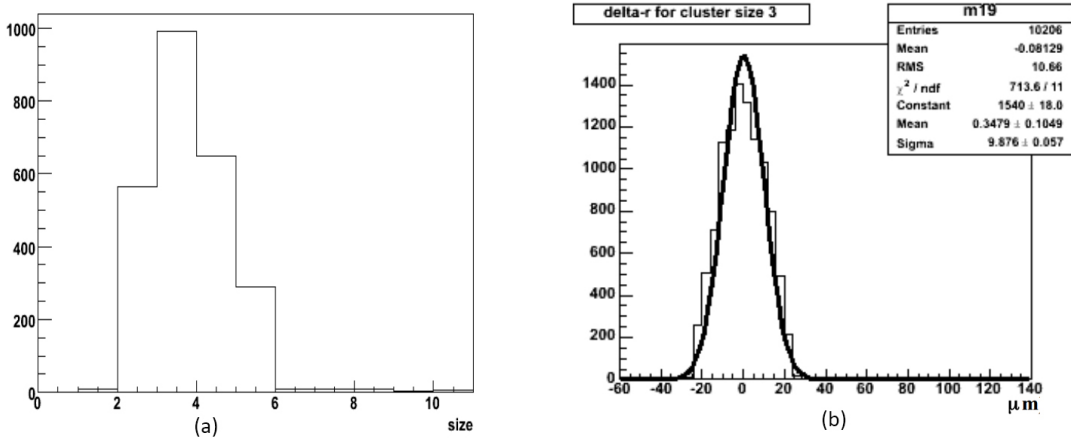


Figure 3.9: (a) The cluster size for a distribution of particles thrown over the FVTX acceptance. (b) The resolution of the found cluster centroids for 3 wide clusters (approximately $10 \mu\text{m}$).

to the finite computing resources. However a realistic algorithm must be efficient and must have a balance between maximizing the number of true tracks found while minimizing the contamination from the fake tracks formed from random combinations of hits that have no true relationship.

Since the FVTX is located within a magnetic field where the field lines are approximately axial along the beam axis, the charged particles passing through the FVTX travel along paths that are roughly parallel to the magnetic field with a minimal bending. The multiple scattering of the particle as it passes through the detector is also assumed to be small. Therefore, if we assume that the particles are traveling in a straight line, the Hough transform [57][58] is a highly efficient pattern recognition algorithm to extract straight line features from images or point clouds. As can be seen in Figure 3.10, a candidate track (tracklet) can be reconstructed

using Hough transform which requires atleast three hits in the FVTX or two hits in FVTX plus the vertex position. After the candidate tracks are found, they are passed to a Kalman Filter track fitter which sends tracks through the known materials and magnetic field and produces track fit parameters at the nominal vertex. Tracks which are below a given track quality, determined by the fit results and the number of hits, are eliminated.

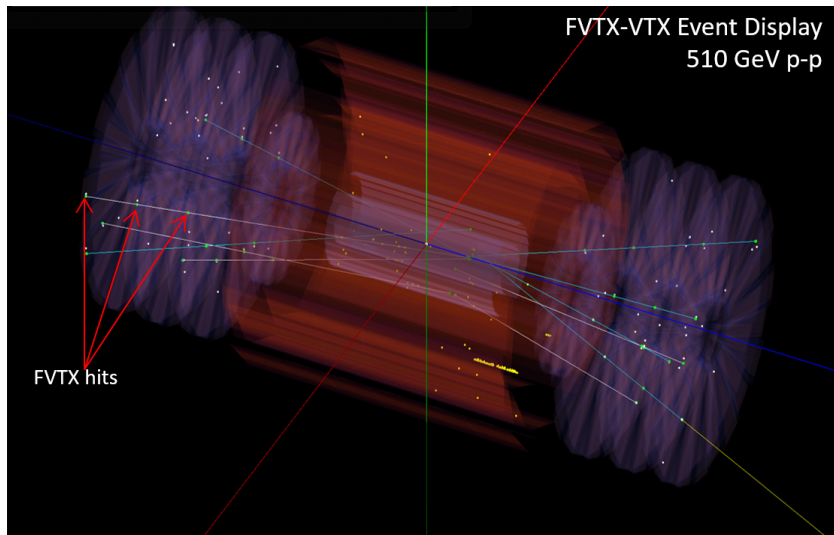


Figure 3.10: FVTX + VTX event display for a p+p collision.

The vertex within 10 cm provides the most efficient tracking through FVTX. But one can even extend the tracking to a vertex range that includes particles originating from outside of the detector volume ($|z| > 30$ cm) due to high computational efficiency of the Hough transform algorithm. Further the tracking acceptance can be expanded by using the hits from the adjacent barrel vertex detector (VTX) combined with the FVTX hits as shown in Figure 3.11.

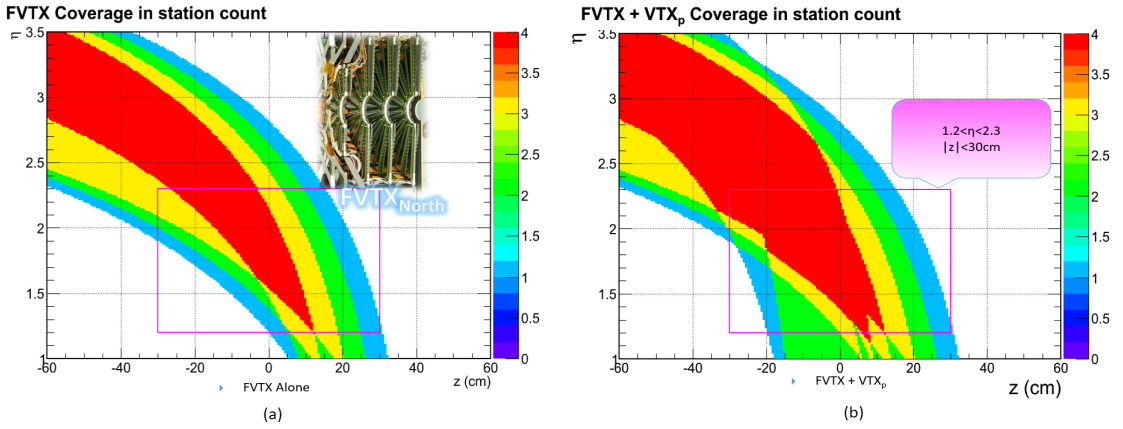


Figure 3.11: (a) FVTX coverage for North Arm. (b) Coverage after combining FVTX and VTX.

FVTX tracklets also can be used to measure the vertex positions for each bunch crossing by examining the tracklet origins. With the current tracking enhancements, FVTX has demonstrated the ability to reconstruct up to 5 event vertexes from a single crossing and correctly associate reconstructed tracks with each vertex up to $|z| < 150$ cm.

3.5 Tracklets for Drell-Yan analysis

In this analysis, the FVTX tracklets were used as a tool to estimate the signal fraction in the data sample. For a jet like heavy flavor event more tracklets are expected than the Drell-Yan event as shown in Figure 3.12.

The tracklet selection for the analysis was done according to two criteria. The first criteria was that the tracklets must be pointing to the primary vertex. This

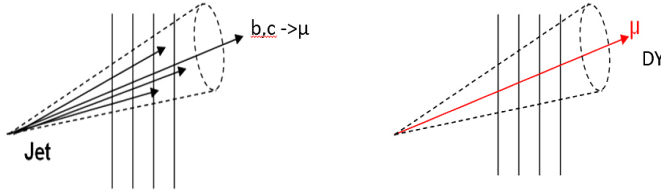


Figure 3.12: Activity around the muon track from jet like event and Drell-Yan event.

was done in Cartesian coordinates by:

(a) Extrapolate the tracklets on to the xy plane at z is equal to the primary vertex location (z_0). Then find the x (x_0) and y (y_0) coordinates. If we know the coordinates and the polar and azimuth angles of a point on the tracklet (x, y, z, θ, ϕ), x_0 and y_0 can be measured as

$$x_0 = x - (z - z_0)\tan\theta\cos\phi \quad (3.1)$$

$$y_0 = y - (z - z_0)\tan\theta\sin\phi \quad (3.2)$$

(b) Find the distance (R) from primary vertex to the tracklet in the xy plane at z is equal to the primary vertex location

$$R = \sqrt{(x_0 - x')^2 + (y_0 - y')^2} \quad (3.3)$$

where x' and y' are the primary vertex coordinates.

(c) Select the tracklets with $R < 1.5$ cm. As an example the y_0 vs. x_0 before and after a $R < 2.0$ cm is shown in figure 3.13

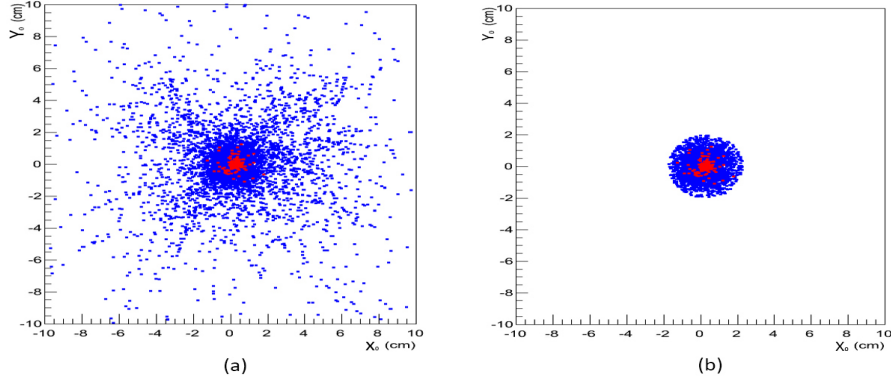


Figure 3.13: The y_0 vs. x_0 graph (a) before and (b) after the $R < 2$ cut.

If we plot the tracklet rapidity vs. track rapidity, we will see a correlation as can be seen in Figure 3.14 (a) since the muon track is also a tracklet. Therefore the second criteria was that the tracklets must not be a reconstructed muon track from the dimuon pair. The plot of tracklet rapidity vs track rapidity after removing the tracks from the tracklets are shown in Figure 3.14 (b).

The tracklet distribution for dimuon events in the J/ψ mass region was studied in order to check whether the tracklet distribution simulations represent the real data. The same quality cuts which are discussed in Section 5.1 were used in order to obtain the plots in Figure 3.15. As can be seen in Figure 3.15, the real data tracklet distribution agrees with the simulated J/ψ tracklet distribution to a greater extent. Therefore tracklet distributions were used as one of the main tool for extracting the signal fraction in the Drell-Yan analysis.

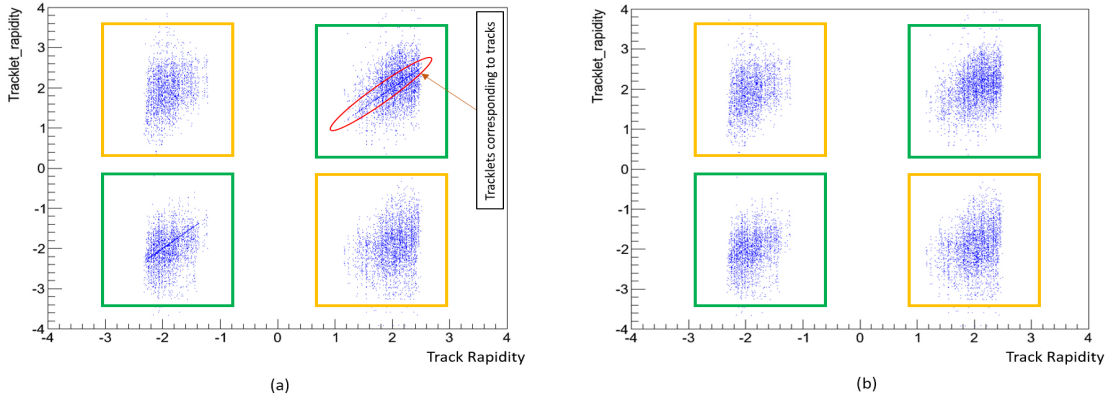


Figure 3.14: Tracklet rapidity vs track rapidity graph (a) before and (b) after removing the tracks from tracklets. Green box corresponds to same arm tracklets as the tracks while yellow box shows the opposite arm tracklets as the tracks.

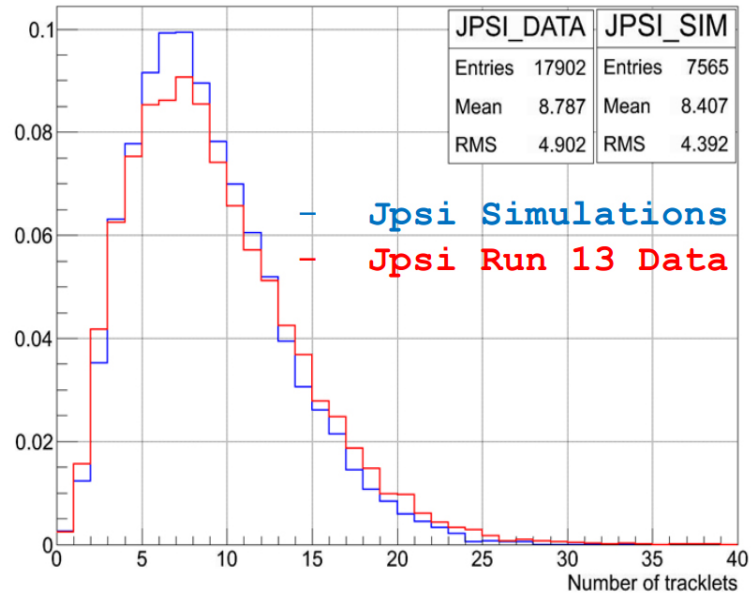


Figure 3.15: Tracklet distribution for J/ψ simulations and J/ψ data.

4 DATA AND SIMULATIONS

As mentioned in Section 1.5, this thesis analysis is based on the data from RHIC Run 2013 proton-proton collisions at $\sqrt{s} = 510$ GeV. Main priority of RHIC Run 13 was the forward W to μ measurements [53]. In parallel to the W -program, one of other goals was providing the first measurement of polarized Drell-Yan production at forward rapidity in PHENIX experiment. In this chapter details on Run 13 data and relevant simulations to the analysis are discussed.

In RHIC, the polarized protons are filled in both rings for the polarized proton-proton collisions. An optimal RHIC fill lasts eight hours. However it may be shorter or longer depending on circumstances. Each fill is identified by fill number associated to RHIC. Fill numbers from 17156 to 17601 were used for this analysis.

The PHENIX DAQ continuously collects online data from subsystems up to a maximum of 1.5 hours at a time. Each data taking unit is identified by a run number associated to PHENIX. Several runs occur during a RHIC fill. The runs can be categorized in to several groups depending on the purpose of collecting data. The runs which are used for physics analysis are called physics runs which usually consists of data taking from all subsystems. The zero field runs are taken every time before turning the magnets on and used to calibrate the alignment of muon arm detectors. Cosmic run data is taken before the physics run while beams are not filled in order to study cosmic backgrounds. Calibration runs are

also taken for each detector subsystem. In this analysis run numbers ranging from 386773 to 398149 are used after completing a quality assurance test which is described in Section 4.3.

4.1 Beam polarization and the integrated luminosity

As discussed in Section 2.1.3, the beam polarization is measured with H-jet polarimeter for absolute calibration and CNI polarimeter for relative profiling. The fill-by-fill beam polarization after correcting the absolute scaling for Run 13 is shown in Figure 4.1. The final average longitudinal beam polarization for the blue beam was $54 \pm 0.42\%$, and $55 \pm 0.40\%$ for the yellow beam for Run 13.

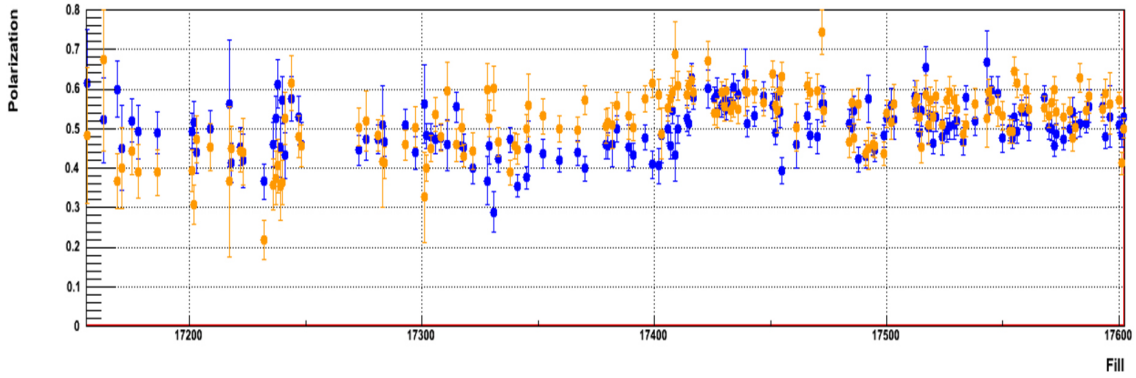


Figure 4.1: Fill-by-fill beam polarizations in year 2013 runs for the Blue beam and Yellow beam [54].

As discussed in Section 2.1.2, the polarization of the bunches are rotated into the longitudinal direction from its default transverse direction using the spin ro-

tators. Therefore we can have either positive helicity (+) or negative helicity (-) bunches according to the rotated longitudinal direction. As a result, spin patterns can be defined according to the helicity of bunch crossings as shown in Table 4.1 and Table 4.2.

Table 4.1: Spin patterns used in the initial part of Run 13 [55].

P1 BLUE:	+	+	-	-	+	+	-	-	+	+	-	-
YELLOW:	+	+	+	+	-	-	-	-	+	+	+	-
P2 BLUE:	-	-	+	+	-	-	+	+	-	-	+	+
YELLOW:	+	+	+	+	-	-	-	-	+	+	+	-
P3 BLUE:	+	+	-	-	+	+	-	-	+	+	-	-
YELLOW:	-	-	-	-	+	+	+	+	-	-	-	+
P4 BLUE:	-	-	+	+	-	-	+	+	-	-	+	+
YELLOW:	-	-	-	-	+	+	+	+	-	-	-	+
P5 BLUE:	+	+	+	+	-	-	-	-	+	+	+	-
YELLOW:	+	+	-	-	+	+	-	-	+	+	-	-
P6 BLUE:	+	+	+	+	-	-	-	-	+	+	+	-
YELLOW:	-	-	+	+	-	-	+	+	-	+	+	-
P7 BLUE:	-	-	-	-	+	+	+	+	-	-	-	+
YELLOW:	+	+	-	-	+	+	-	-	+	+	-	-
P8 BLUE:	-	-	-	-	+	+	+	+	-	-	-	+
YELLOW:	-	-	+	+	-	-	+	+	-	-	+	+

Table 4.2: Spin patterns for the later part of Run 13 [55].

P21 BLUE:	+	+	-	-	+	+	-	-	repeat
YELLOW:	+	+	+	+	-	-	-	-	repeat
P22 BLUE:	-	-	+	+	-	-	+	+	repeat
YELLOW:	+	+	+	+	-	-	-	-	repeat
P23 BLUE:	+	+	-	-	+	+	-	-	repeat
YELLOW:	-	-	-	-	+	+	+	+	repeat
P24 BLUE:	-	-	+	+	-	-	+	+	repeat
YELLOW:	-	-	-	-	+	+	+	+	repeat
P25 BLUE:	+	+	+	+	-	-	-	-	repeat
YELLOW:	+	+	-	-	+	+	-	-	repeat
P26 BLUE:	+	+	+	+	-	-	-	-	repeat
YELLOW:	-	-	+	+	-	-	+	+	repeat
P27 BLUE:	-	-	-	-	+	+	+	+	repeat
YELLOW:	+	+	-	-	+	+	-	-	repeat
P28 BLUE:	-	-	-	-	+	+	+	+	repeat
YELLOW:	-	-	+	+	-	-	+	+	repeat

For proton-proton collisions, luminosity can be defined as the particle yield per unit of the inelastic pp cross section. The integrated luminosity is used to refer to the time integrated luminosity which gives a measure of the number of collisions. Measuring the luminosity precisely is very important to spin asymmetry measurements which are made relative to the number of collisions. In PHENIX, the luminosity is monitored by BBC and ZDC detectors.

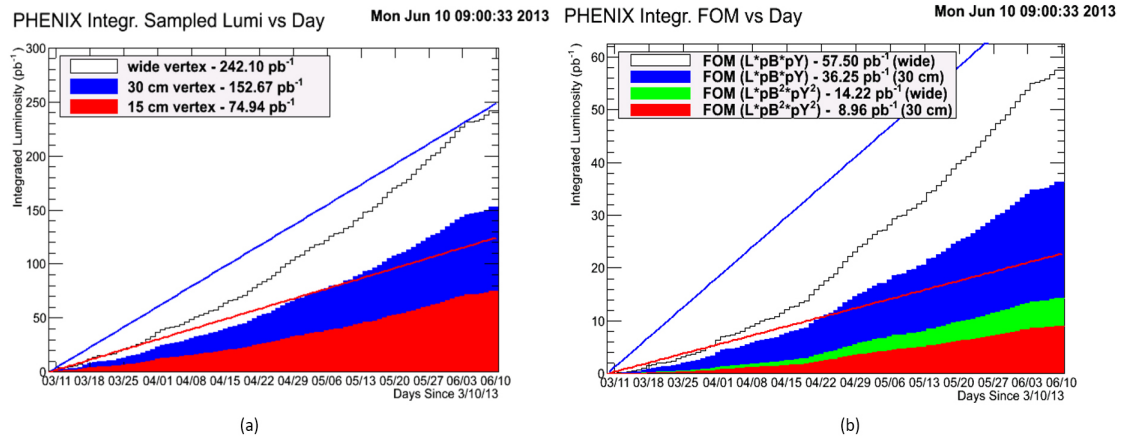


Figure 4.2: (a) Integrated luminosity vs. day for the Run 2013 at PHENIX. (b) Integrated figure of merit metric vs. day for the Run 2013 running period at RHIC.

As can be seen in Figure 4.2, the luminosity is measured for different vertex ranges at PHENIX. The integrated luminosity for wide vertex ($-150 \text{ cm} < z < 150 \text{ cm}$) case is $\approx 240 \text{ pb}^{-1}$, which is more than four times the total luminosity previously collected during Run 12 ($\approx 50 \text{ pb}^{-1}$). However for this analysis the

narrow vertex ($-30 \text{ cm} < z < 30 \text{ cm}$) luminosity was used which is $\approx 150 \text{ pb}^{-1}$.

4.2 Dimuon spectrum

In this study, we are only interested in the dimuon events detected in the same arm. The dimuon events can be categorized into three data sets according to their charge as shown in Figure 4.3. μ^{++} and μ^{--} events are called like-sign events and μ^{+-} events are called unlike-sign events. MUID 2D trigger discussed

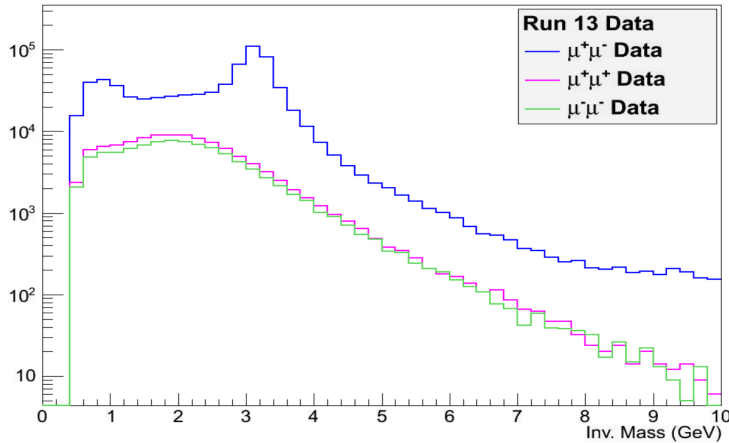


Figure 4.3: Dimuon spectrum for PHENIX Run 13.

in Section 2.2.5 was used to trigger on the possible presence of a dimuon. The trigger efficiencies for dimuon trigger for Run 13 are shown in Figure 4.4.

4.3 Quality assurance (QA)

It is important to perform a QA test before using the data for precision measurements. QA test ensures that conditions under which the data has been recorded

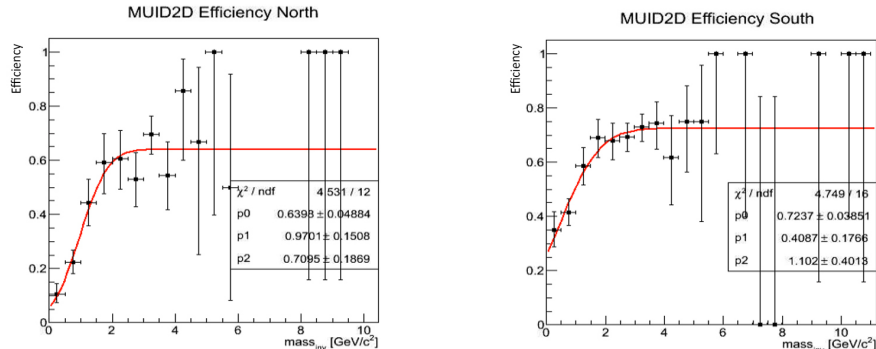


Figure 4.4: MUID 2D trigger efficiency for North and South arm separately.

remain stable. Many factors like humidity, atmospheric pressure and temperature affects the physical operating parameters of the detectors. And also the factors like collisions conditions, detector conditions and the beam quality affect the data quality. These conditions are monitored during the data taking period by monitoring the detectors and their output in real-time. However it is still important to quantify the reliability of the data through QA checks prior to the analysis.

It was needed to keep the data as much as possible since one of the main challenges for Drell-Yan measurements was the limited amount of statistics. And also, FVTX was required to work efficiently and correctly in order to use the tracklet activity for the precise measurements. Further for the asymmetry measurements, precise spin information was required. Therefore the runs given in Table 4.3 which did not pass FVTX quality assurance checks and the runs given in Table 4.4 which did not pass spin database quality assurance checks were removed from the data.

Table 4.3: Bad Run list from FVTX QA

386773	387027	387068	387081	387082	387083	387086	387128
387129	387131	387423	387424	387428	387564	387565	387666
387788	387801	387806	387969	388004	388020	388403	388537
388538	388690	388696	388723	388745	389254	389257	389904
389906	389907	389908	389909	390026	390029	390030	390031
390032	390033	390038	390039	390174	390175	390176	390230
390231	390232	390234	390236	390237	390239	390306	390313
390314	390315	390316	390318	390319	390418	390419	390421
390422	390423	390424	390425	390507	390511	390512	390515
390517	390613	392353	392354	392431	392712	392713	392714
392715	392716	392923	395102	395103	395223	395225	396563
396995	396997	396998	397702	398016	398027	398028	398029
398030	398031						

Table 4.4: Bad Run list from Spin QA

393164	393167	393175	393176	393177	393178	393179	393180
398005	398007	398009	398010	398011	398012	398013	398014
398017	398018	398019	398020	398026	398027	398028	398029
398030	398031						

4.4 Simulation

Precise simulation is the key to understand the real data correctly. Therefore Drell-Yan, J/ψ and ψ' full events were generated using PYTHIA 6 [56] particle generator. And also, Minimum Biased simulation was run in order to properly sample beyond leading-order heavy flavor production channels in PYTHIA6, including flavor excitation and gluon splitting. Production of the Minimum Biased simulations was highly time taking. It was roughly calculated that atleast 1000 cpu

years were needed to achieve enough simulation statistics which will match with the Run 13 data luminosity. Therefore the Open Science Grid, high throughput computing resource was used for the event generation. The integrated luminosity achieved for each process in PYTHIA production is given in Table 4.5.

Table 4.5: Total integrated luminosity produced for each simulated sub-processes using reference run 393888.

Process	Total Integrated Luminosity Achieved
Drell-Yan	1192.4 pb^{-1}
Minimum Biased	141.7 pb^{-1}
ψ'	147.6 pb^{-1}

Simulated proton-proton collisions produced in PYTHIA6 were then fully propagated through full detector simulation called PISA. PISA (PHENIX Integrated Simulation Application) is based on the GEANT3 framework [59]. All detector geometries, materials and fields are implemented in the PISA and the interaction of particles with matters and particle decays are simulated. Output from the PISA contains the detector hit data. Then the simulated detector hit data were processed by the same reconstruction codes as those used for the real data. The stack plot of invariant mass distributions of simulations and Run 12 data scaled to a luminosity of 200 pb^{-1} for south arm is shown in Figure 4.5. As can be seen in Figure 4.5, contributions to correlated unlike-sign dimuons mainly come from heavy flavor decays ($b\bar{b}$ and $c\bar{c}$) and Drell-Yan process for the intermedi-

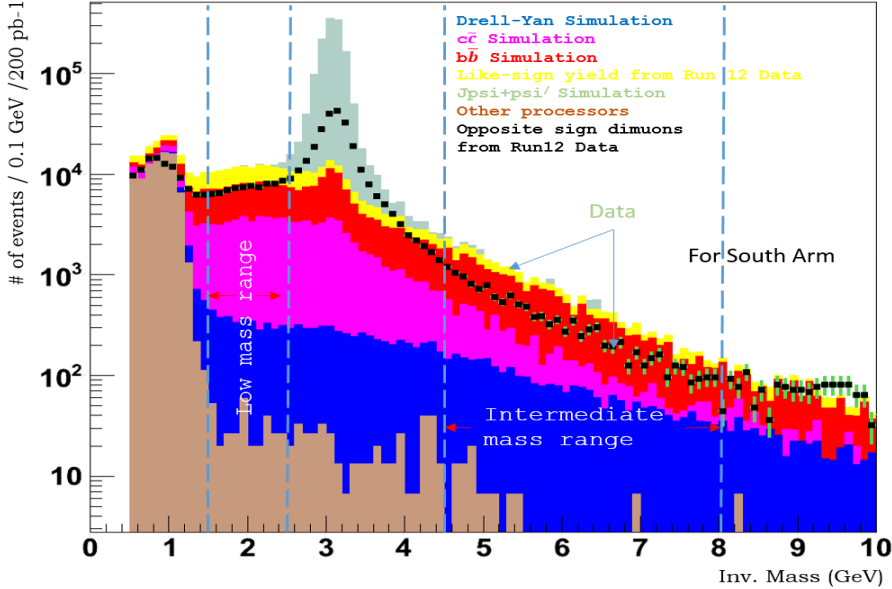


Figure 4.5: Stack plot of unlike-sign dimuon invariant mass distributions scaled to a luminosity of 200 pb⁻¹ for South arm.

ate mass region. However in a high multiplicity experimental environment, there can be random muon pairs also created, which are called as combinatorial backgrounds or uncorrelated backgrounds. In Figure 4.5, combinatorial background was estimated using the like-sign dimuon pairs. The data from Run 12 are off by a factor of few from the simulation mainly due to the differences in trigger efficiency between data and simulations and less precise PYTHIA cross-sections. More information about combinatorial background estimation and the decomposition of real data in to different processes are discussed in Chapter 5.

5 MEASUREMENT OF DRELL-YAN SIGNAL FRACTION

Drell-Yan signal fraction can be defined as the number of Drell-Yan events over all the dimuon events that passed a given set of cuts in the data. It is required to extract the signal fraction as well as the background fractions with the highest possible precision for a precise asymmetry measurement. The relationship between the signal fraction and the asymmetry is discussed in detail in Chapter 6.

Most common variables which are used to determine the signal fraction in a dimuon data sample are invariant mass and momentum. As an example, J/ψ signal to background ratio can be measured easily from a fit by looking at the invariant mass spectrum and observing the J/ψ peak over the background. However, invariant mass distributions of the muon pairs from the Drell-Yan process and other background processes are continuum in the intermediate mass region (4.5 GeV to 8.0 GeV). And also the momentum and most of other kinematic variables of the signal are rather similar to the backgrounds in this mass region. Because of that it is hard to differentiate the background processes from the Drell-Yan process using these variables alone. Hence new methods were studied to find the signal and background fractions. Such methods and the final result for the Drell-Yan signal fraction are discussed in this chapter.

5.1 Basic event selection criteria

After a careful quality assurance check as discussed in Section 4.3, basic cuts were needed to select the events for the analysis. Most of the basic event selection cuts were track matching cuts which measure the degree of matching of a track from one detector to another detector or to vertex. These cuts reduced the noise and background under the intermediate mass region and ensured that we only chose true muon candidates as much as possible for our analysis. The kinematic variables, their description and basic muon cuts used in this analysis can be listed as follows.

- $DG0 < 20$: Distance between the projected MuTr track and the MuID road at the gap 0 z position in cm.
- $DDG0 < 8$: Deviation of the slopes of the MuTr track and the MuID road at the gap 0 z position in degrees.
- $\chi^2 < 10$: Track fit quality which describes the quality of the fit to the MuTr and MuID hits
- $\text{MuID hits} > 6$: Number of MuID hits recorded
- $\text{MuTR hits} > 10$: Number of MuTr hits recorded
- $\text{vertex } \chi^2 < 4$: Track fit quality to the primary vertex

- $\text{lastgap} > 3$: MuID gap that the muon penetrates which ensure muons going through all MuID steel
- $|p_z| > 2$: Track momentum along z direction which helps to reduce backgrounds
- same event == 1: single track candidate in one event
- $1.2 \leq |\eta| \leq 2.4$: Pseudorapidity of the muon track falls within forward arm acceptance
- $|z| < 10$ cm : FVTX determined vertex position is within 10 cm from $z=0$ for better FVTX coverage

5.2 Distance of closest approach (DCA) Method

Among several methods which were studied to extract the Drell-Yan signal fraction, the distance of closest approach (DCA) method and the total tracklet activity in the FVTX detector method were very promising. DCA as defined in Figure 5.1, measures the closest distance of approach to the vertex position after projecting the muon track back towards the vertex position. The Drell-Yan signal fraction can be measured using the DCA distributions, since the muons from Drell-Yan process are created at the primary vertex (prompt muon) whereas the muons with heavy flavors are created at a displaced vertex (decay muons). However this method requires very precise vertex location determination.

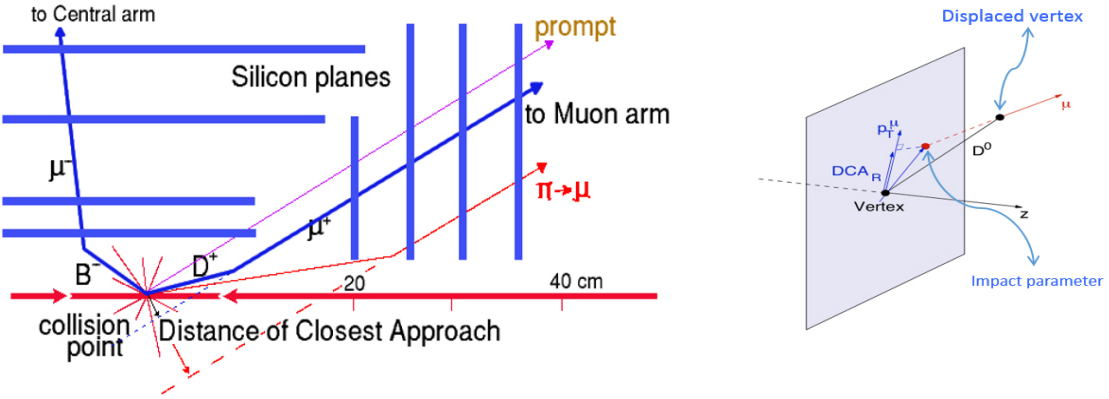


Figure 5.1: Distance of closest approach (DCA) and its projection to the transverse momentum plane (DCAr).

DCA projection to the transverse momentum plane (DCAr) is used instead of DCA since the FVTX has a better resolution in the radial direction. Simulated DCAr distributions of Drell-Yan process and heavy flavor decays are given in Figure 5.2 with a precise enough vertex determination from VTX detector.

It can be clearly seen, that the distinct DCAr widths of heavy flavor events ($\sim 300 \mu m$) from the Drell-Yan events ($\sim 100 \mu m$) can be used as a tool to estimate Drell-Yan and heavy flavor fractions in the data by using a fitting method.

But unfortunately, the VTX detector which provided an adequate resolution ($\sim 100 \mu m$) to use DCAr method was malfunctioning (only one pixel layer was functioning) in Run 13. Although many efforts were taken to recover the problem, VTX detector could not be used to measure the vertex location. Hence BBC and

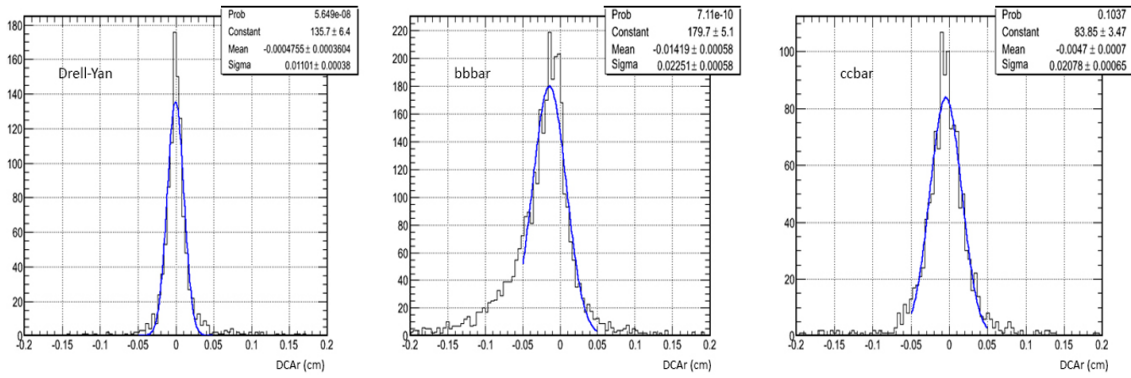


Figure 5.2: Simulated DCAr distributions for Drell-Yan, $b\bar{b}$ and $c\bar{c}$ with vertex determination from VTX detector.

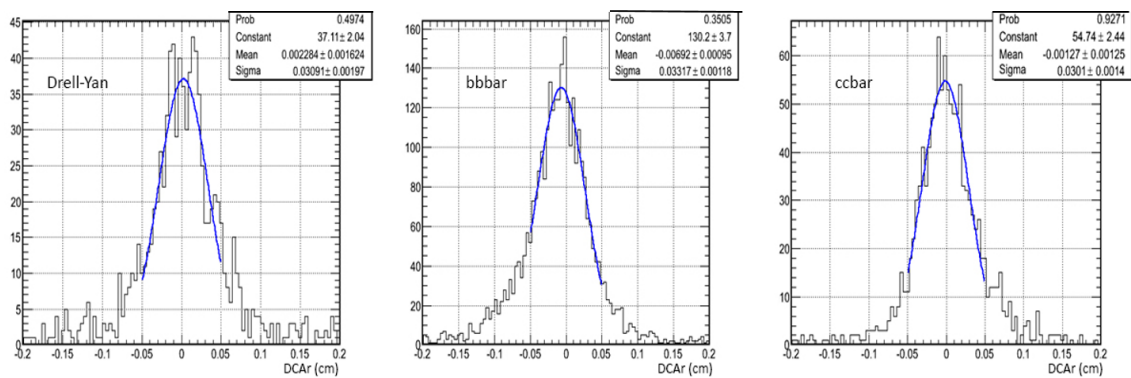


Figure 5.3: Simulated DCAr distributions for Drell-Yan, $b\bar{b}$ and $c\bar{c}$ without vertex information from VTX detector.

fvtx detectors were used to determine the vertex location but with a less resolution. As a result, DCAr could not be used to measure Drell-Yan signal fraction for Run 13 since it did not have the required differentiation power as depicted in Figure 5.3 where all processes have DCAr distribution widths of same order ($\sim 300 \mu m$).

5.3 Signal fraction from Tracklets Vs. Mass 2-D distributions

The observation of tracklet activity in the FVTX detector is the new technique introduced to overcome the challenges in the process of extracting the signal fraction. Tracklet activity in the FVTX detector is discussed in detail in Section 3.5. As can be seen in Figure 5.4, the tracklet distribution for Drell-Yan events is clearly different from the heavy flavor decays.

However, in order to get the most reliable signal to background ratio, both the tracklet activity and the invariant mass distributions were used together. The procedure to measure the signal fraction can be described in few steps as follows.

1. Draw number of tracklets vs. invariant mass 2-D distributions for the simulated Drell-Yan, ψ' and heavy flavor samples.
2. Determine the appropriate template functions to match the 2-D distributions
3. Fit the template functions to the 2-D distributions and obtain the function

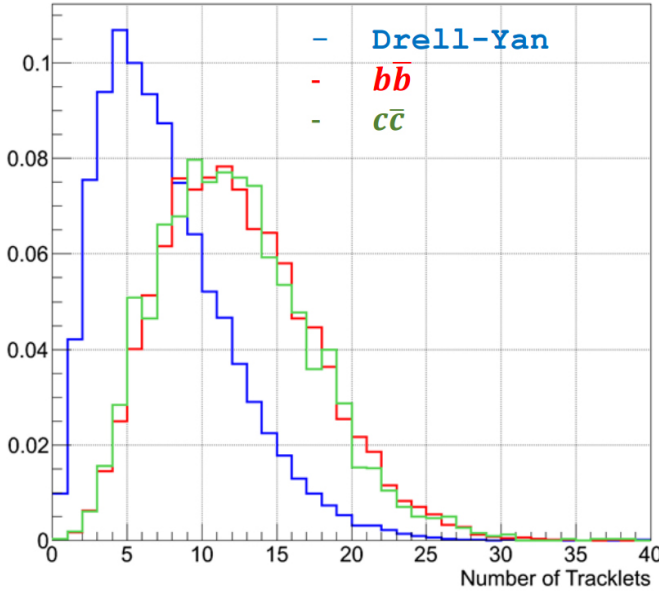


Figure 5.4: Simulated tracklet distributions for Drell-Yan, $b\bar{b}$ and $c\bar{c}$.

parameters and finalize the template functions.

4. Draw the similar 2-D distributions for the three sets of real data which were discussed in Section 4.2. For unlike-sign data we restricted our mass range from 4.5 GeV to 8.0 GeV, as the J/ψ and ψ' contamination were high in the 4.0 GeV to 4.5 GeV region.
5. Fit the three sets of real data with template functions simultaneously .
6. Determine the signal fraction.

5.3.1 Template functions

As mentioned in step 1, number of tracklets vs. invariant mass 2-D distributions were drawn for the simulated Drell-Yan, ψ' and heavy flavor samples. After carefully observing the 2-D shapes, following functions were assumed to be their functional forms.

$$f_{DY}(m, n) = \exp(A_{DY}m + B_{DY}m^2) \left(\frac{C_{DY} + D_{DY}m}{E_{DY} + F_{DY}m} \right)^{n/(E_{DY} + F_{DY}m)} \\ \times \frac{\exp[-(C_{DY} + D_{DY})/(E_{DY} + F_{DY}m)]}{\Gamma[n/(E_{DY} + F_{DY}m) + 1]} \\ \times (G_{DY} + H_{DY}n + I_{DY}n^2) \quad (5.1)$$

$$f_{b\bar{b}}(m, n) = \exp(A_{b\bar{b}}m + B_{b\bar{b}}m^2) \left(\frac{C_{b\bar{b}}}{D_{b\bar{b}}} \right)^{n/D_{b\bar{b}}} \\ \times \frac{\exp(-(C_{b\bar{b}}/D_{b\bar{b}}))}{\Gamma((n/D_{b\bar{b}}) + 1)} (E_{b\bar{b}} + F_{b\bar{b}}n) \quad (5.2)$$

$$f_{c\bar{c}}(m, n) = \exp(A_{c\bar{c}}m + B_{c\bar{c}}m^2) \left(\frac{C_{c\bar{c}}}{D_{c\bar{c}}} \right)^{n/D_{c\bar{c}}} \\ \times \frac{\exp(-(C_{c\bar{c}}/D_{c\bar{c}}))}{\Gamma((n/D_{c\bar{c}}) + 1)} (E_{c\bar{c}} + F_{c\bar{c}}n) \quad (5.3)$$

$$f_{\psi'}(m, n) = \exp(A_{\psi'}m + B_{\psi'}m^2) \left(\frac{C_{\psi'}}{D_{\psi'}} \right)^{n/D_{\psi'}} \\ \times \frac{\exp(-(C_{\psi'}/D_{\psi'}))}{\Gamma((n/D_{\psi'}) + 1)} (E_{\psi'} + F_{\psi'}n) \quad (5.4)$$

where m is the invariant mass of the dimuon pair and n is the number of tracklets.

Then the A, B, C, D, E, F, G, H and I values for each process were determined by fitting the functions to the 2-D histograms using the maximum likelihood fitting method. Since the geometrical parameters of south arm are different from north arm parameters, the analysis was done separately for two arms. The 2-D histograms of Drell-Yan, ψ' and heavy flavors with the fitted functions for north arm and south arm are shown in Figure 5.5 and Figure 5.6 respectively.

Since it is hard to see how well the fitting functions match with the simulation data distributions in Figure 5.5 and Figure 5.6, the projections of data and fitting function to mass and tracklet axis were drawn. The projection to mass axis are shown in Figure 5.7 and Figure 5.8 while the projection to tracklets axis are shown in Figure 5.9 and Figure 5.10. As can be seen in Figures 5.7, 5.8, 5.9 and 5.10, mass and tracklet distributions match with the functional forms very well. The ψ' distributions were also tested to have the correct functional forms.

The constant coefficients of template functions obtained from likelihood fitting are shown in Table 5.1 and Table 5.2. These coefficients are assumed to be fixed constants for the rest of the analysis.

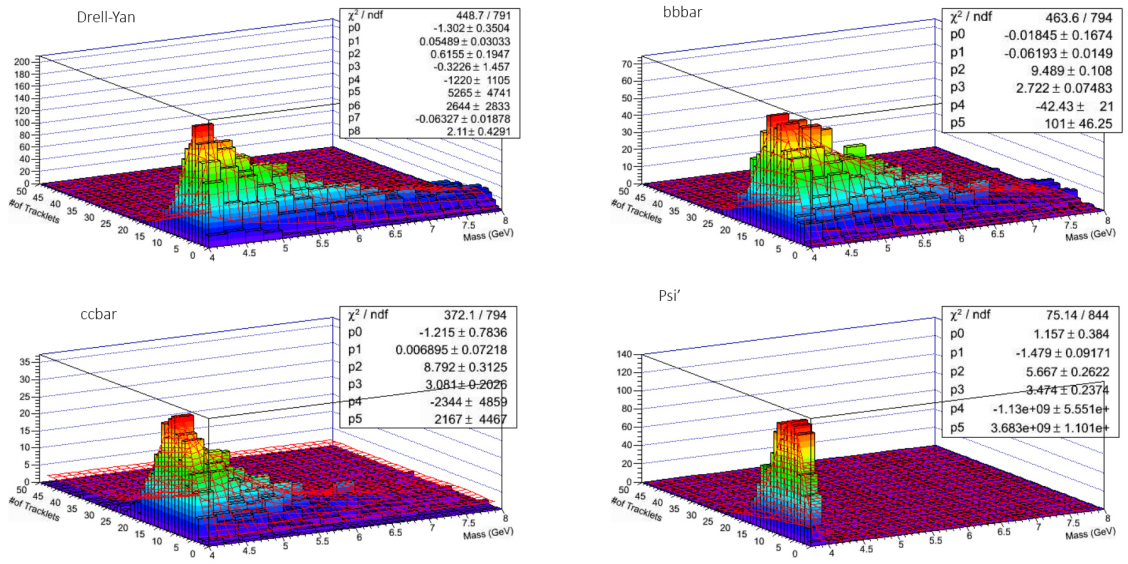


Figure 5.5: Tracklets Vs. Mass, 2-D distributions with fitted template functions for Drell-Yan, $b\bar{b}$, $c\bar{c}$ and ψ' simulations for north arm.

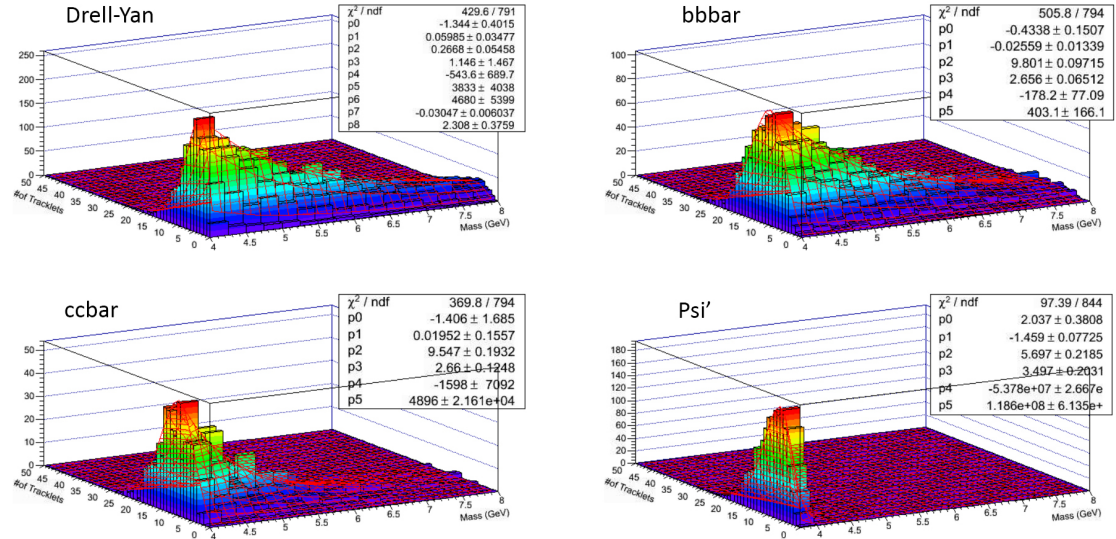


Figure 5.6: Tracklets Vs. Mass, 2-D distributions with fitted template functions for Drell-Yan, $b\bar{b}$, $c\bar{c}$ and ψ' simulations for south arm.

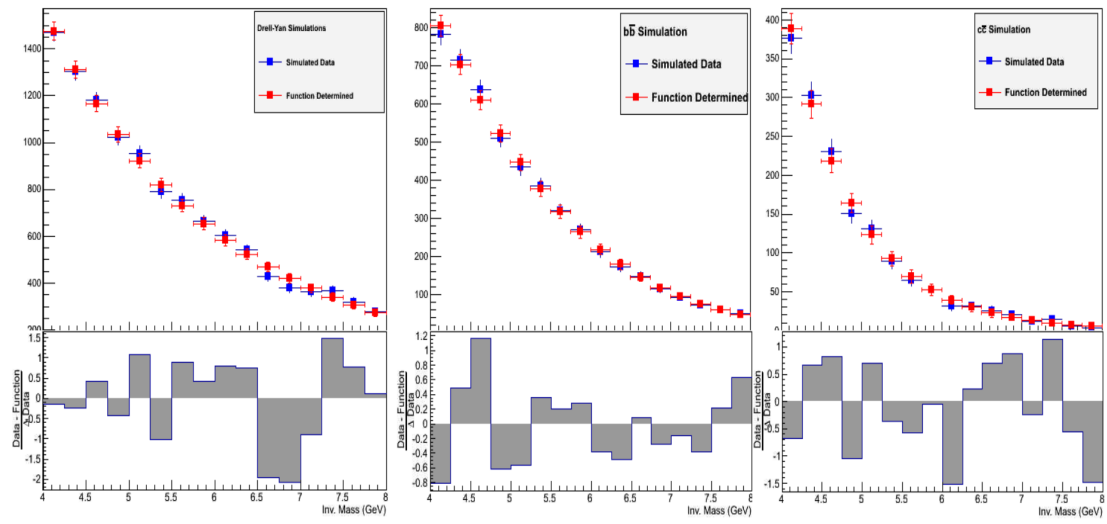


Figure 5.7: 2-D histogram projections to mass axis for north arm simulations (for tracklets vs. mass case).

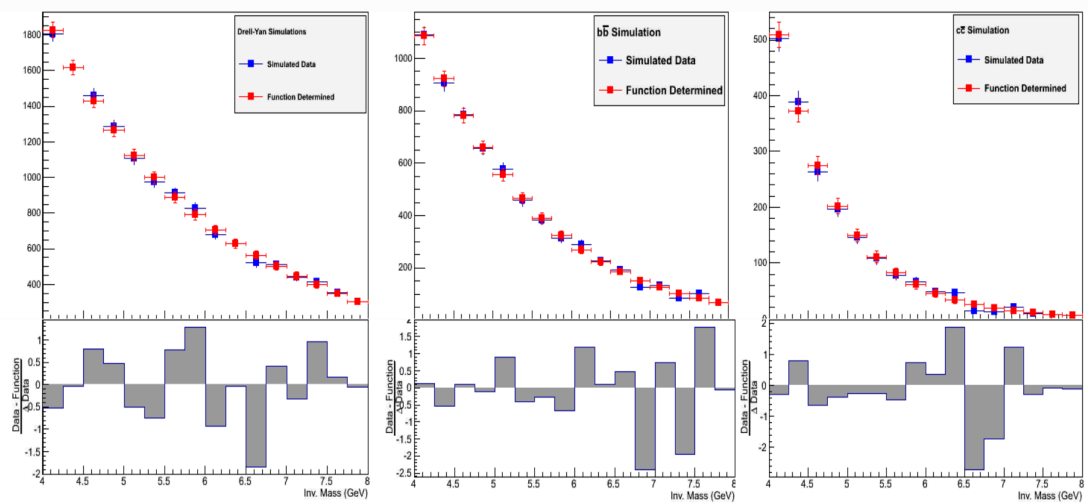


Figure 5.8: 2-D histogram projections to mass axis for south arm simulations (for tracklets vs. mass case).

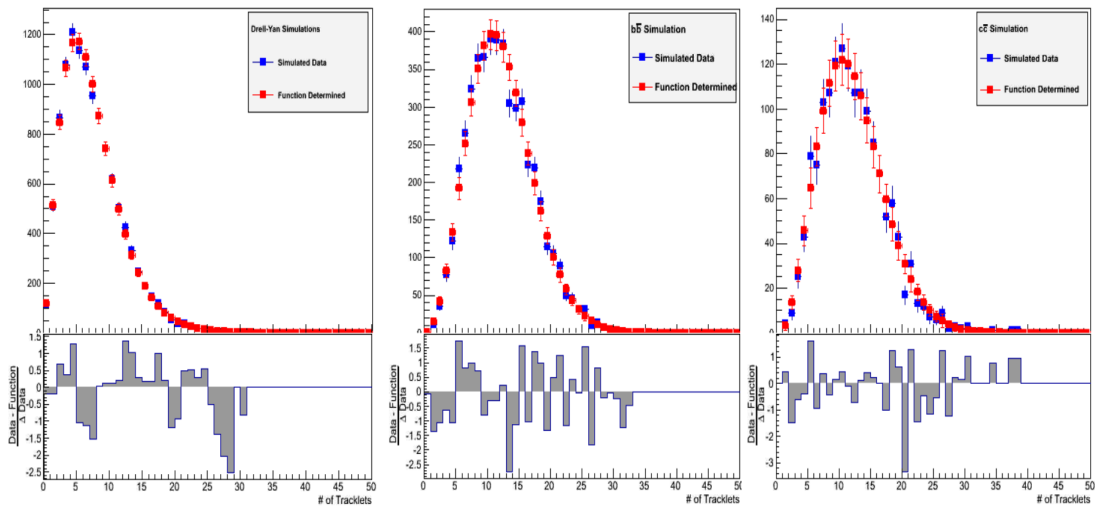


Figure 5.9: 2-D histogram projections to tracklet axis for north arm simulations (for tracklets vs. mass case).

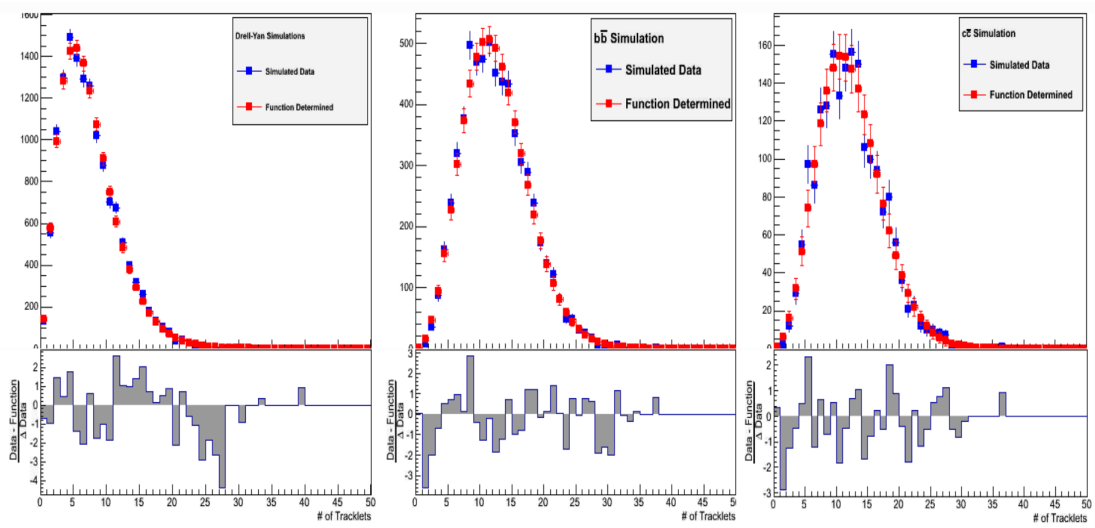


Figure 5.10: 2-D histogram projections to tracklet axis for south arm simulations (for tracklets vs. mass case).

Table 5.1: Constant coefficients of template functions determined from likelihood fitting for north arm (for tracklets vs. mass case).

Coefficient	Drell-Yan	bb	$c\bar{c}$	ψ'
A	-1.30231	-1.84518×10^{-2}	-1.21470	1.15654
B	5.48890×10^{-2}	-6.19272×10^{-2}	6.89455×10^{-3}	-1.47943
C	6.15495×10^{-1}	9.48913	8.79197	5.66740
D	-3.22599×10^{-1}	2.72228	3.08102	3.47383
E	-1.22041×10^3	-4.24254×10^1	-2.34365×10^3	-1.13019×10^9
F	5.26518×10^3	1.00984×10^2	2.16680×10^3	3.68337×10^9
G	2.64442×10^3			
H	-6.32659×10^{-2}			
I	2.10978			

Table 5.2: Constant coefficients of template functions determined from likelihood fitting for south arm (for tracklets vs. mass case).

Coefficient	Drell-Yan	bb	$c\bar{c}$	ψ'
A	-1.34388	-4.33761×10^{-1}	-1.40639	2.0368
B	5.98491×10^{-2}	-2.55920×10^{-2}	1.95232×10^{-2}	-1.45908
C	2.66763×10^{-1}	9.80109	9.54739	5.6966
D	1.14564	2.65613	2.66032	3.49692
E	-5.43638×10^2	-1.78231×10^2	-1.59751×10^3	-5.37760×10^7
F	3.83264×10^3	4.03103×10^2	4.89592×10^3	1.18560×10^8
G	4.67991×10^3			
H	-3.04739×10^{-2}			
I	2.30778			

5.3.2 Template fitting

After confirming the final template functions which represent the signal and background 2-D distribution shapes, the three sets of data were fitted simultaneously with the template functions according to the following equations. The maximum likelihood method was used as the fitting method.

$$f_{Final}^{+-}(m, n) = A \cdot f_{DY} + B \cdot f_{b\bar{b}} + C \cdot f_{c\bar{c}} + 2 \cdot \sqrt{D * E} \cdot f_{comb} \quad (5.5)$$

$$f_{Final}^{++}(m, n) = B' \cdot f_{b\bar{b}} + D \cdot f_{comb} \quad \text{where } (B' = 0.26 * B) \quad (5.6)$$

$$f_{Final}^{--}(m, n) = B'' \cdot f_{b\bar{b}} + E \cdot f_{comb} \quad \text{where } (B'' = 0.26 * B) \quad (5.7)$$

Where f_{comb} is the combinatorial background shape which was assumed to be the functional form given in Equation 5.8.

$$f_{comb}(m, n) = \exp(A_{comb}m + B_{comb}m^2) \cdot \text{Poisson}(n, C_{comb}) \quad (5.8)$$

A, B, C, D, E, A_{comb} , B_{comb} and C_{comb} were kept as free parameters and they were determined from the template fitting. Some of the assumptions made while deriving these formula are,

1. The template functions represent the actual shapes of signal and each background distributions. This assumption is made based on the agreement of Run 13 J/ψ data with the J/ψ simulations as showed in Section 3.5.

2. The $b\bar{b}$ 2-D shapes of the like-sign data were assumed to be similar to $b\bar{b}$ shape of unlike-sign data. (The simulated $b\bar{b}$ 2-D shapes for the like-sign cases agreed with $b\bar{b}$ template for unlike-sign case.)
3. Combinatorial background in unlike-sign data is assumed to be $2\cdot\sqrt{N_{++}\cdot N_{--}}$. (N_{++} is chosen to be proportional to coefficient D whereas N_{--} is assumed to be proportional to coefficient E) This assumption was made using the following hypothesizes
 - Muons from pair are not physically corelated.
 - No correlation between meson + and - multiplicities
 - Multiplicities follow a Poisson distribution

For this fitting, a special technique was used in root programming language. First the three sets of data were plotted into a single histogram for each arm as shown in Figure 5.11 and Figure 5.12. The X axis was divided into three regions as

- 4.5 to 8 = Mass 4.5 to 8 for unlike-sign sign
- 8 to 12 = Mass 4 to 8 for like-sign ++
- 12 to 16 = Mass 4 to 8 for like-sign --

and the Y axis was divided into three regions as

- 0 to 50 = Tracklet 0 to 50 for unlike-sign sign
- 50 to 100 = Tracklet 0 to 50 for like-sign ++
- 100 to 150 = Tracklet 0 to 50 for like-sign --

Then the template functions were fitted simultaneously for the three sets of data which were plotted into a single histogram. Since it is hard to see the matching of the fitting to the data from the 2-D plot, the projections to mass and tracklet axis and the decomposition of the yield to each process were drawn as shown in Figure 5.13 and Figure 5.14. It can be seen that the fitted functions agree well with the three sets of the data.

The A, B, C, D, E, A_{comb} , B_{comb} and C_{comb} coefficients were found from the fitting. Then these coefficients were used to measure the number of events from Drell-Yan and other background processes. The measured numbers of each type of process are given in Table 5.3.

As an example the number of Drell-Yan events (N_{DY}) was measured as :

$$N_{DY} = A \int_{n=0}^{50} \int_{m=4.5}^{8.0} f_{DY}(m, n) dm dn \quad (5.9)$$

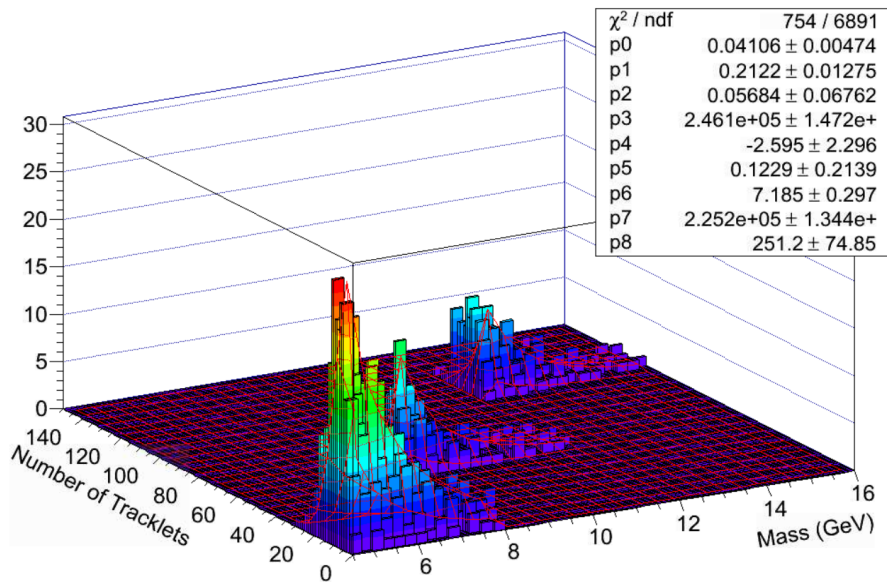


Figure 5.11: North arm template fitting (for tracklets vs. mass case).

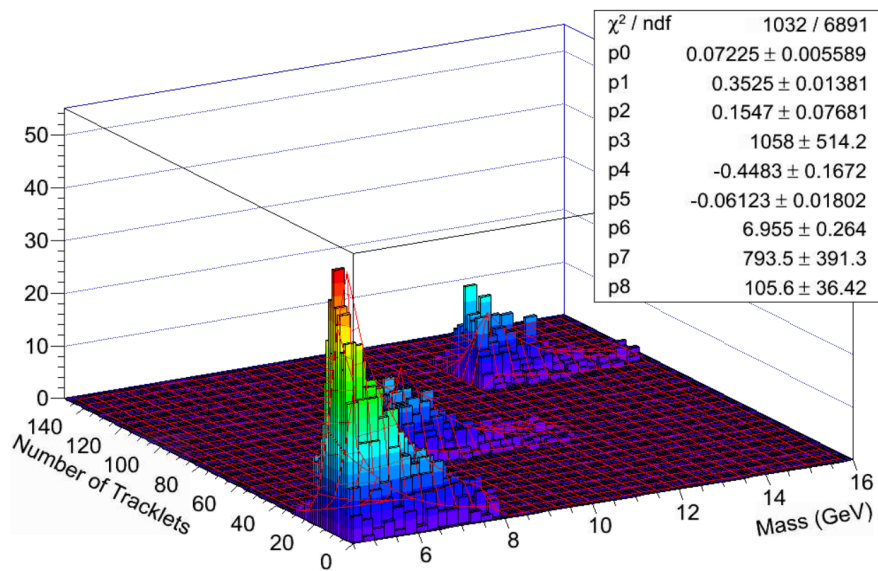


Figure 5.12: South arm template fitting (for tracklets vs. mass case).

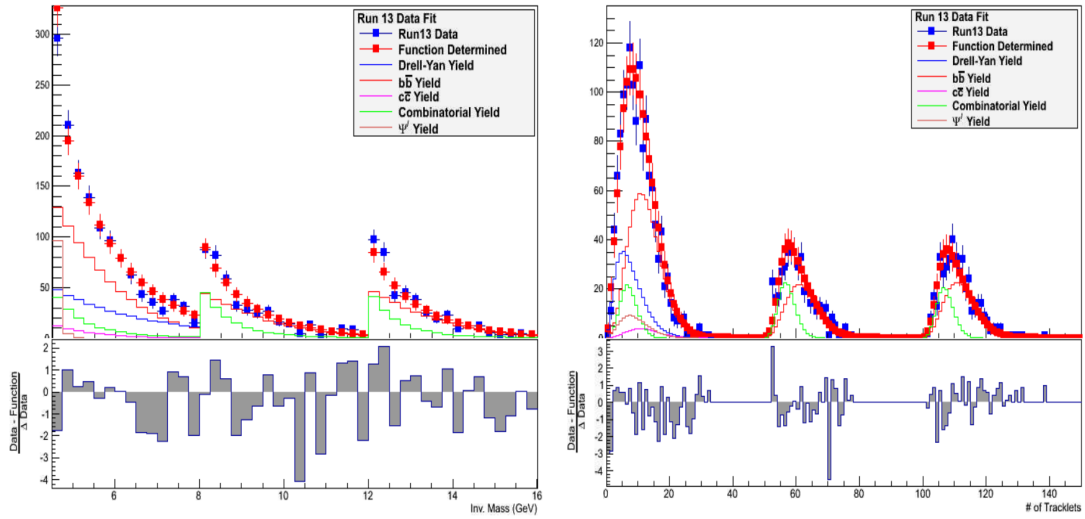


Figure 5.13: Template fitted final histogram projections to mass axis and tracklets axis for north arm.

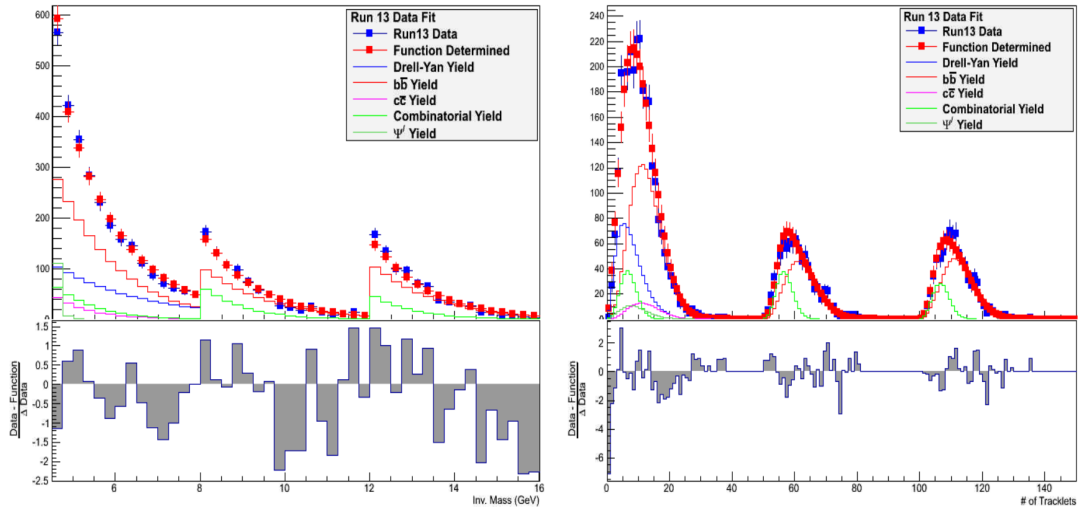


Figure 5.14: Template fitted final histogram projections to mass axis and tracklets axis for south arm.

Table 5.3: Number of signal events and each background events obtained from the tracklets vs. mass template fitting.

Arm	Process	Number of events (\pm) Stat. Error
North	Drell-Yan	354 ± 41
North	$b\bar{b}$	738 ± 44
North	$c\bar{c}$	49 ± 58
North	ψ'	100 ± 30
North	Combinatorial	145 ± 20
South	Drell-Yan	751 ± 68
South	$b\bar{b}$	1544 ± 61
South	$c\bar{c}$	161 ± 80
South	ψ'	116 ± 40
South	Combinatorial	253 ± 25

5.3.3 Monte Carlo test results

Monte Carlo test (also known as pull test) was done in order to test how well the fitting method can extract the spectrum shapes that are found in this analysis.

The procedure followed for Monte Carlo test is described as follows:

1. Calculate the each bin content from the final fitting function.
2. Generate a random number for each bin from a Poisson distribution with the mean value as the calculated bin content.
3. Plot the new 2-D plot with the generated numbers.
4. Fit the 2-D plot with the final function with likelihood method and determine the coefficients.
5. Then iterate this procedure 1400 times.
6. Get the coefficients which correspond to each type of process for each iteration and fill them into histograms.
7. Fit with a Gaussian distributions to the histograms.
8. Compare the mean values and the standard deviations of the Gaussian fittings to number of signal and background events and their uncertainties.

The Monte Carlo test results for North and South arms are shown in Figures 5.15 and 5.16. The mean and the error values of the Gaussian fitting agrees with

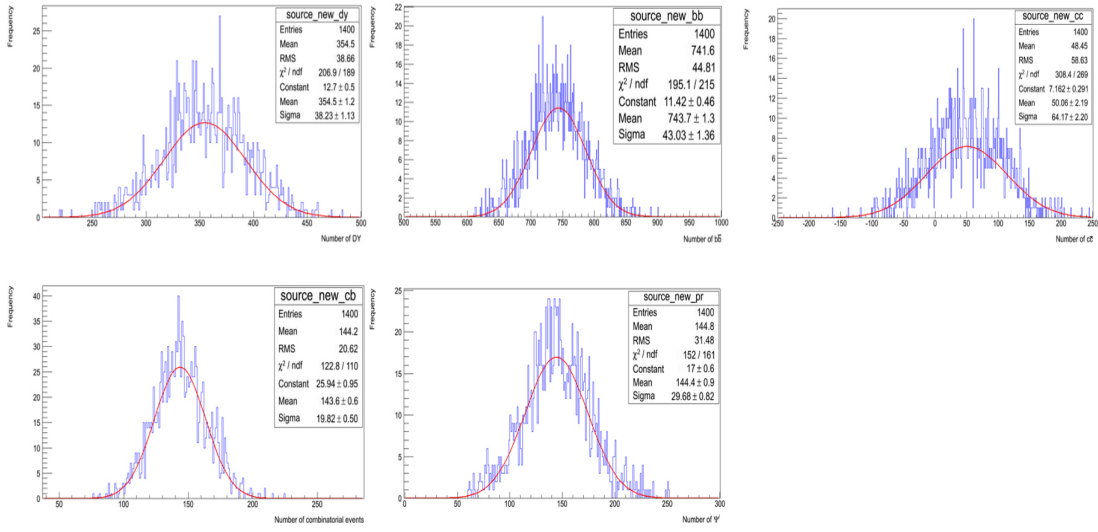


Figure 5.15: The number of events for each process determined from Monte Carlo test for north arm.

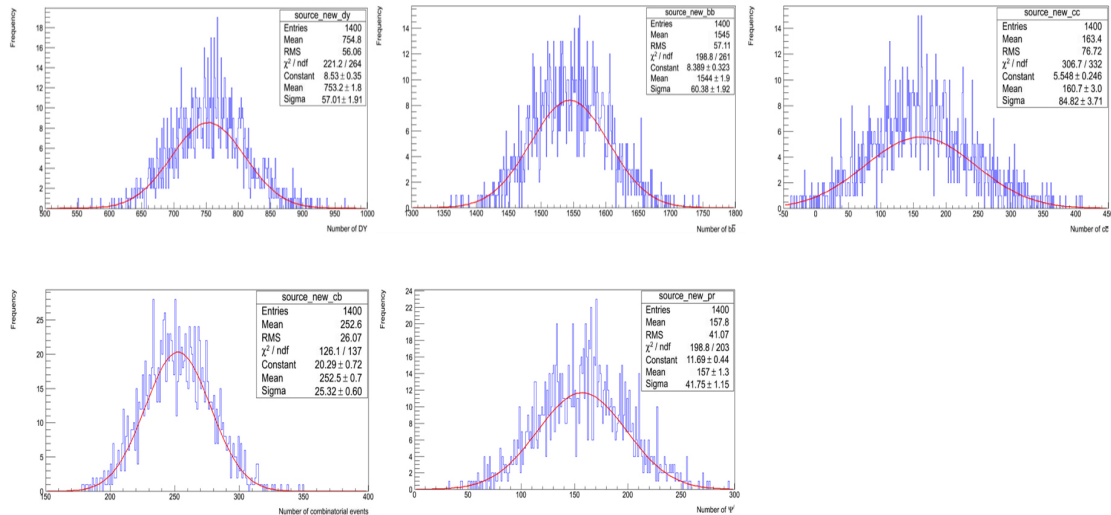


Figure 5.16: The number of events for each process determined from Monte Carlo test for south arm.

the final fitting for the data which indicates that the fitting method properly estimate the statistical uncertainties. Further the backgrounds and signal were mixed in different ratios and tested the template fitting. The two dimensional likelihood method was able to correctly identify the correct ratios between signal and background.

The coefficient for Drell-Yan vs. coefficient for $b\bar{b}$ was plotted to see whether there is any correlations between them. As can be seen in Figure 5.17, no strong correlation was seen between them. And also no strong correlations were observed between Drell-Yan and other backgrounds. But as expected, a strong co-relation was observed between $b\bar{b}$ and $c\bar{c}$ coefficients as shown in Figure 5.17.

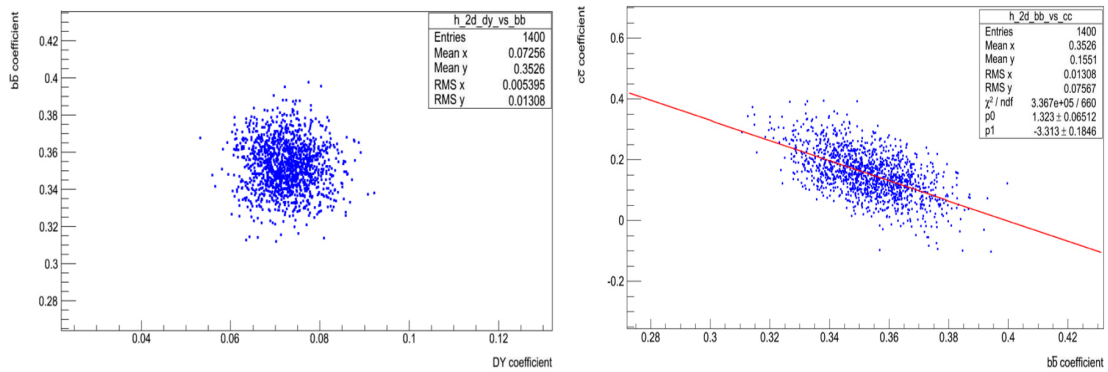


Figure 5.17: 2-D distributions of coefficient of Drell-Yan vs. coefficient of $b\bar{b}$ and coefficient of $c\bar{c}$ vs. coefficient of $b\bar{b}$ obtained from Monte Carlo test fittings.

5.4 Tracklets Vs. Transverse Momentum 2-D template functions

As a measure of the systematic uncertainty to the signal fraction and as a cross check, similar procedure to the tracklets vs. mass was carried out with the tracklets vs. transverse momentum (p_T) 2-D distributions.

5.4.1 Template functions

The template functions of number of tracklets vs. transverse momentum 2-D distributions for the simulated Drell-Yan, ψ' and heavy flavor samples were assumed to have following functional forms.

$$f_{DY}(p, n) = \left(\frac{A_{DY}}{B_{DY}} \right)^{p/B_{DY}} \cdot \frac{\exp(-(A_{DY}/B_{DY}))}{\Gamma((p/B_{DY}) + 1)} * (G_{DY} + H_{DYP}p + I_{DYP^2} + J_{DYP^3}) \\ \times \left(\frac{C_{DY}}{D_{DY}} \right)^{n/D_{DY}} \cdot \frac{\exp(-(C_{DY}/D_{DY}))}{\Gamma((n/D_{DY}) + 1)} \cdot (E_{DY} + F_{DY}n) \quad (5.10)$$

$$f_{b\bar{b}}(p, n) = \left(\frac{A_{b\bar{b}}}{B_{b\bar{b}}} \right)^{p/B_{b\bar{b}}} \cdot \frac{\exp(-(A_{b\bar{b}}/B_{b\bar{b}}))}{\Gamma((p/B_{b\bar{b}}) + 1)} * (G_{b\bar{b}} + H_{b\bar{b}}p) \\ \times \left(\frac{C_{b\bar{b}}}{D_{b\bar{b}}} \right)^{n/D_{b\bar{b}}} \cdot \frac{\exp(-(C_{b\bar{b}}/D_{b\bar{b}}))}{\Gamma((n/D_{b\bar{b}}) + 1)} \cdot (E_{b\bar{b}} + F_{b\bar{b}}n) \quad (5.11)$$

$$f_{c\bar{c}}(p, n) = \left(\frac{A_{c\bar{c}}}{B_{c\bar{c}}} \right)^{p/B_{c\bar{c}}} \cdot \frac{\exp(-(A_{c\bar{c}}/B_{c\bar{c}}))}{\Gamma((p/B_{c\bar{c}}) + 1)} * (G_{c\bar{c}} + H_{c\bar{c}}p) \\ \times \left(\frac{C_{c\bar{c}}}{D_{c\bar{c}}} \right)^{n/D_{c\bar{c}}} \cdot \frac{\exp(-(C_{c\bar{c}}/D_{c\bar{c}}))}{\Gamma((n/D_{c\bar{c}}) + 1)} \cdot (E_{c\bar{c}} + F_{c\bar{c}}n) \quad (5.12)$$

$$f_{\psi'}(p, n) = \left(\frac{A_{\psi'}}{B_{\psi'}}\right)^{p/B_{\psi'}} \cdot \frac{\exp(-(A_{\psi'}/B_{\psi'}))}{\Gamma((p/B_{\psi'}) + 1)} * (G_{\psi'} + H_{\psi'}p) \\ \times \left(\frac{C_{\psi'}}{D_{\psi'}}\right)^{n/D_{\psi'}} \cdot \frac{\exp(-(C_{\psi'}/D_{\psi'}))}{\Gamma((n/D_{\psi'}) + 1)} \cdot (E_{\psi'} + F_{\psi'}n) \quad (5.13)$$

where p is the transverse momentum of the dimuon pair and n is the number of tracklets.

Similarly to the tracklet vs. mass case, the A, B, C, D, E, F, G, H, I, J values for each process were determined by fitting the functions to the 2-D histograms using the maximum likelihood fitting method. The 2-D histograms of Drell-Yan, ψ' and heavy flavors with the fitted functions for north arm and south arm are shown in Figure 5.18 and Figure 5.19 respectively. The projections of data and fitting function to pT axis are drawn in Figure 5.20 and Figure 5.21 and the projection to tracklets axis are drawn in Figure 5.22 and Figure 5.23. As can be seen in Figures 5.20, 5.21, 5.22 and 5.23, pT and tracklet distributions agree with the functional forms very well. The ψ' distributions were also tested to have the correct functional forms.

The constant coefficients of template functions obtained from likelihood fitting are shown in Table 5.4 and Table 5.5. Similarly to tracklet vs mass case, these coefficients were kept fixed for the rest of the analysis.

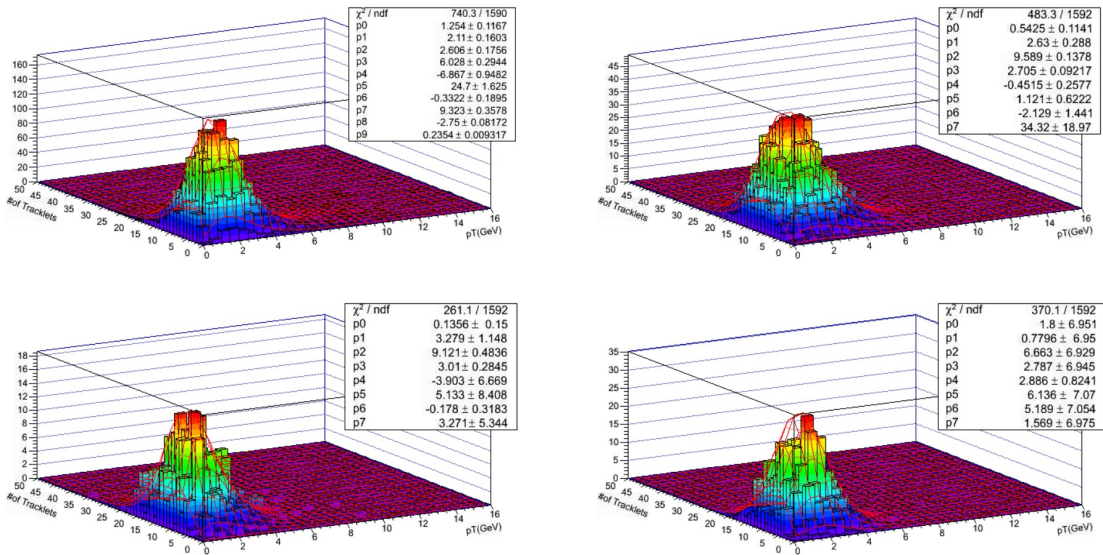


Figure 5.18: Tracklets Vs. pT, 2-D distributions with fitted template functions for Drell-Yan, $b\bar{b}$, $c\bar{c}$ and ψ' simulations for north arm.

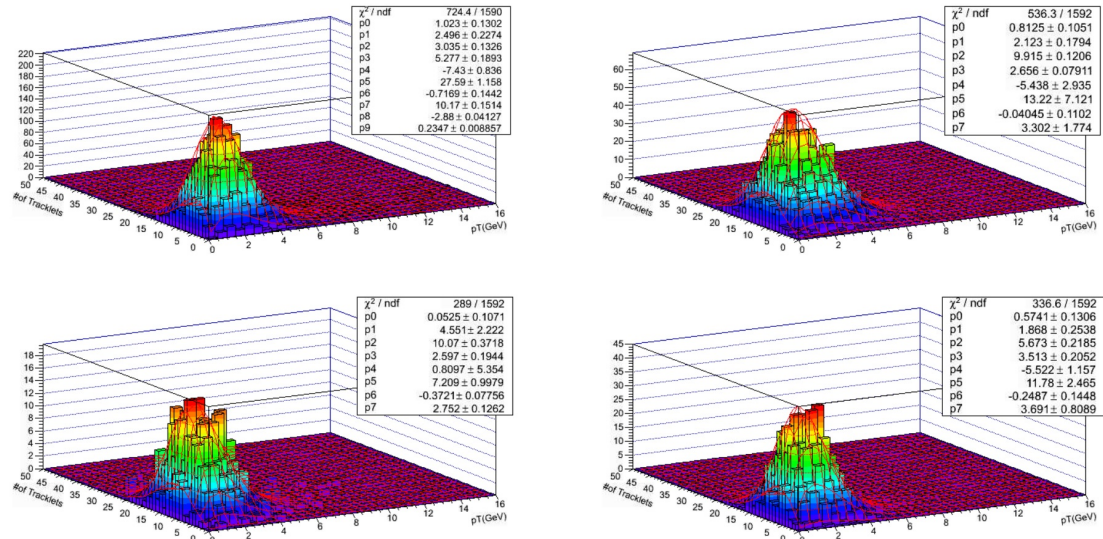


Figure 5.19: Tracklets Vs. pT, 2-D distributions with fitted template functions for Drell-Yan, $b\bar{b}$, $c\bar{c}$ and ψ' simulations for south arm.

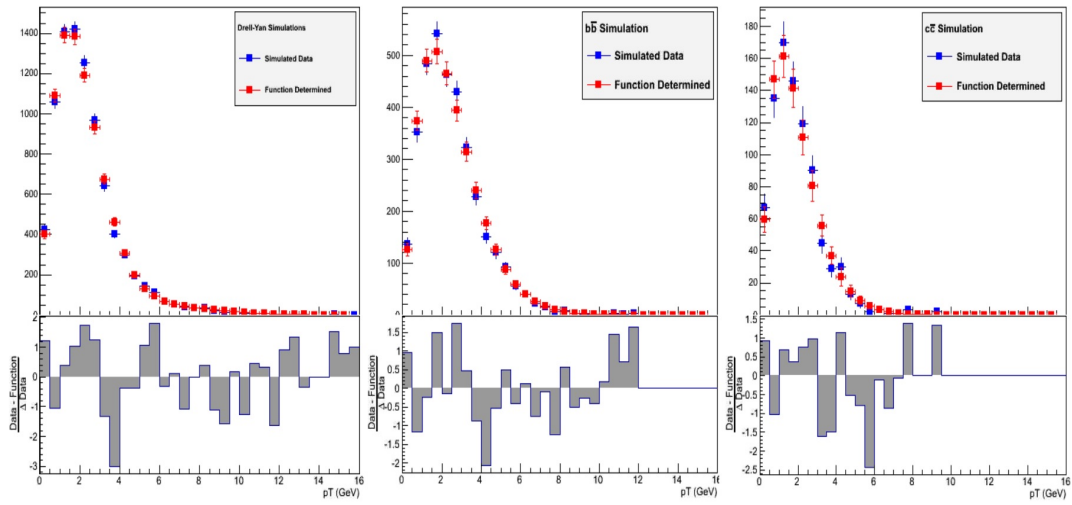


Figure 5.20: 2-D histogram projections to p_T axis for north arm simulations (for tracklet vs. p_T case).

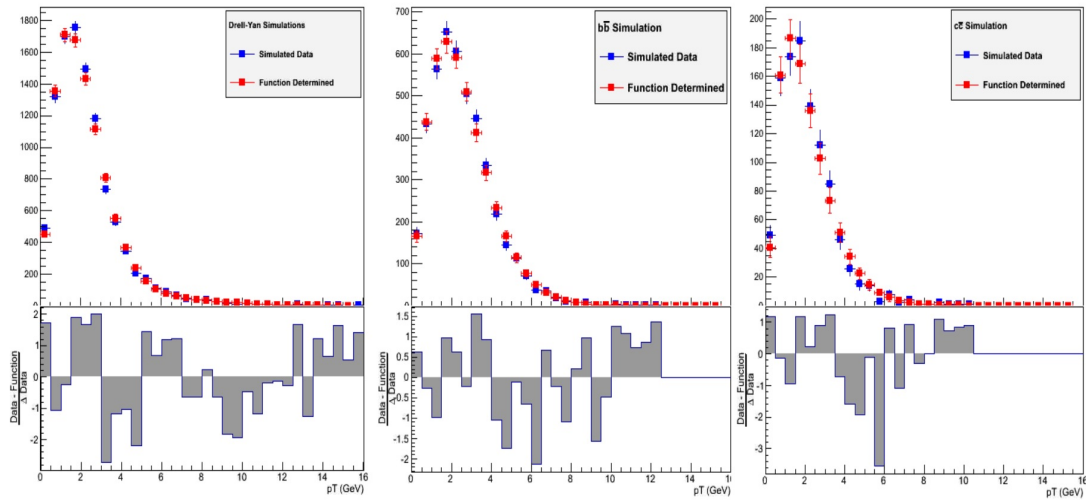


Figure 5.21: 2-D histogram projections to p_T axis for south arm simulations (for tracklet vs. p_T case).

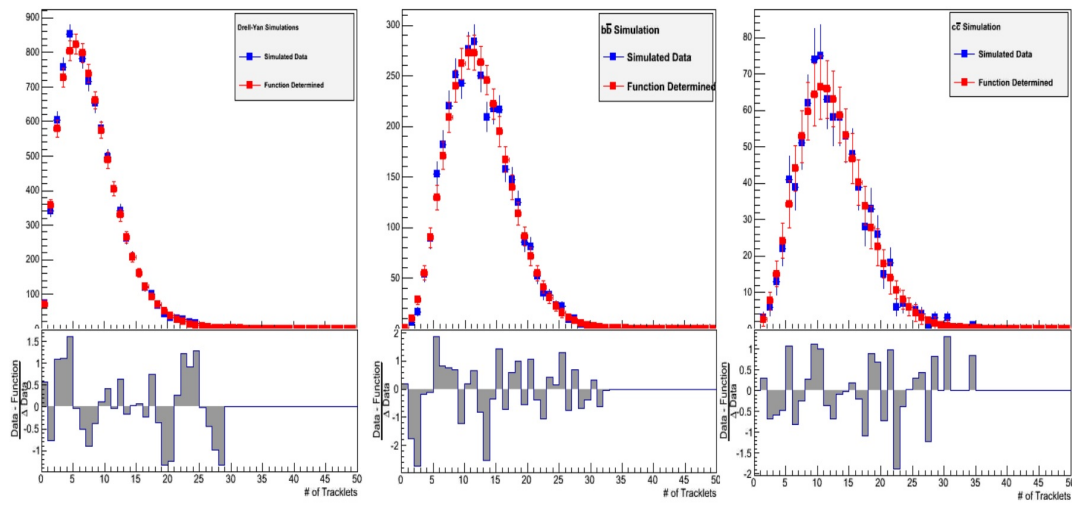


Figure 5.22: 2-D histogram projections to tracklets axis for north arm simulations (for tracklet vs. pT case).

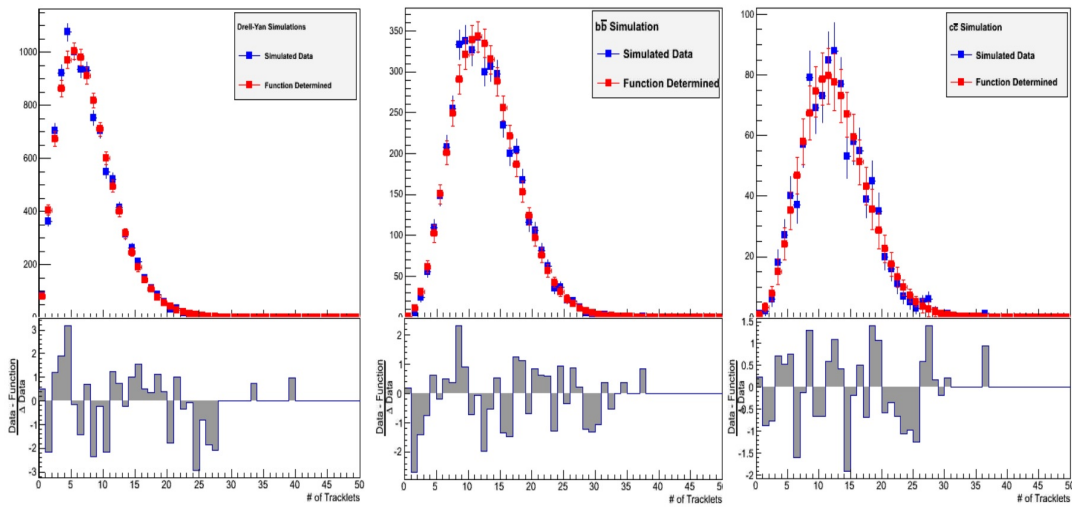


Figure 5.23: 2-D histogram projections to tracklets axis for south arm simulations (for tracklet vs. pT case).

Table 5.4: Constant coefficients of template functions determined from likelihood fitting for north arm (for tracklets vs. pT case).

Coefficient	Drell-Yan	$b\bar{b}$	$c\bar{c}$	ψ'
A	1.25444	5.42465×10^{-1}	1.35557×10^{-1}	1.79965
B	2.11016	2.63032	3.27890	7.79552×10^{-1}
C	2.60569	9.58856	9.12118	6.66331
D	6.02841	2.70545	3.01008	2.78745
E	-6.86702	-4.51529×10^{-1}	-3.90258	2.88563
F	2.47001×10^1	1.12148	5.13332	6.13620
G	-3.32205×10^{-1}	-2.12887	-1.77985×10^{-1}	5.18944
H	9.32313	3.43214×10^1	3.27127	1.56900
I	-2.75027			
J	2.35411×10^{-1}			

Table 5.5: Constant coefficients of template functions determined from likelihood fitting for south arm (for tracklets vs. pT case).

Coefficient	Drell-Yan	$b\bar{b}$	$c\bar{c}$	ψ'
A	1.02349	8.12519×10^{-1}	5.25022×10^{-2}	5.74089×10^{-1}
B	2.49557	2.12333	4.55086	1.86765
C	3.03453	9.91547	1.00684×10^1	5.67252
D	5.27734	2.65629	2.59729	3.51315
E	-7.42975	-5.43819	8.09703×10^{-1}	-5.52186
F	2.75866×10^1	1.32249×10^1	7.20927	1.17809×10^1
G	-7.16948×10^{-1}	-4.04502×10^{-2}	-3.72125×10^{-1}	-2.48654×10^{-1}
H	1.01746×10^1	3.30167	2.75174	3.69123
I	-2.87955			
J	2.34746×10^{-1}			

5.4.2 Template fitting

After finding the best template functions which represent the signal and background 2-D distribution shapes, the three sets of data were fitted simultaneously with the template functions according to the relationships in Equations 5.5, 5.6 and 5.7 using the maximum likelihood method. The combinatorial background shape was assumed to be the functional form given in Equation 5.14.

$$f_{comb}(p, n) = Poisson(p, A_{comb}) \cdot Poisson(n, B_{comb}) \quad (5.14)$$

A, B, C, D, E, A_{comb} and B_{comb} were kept as free parameters and they were determined from the template fitting. For this fitting, same technique was used as the tracklets vs. mass case. The X axis was divided into three regions as

- 0 to 16 = pT 0 to 16 for unlike-sign sign
- 16 to 32 = pT 0 to 16 for like-sign ++
- 32 to 48 = pT 0 to 16 for like-sign --

and the Y axis was divided into three regions as

- 0 to 50 = Tracklet 0 to 50 for unlike-sign sign
- 50 to 100 = Tracklet 0 to 50 for like-sign ++
- 100 to 150 = Tracklet 0 to 50 for like-sign --

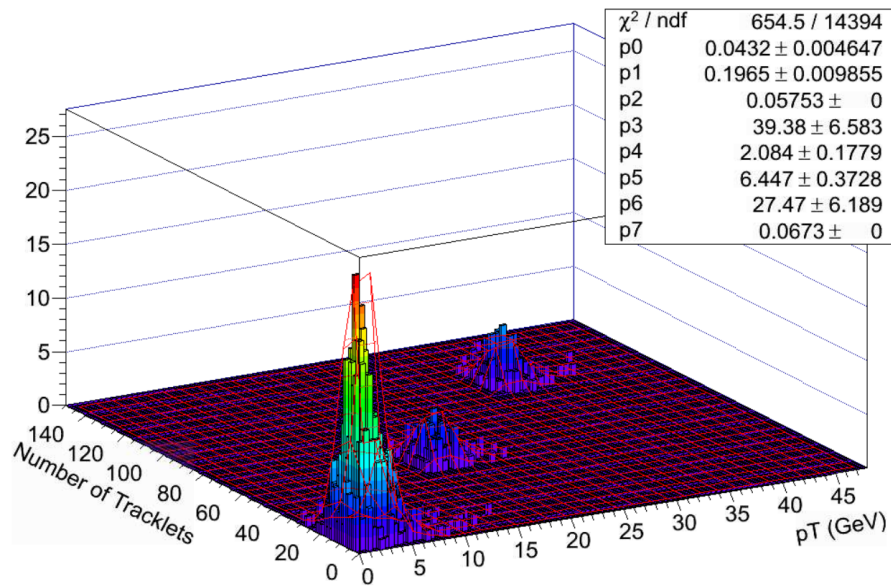


Figure 5.24: North arm template fit using tracklets vs. p_T distributions.

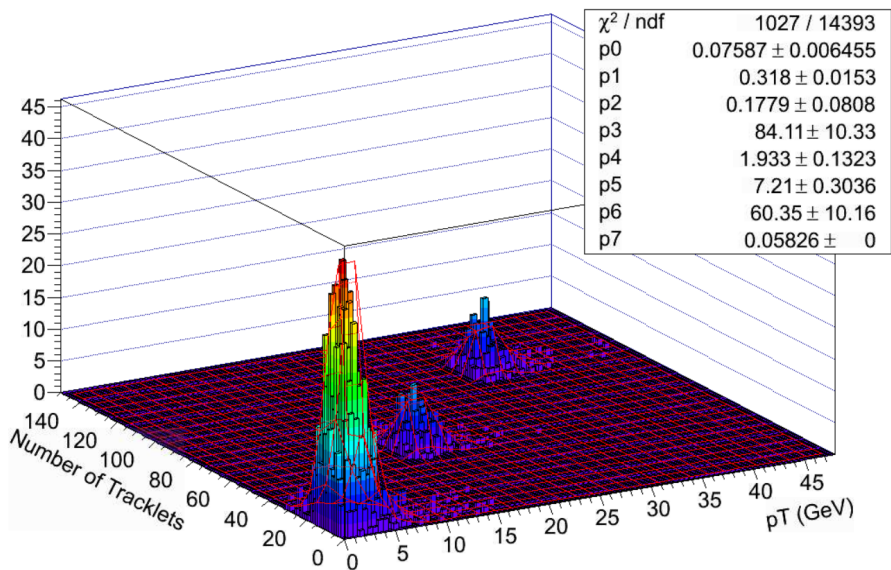


Figure 5.25: South arm template fit using tracklets vs. p_T distribution.

The three sets of data fitted with template functions are shown in Figure 5.24 and Figure 5.25. However the number of ψ' events was estimated from the mass fitting and kept constant in this fitting.

The projections to pT and tracklet axis and the decomposition of the yield to each process were drawn as shown in Figure 5.26 and Figure 5.27. It can be seen that the fitted function agrees well with the three sets of the data. The number of events determined from the tracklets vs pT fitting for each process is given in Table 5.6.

Table 5.6: Number of signal events and each background events obtained from the tracklets vs. pT fitting

Arm	Process	Number of events (\pm)Stat. Error
North	Drell-Yan	440 ± 39
	$b\bar{b}$	698 ± 34
	$c\bar{c}$	0 ± 51
	ψ'	100 ± 0 (Fixed)
	Combinatorial	113 ± 35
South	Drell-Yan	926 ± 54
	$b\bar{b}$	1414 ± 51
	$c\bar{c}$	102 ± 112
	ψ'	116 ± 0 (FIXED)
	Combinatorial	243 ± 54

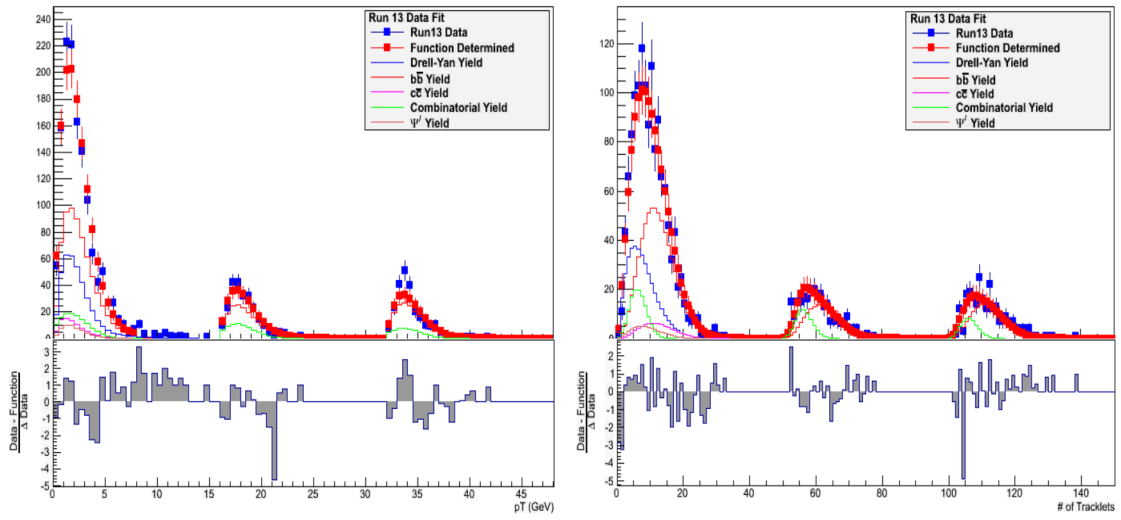


Figure 5.26: Template fitted final histogram projections to p_T axis and tracklets axis for north arm.

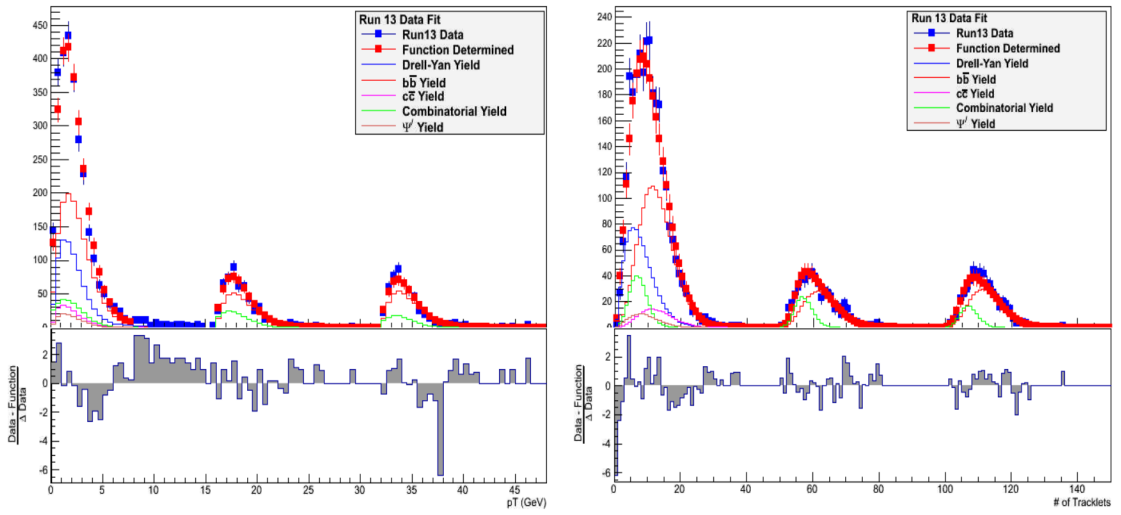


Figure 5.27: Template fitted final histogram projections to p_T axis and tracklets axis for south arm.

5.5 Drell-Yan signal fraction

The final results for the number of each type of events present in Run 13 data are given in Table 5.7.

Table 5.7: Summary of the number of events for signal and backgrounds.

Arm	Process	# of events from mass fit	# of events from pT fit	Sys. Err.
North	Drell-Yan	354 ± 41	440 ± 39	86
North	$b\bar{b}$	738 ± 44	698 ± 34	40
North	$c\bar{c}$	49 ± 58	0 ± 51	49
North	ψ'	100 ± 30	100 ± 0	0
North	Combinatorial	145 ± 20	113 ± 35	32
South	Drell-Yan	751 ± 68	926 ± 54	175
South	$b\bar{b}$	1544 ± 61	1414 ± 51	130
South	$c\bar{c}$	161 ± 80	102 ± 112	59
South	ψ'	116 ± 40	116 ± 0	0
South	Combinatorial	253 ± 87	243 ± 54	10

Results in Table 5.7 were used to measure the Drell-Yan fraction for north arm (F_{DY}^{north}) as

$$F_{DY}^{north} = 0.26 \pm 0.03(stat.) \pm 0.07(syst.) \quad (5.15)$$

and south arm (F_{DY}^{south}) as

$$F_{DY}^{south} = 0.27 \pm 0.03(stat.) \pm 0.06(syst.) \quad (5.16)$$

6 MEASUREMENT OF DRELL-YAN A_{LL}

Measurement of the Drell-Yan longitudinal double spin asymmetry (A_{LL}^{DY}) can be described in following steps. Each step is discussed in detail later in this chapter.

1. Define four tracklet bins (0–5, 5–10, 10–15 and 15–50) and two mass bins (4.5–5 GeV for unlike-sign/4–5 GeV for like-sign and 5–8 GeV). This makes 8 interested regions for each arm.
2. Determine the signal and background fractions in each region using the results from template fitting.
3. Measure the inclusive A_{LL} (Section 6.2.1) in each region for unlike-sign and like-sign dimuon pairs.
4. Remove the ψ' contribution to the inclusive asymmetries.
5. Plot the inclusive asymmetry values to a graph where x axis is heavy flavor fraction and the y axis is the combinatorial fraction.
6. Determine the physics asymmetries for signal and backgrounds from a fitting to the graph in step 5.

6.1 Signal and background fractions

Since the total number of signal events and background events are already measured as discussed in Chapter 5, the fractions of each event type in each of the 8 regions defined in step 1 can be found easily. The fractions of Drell-Yan, heavy flavors and combinatorial events are shown in Figure 6.1 and Figure 6.2. It can be clearly seen that the heavy flavor fraction increases whereas the signal and combinatorial fractions decrease with the number of tracklets. Since the Drell-Yan and background fractions depend on tracklet number differently, these distributions can be used to separate out the contributions of the Drell-Yan and background processes to the asymmetry.

As a comparison, Tracklet vs. pT distributions were also used to measure Drell-Yan A_{LL} as a separate study. Hence similar regions were defined using four tracklet bins (0–5, 5–10, 10–15 and 15–50) and two pT bins (0–2 GeV and 2–10 GeV). The dimuon mass range used was from 4.5 GeV to 8.0 GeV. Then the signal and background fractions were found for each region. As expected, it was observed that the heavy flavor fraction increases whereas the signal and combinatorial fractions decrease with the number of tracklets for each pT bin as shown in Figure 6.3 and Figure 6.4.

The systematic uncertainties in Figure 6.1 and Figure 6.2 are shown in gray color and they were estimated by scaling the systematic uncertainties found in

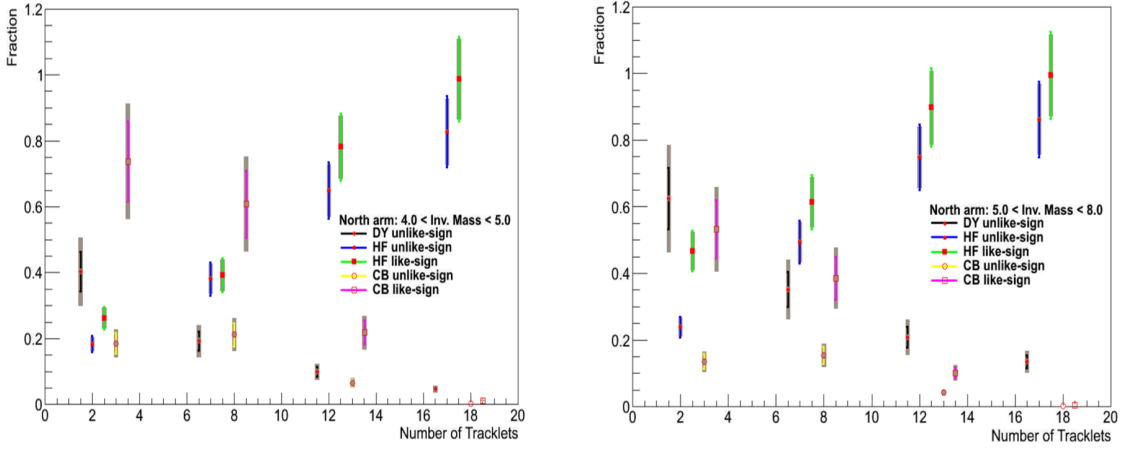


Figure 6.1: North arm signal and background fractions for four tracklet regions (0–5, 5–10, 10–15 and 15–50) for tracklets vs. mass case.

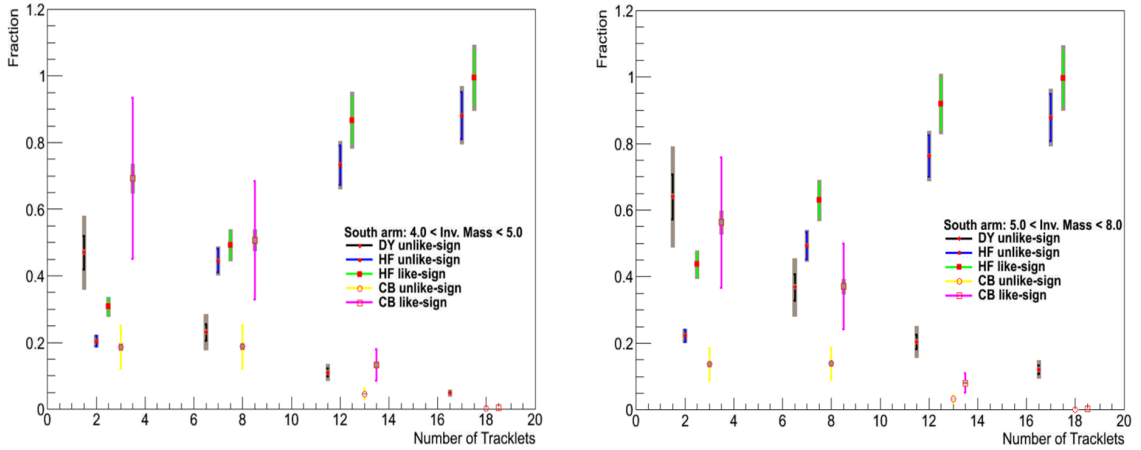


Figure 6.2: South arm signal and background fractions for four tracklet regions (0–5, 5–10, 10–15 and 15–50) for tracklets vs. mass case.

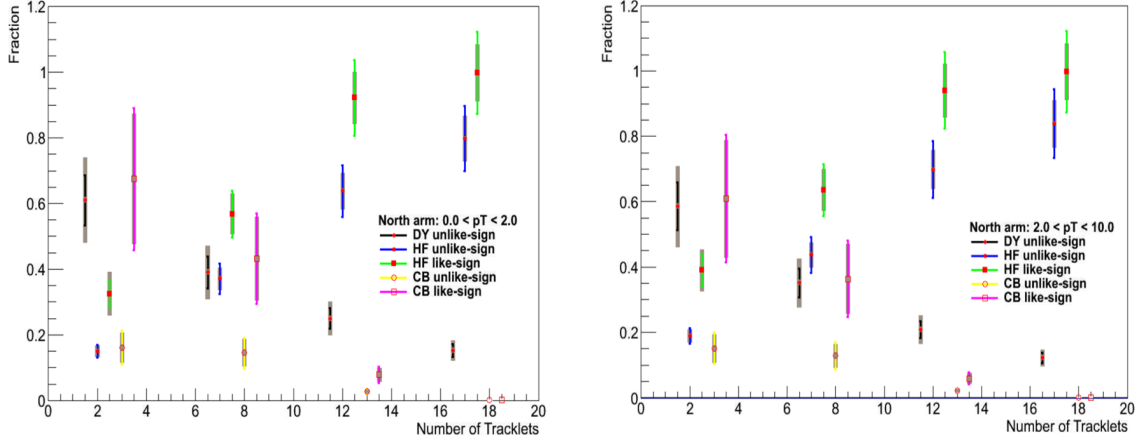


Figure 6.3: North arm signal and background fractions for four tracklet regions ($0-5$, $5-10$, $10-15$ and $15-50$) for tracklets vs. pT case.

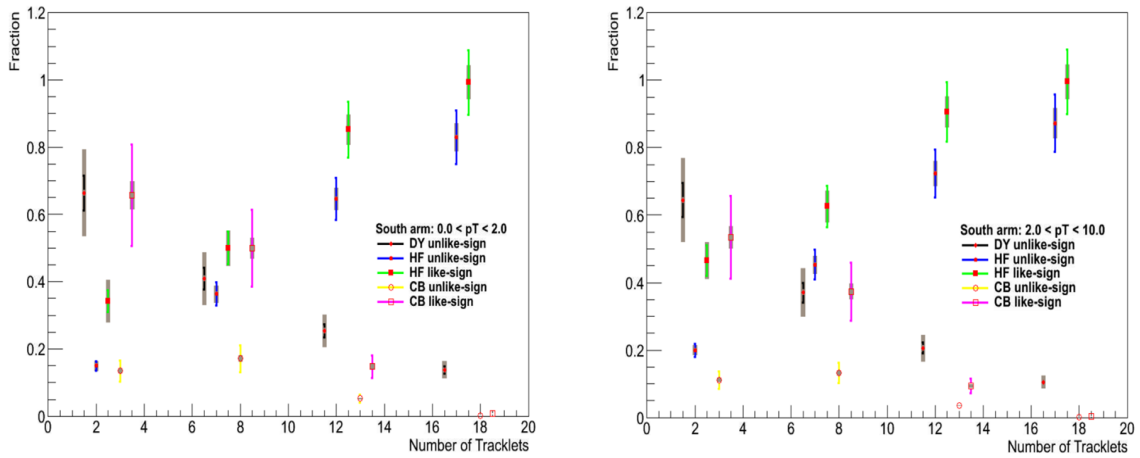


Figure 6.4: South arm signal and background fractions for four tracklet regions ($0-5$, $5-10$, $10-15$ and $15-50$) for tracklets vs. pT case.

Section 5.5.

In both tracklets vs. mass and tracklets vs. pT cases, it was assumed that the template functions which were determined from the simulations correctly represent the actual shapes of the 2-D distributions of signal and backgrounds.

6.2 Measuring longitudinal double spin asymmetry

As discussed in Section 1.3.4, A_{LL} for longitudinally polarized proton-proton collisions is defined in terms of yield as:

$$A_{LL} = \frac{1}{P_B P_Y} \frac{N_{++} - RN_{+-}}{N_{++} + RN_{+-}} \quad (6.1)$$

where P_B and P_Y are the polarization of the two beams and R is the relative luminosity between like (++) and unlike (+-) helicity crossings.

6.2.1 Inclusive double spin asymmetry

The asymmetry that is found from the dimuon data which consists of signal as well as the backgrounds is called the “inclusive asymmetry”. As mentioned at the beginning of this chapter, the inclusive asymmetry for each tracklet region for given mass (and pT) bin was found. For this analysis, the inclusive double spin asymmetry can be decomposed into the contributions of signal asymmetry and background asymmetries as follows.

$$A_{LL}^{inc} = F_{DY} \cdot A_{LL}^{DY} + F_{hf} \cdot A_{LL}^{hf} + F_{comb} \cdot A_{LL}^{comb} + F_{\psi'} \cdot A_{LL}^{\psi'} \quad (6.2)$$

$F_{process}$ stands for the fraction of each process. Since ψ' is an excited state of the J/ψ resonance, it was assumed that the ψ' have the same longitudinal double spin asymmetry as the J/ψ . PHENIX J/ψ longitudinal double spin asymmetry measurements [60] for Run 13 are shown in Figure 6.5. Therefore, we could

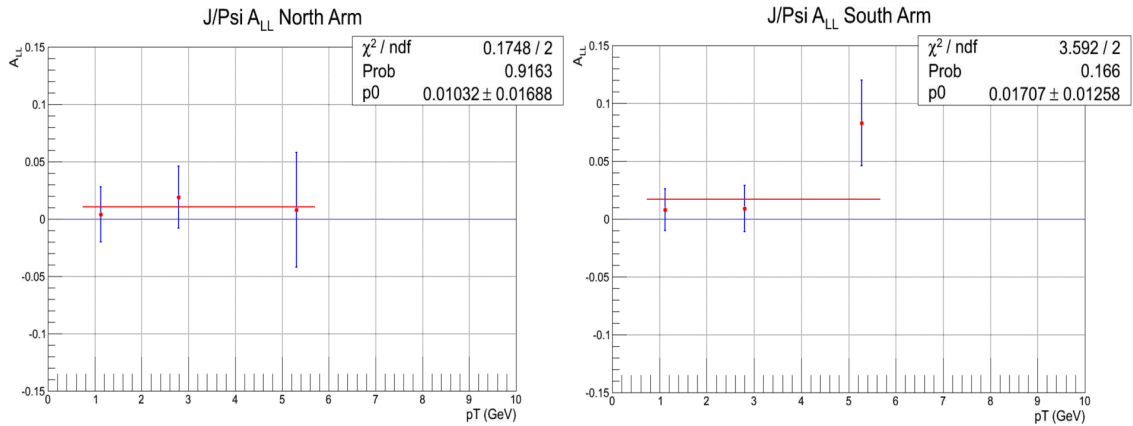


Figure 6.5: PHENIX Measurement of the J/ψ A_{LL} from Run 13 Data [60]

remove the ψ' contribution to the inclusive asymmetry from the Equation 6.2. The inclusive asymmetries before and after removing the ψ' contribution are given in Table 6.1 and Table 6.2.

US and LS stands for unlike-sign and like-sign events. It can be seen that the ψ' fraction for most of the bins are negligible and therefore its effect for the asymmetry measurement is very small. For tracklets vs. pT case the fraction of ψ' is set constant. The uncertainties of the inclusive asymmetries are very large due to the lack of statistics.

Table 6.1: Inclusive asymmetries for north arm for tracklets vs. mass case.

Mass (GeV)	Charge	Tracklet Cut	$F_{\psi'}$	A_{LL}^{inc}	$A_{LL}^{new inc}$
4.5-5.0	US	0 to 5	0.227 ± 0.071	-0.051 ± 0.702	-0.053 ± 0.702
4.0-5.0	LS	0 to 5	0.000 ± 0.000	0.968 ± 0.759	0.968 ± 0.759
4.5-5.0	US	5 to 10	0.213 ± 0.067	0.164 ± 0.551	0.162 ± 0.551
4.0-5.0	LS	5 to 10	0.000 ± 0.000	-1.241 ± 0.567	-1.241 ± 0.567
4.5-5.0	US	10 to 15	0.186 ± 0.058	-0.050 ± 0.686	-0.052 ± 0.686
4.0-5.0	LS	10 to 15	0.000 ± 0.000	0.984 ± 0.650	0.984 ± 0.650
4.5-5.0	US	15 to 50	0.122 ± 0.038	0.134 ± 0.967	0.132 ± 0.967
4.0-5.0	LS	15 to 50	0.000 ± 0.000	1.307 ± 0.841	1.307 ± 0.841
5.0-8.0	US	0 to 5	0.000 ± 0.000	0.244 ± 0.512	0.244 ± 0.512
5.0-8.0	LS	0 to 5	0.000 ± 0.000	0.122 ± 0.953	0.122 ± 0.953
5.0-8.0	US	5 to 10	0.000 ± 0.000	-0.450 ± 0.476	-0.450 ± 0.476
5.0-8.0	LS	5 to 10	0.000 ± 0.000	0.775 ± 0.817	0.775 ± 0.817
5.0-8.0	US	10 to 15	0.000 ± 0.000	0.108 ± 0.450	0.108 ± 0.450
5.0-8.0	LS	10 to 15	0.000 ± 0.000	-0.937 ± 0.908	-0.937 ± 0.908
5.0-8.0	US	15 to 50	0.000 ± 0.000	-2.151 ± 0.663	-2.151 ± 0.663
5.0-8.0	LS	15 to 50	0.000 ± 0.000	-0.601 ± 1.094	-0.601 ± 1.094

Table 6.2: Inclusive asymmetries for south arm for tracklets vs. mass case.

Mass (GeV)	Charge	Tracklet Cut	$F_{\psi'}$	A_{LL}^{inc}	$A_{LL}^{new inc}$
4.5-5.0	US	0 to 5	0.139 ± 0.049	-0.489 ± 0.601	-0.491 ± 0.601
4.0-5.0	LS	0 to 5	0.000 ± 0.000	0.837 ± 0.582	0.837 ± 0.582
4.5-5.0	US	5 to 10	0.135 ± 0.047	0.464 ± 0.421	0.461 ± 0.421
4.0-5.0	LS	5 to 10	0.000 ± 0.000	-0.059 ± 0.436	-0.059 ± 0.436
4.5-5.0	US	10 to 15	0.110 ± 0.039	-0.928 ± 0.487	-0.930 ± 0.487
4.0-5.0	LS	10 to 15	0.000 ± 0.000	-0.216 ± 0.446	-0.216 ± 0.446
4.5-5.0	US	15 to 50	0.067 ± 0.024	0.359 ± 0.631	0.358 ± 0.631
4.0-5.0	LS	15 to 50	0.000 ± 0.000	-0.159 ± 0.580	-0.159 ± 0.580
5.0-8.0	US	0 to 5	0.000 ± 0.000	0.180 ± 0.390	0.180 ± 0.390
5.0-8.0	LS	0 to 5	0.000 ± 0.000	-0.322 ± 0.807	-0.322 ± 0.807
5.0-8.0	US	5 to 10	0.000 ± 0.000	-0.060 ± 0.304	-0.060 ± 0.304
5.0-8.0	LS	5 to 10	0.000 ± 0.000	-0.606 ± 0.533	-0.606 ± 0.533
5.0-8.0	US	10 to 15	0.000 ± 0.000	0.251 ± 0.355	0.251 ± 0.355
5.0-8.0	LS	10 to 15	0.000 ± 0.000	0.616 ± 0.603	0.616 ± 0.603
5.0-8.0	US	15 to 50	0.000 ± 0.000	0.388 ± 0.477	0.388 ± 0.477
5.0-8.0	LS	15 to 50	0.000 ± 0.000	-0.684 ± 0.676	-0.684 ± 0.676

Table 6.3: Inclusive asymmetries for north arm for tracklets vs. pT case.

pT (GeV)	Charge	Tracklet Cut	$F_{\psi'}$	A_{LL}^{inc}	$A_{LL}^{new \ inc}$
0.0-2.0	US	0 to 5	0.084	0.929 ± 0.648	0.928 ± 0.648
0.0-2.0	LS	0 to 5	0.000	0.766 ± 1.215	0.766 ± 1.215
0.0-2.0	US	5 to 10	0.095	0.042 ± 0.483	0.041 ± 0.483
0.0-2.0	LS	5 to 10	0.000	0.721 ± 0.898	0.721 ± 0.898
0.0-2.0	US	10 to 15	0.084	0.902 ± 0.621	0.902 ± 0.621
0.0-2.0	LS	10 to 15	0.000	-0.835 ± 1.052	-0.835 ± 1.052
0.0-2.0	US	15 to 50	0.047	-0.740 ± 0.808	-0.740 ± 0.808
0.0-2.0	LS	15 to 50	0.000	0.013 ± 1.221	0.013 ± 1.221
2.0-10.0	US	0 to 5	0.079	-0.381 ± 0.556	-0.383 ± 0.556
2.0-10.0	LS	0 to 5	0.000	0.287 ± 1.057	0.287 ± 1.057
2.0-10.0	US	5 to 10	0.085	-0.342 ± 0.552	-0.343 ± 0.552
2.0-10.0	LS	5 to 10	0.000	-0.554 ± 0.861	-0.554 ± 0.861
2.0-10.0	US	10 to 15	0.070	-0.569 ± 0.535	-0.570 ± 0.535
2.0-10.0	LS	10 to 15	0.000	-0.236 ± 0.989	-0.236 ± 0.989
2.0-10.0	US	15 to 50	0.038	-2.105 ± 0.759	-2.106 ± 0.759
2.0-10.0	LS	15 to 50	0.000	0.001 ± 1.251	0.001 ± 1.251

Table 6.4: Inclusive asymmetries for south arm for tracklets vs. pT case.

pT (GeV)	Charge	Tracklet Cut	$F_{\psi'}$	A_{LL}^{inc}	$A_{LL}^{new \ inc}$
0.0-2.0	US	0 to 5	0.056	-0.365 ± 0.477	-0.365 ± 0.477
0.0-2.0	LS	0 to 5	0.000	-0.722 ± 0.910	-0.722 ± 0.910
0.0-2.0	US	5 to 10	0.056	0.298 ± 0.354	0.298 ± 0.354
0.0-2.0	LS	5 to 10	0.000	-0.433 ± 0.627	-0.433 ± 0.627
0.0-2.0	US	10 to 15	0.047	-0.175 ± 0.405	-0.175 ± 0.405
0.0-2.0	LS	10 to 15	0.000	-0.271 ± 0.666	-0.271 ± 0.666
0.0-2.0	US	15 to 50	0.029	-0.219 ± 0.551	-0.219 ± 0.551
0.0-2.0	LS	15 to 50	0.000	-1.392 ± 0.753	-1.392 ± 0.753
2.0-10.0	US	0 to 5	0.047	0.306 ± 0.462	0.306 ± 0.462
2.0-10.0	LS	0 to 5	0.000	2.055 ± 0.810	2.055 ± 0.810
2.0-10.0	US	5 to 10	0.045	-0.080 ± 0.348	-0.080 ± 0.348
2.0-10.0	LS	5 to 10	0.000	-0.241 ± 0.571	-0.241 ± 0.571
2.0-10.0	US	10 to 15	0.034	0.055 ± 0.415	0.055 ± 0.415
2.0-10.0	LS	10 to 15	0.000	1.203 ± 0.618	1.203 ± 0.618
2.0-10.0	US	15 to 50	0.020	0.969 ± 0.526	0.969 ± 0.526
2.0-10.0	LS	15 to 50	0.000	-0.202 ± 0.751	-0.202 ± 0.751

6.2.2 Drell-Yan A_{LL}

After removing the ψ' contribution from the inclusive asymmetry, the new inclusive asymmetry can be written as:

$$A_{LL}^{new \ inc} = F_{dy} \cdot A_{LL}^{DY} + F_{hf} \cdot A_{LL}^{hf} + F_{comb} \cdot A_{LL}^{comb} \quad (6.3)$$

And also,

$$F_{dy} + F_{hf} + F_{comb} + F_{\psi'} = 1 \quad (6.4)$$

After removing $F_{\psi'}$ and rescaling F_{dy} , F_{hf} , F_{comb} to sum to 1 again, the $A_{LL}^{new \ inc}$ can be written as

$$A_{LL}^{new \ inc} = (1 - F_{hf} - F_{comb}) \cdot A_{LL}^{DY} + F_{hf} \cdot A_{LL}^{hf} + F_{comb} \cdot A_{LL}^{comb} \quad (6.5)$$

Therefore, Equation 6.5 was used to find the physics asymmetry values for the Drell-Yan and background processes for each mass/pT bin. First the new inclusive asymmetry values were plotted into a graph where x axis is heavy flavor fraction and the y axis is the combinatorial fraction as shown in Figure 6.6. Then the function in Equation 6.5 was used to fit the $A_{LL}^{new \ inc}$ values and determined the A_{LL}^{dy} , A_{LL}^{hf} and A_{LL}^{comb} from the function coefficients.

The fitting results are shown in Table 6.5 and Table 6.6. Measured physics asymmetry values for Drell-Yan process for north arm and south arm are shown in Figure 6.7 in two mass bins and Figure 6.8 in two pT bins. The final asymmetry value is shown for both tracklets vs. mass and tracklets vs. pT cases in Figure 6.9.

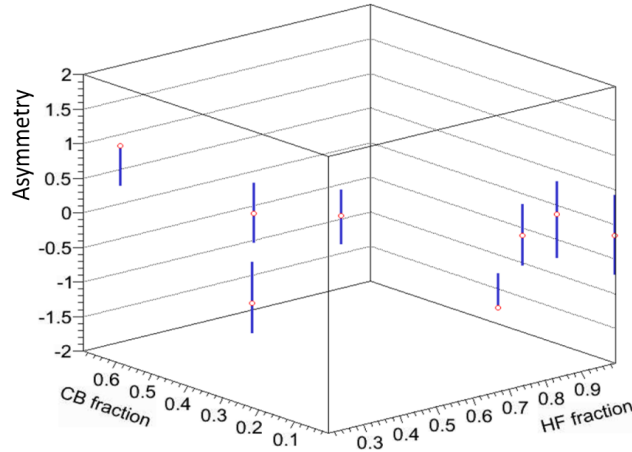


Figure 6.6: Asymmetry values plotted in to a graph where x axis is heavy flavor fraction and y axis is combinatorial fraction for south arm (mass 4.5 - 5 GeV).

Table 6.5: Fitting results for asymmetry measurements for each process for each mass bin and each arm.

Arm	mass (GeV)	Process	χ^2/NDF	A_{LL}	Stat. Uncertainty
North	4.5 - 5.0	Drell-Yan	8.7/5	-0.35	1.15
	4.5 - 5.0	Heavy flavor	8.7/5	0.79	0.50
	4.5 - 5.0	Combinatorial	8.7/5	-0.76	0.74
South	4.5 - 5.0	Drell-Yan	6.1/5	-0.37	0.83
	4.5 - 5.0	Heavy flavor	6.1/5	-0.30	0.34
	4.5 - 5.0	Combinatorial	6.1/5	0.85	0.65
North	5.0 - 8.0	Drell-Yan	7.6/5	0.16	0.78
	5.0 - 8.0	Heavy flavor	7.6/5	-1.16	0.49
	5.0 - 8.0	Combinatorial	7.6/5	2.24	1.45
South	5.0 - 8.0	Drell-Yan	3.2/5	0.42	0.53
	5.0 - 8.0	Heavy flavor	3.2/5	0.15	0.33
	5.0 - 8.0	Combinatorial	3.2/5	-1.27	1.07

Table 6.6: Fitting results for asymmetry measurements for each process for each pT bin and each arm.

Arm	pT (GeV)	Process	χ^2/NDF	A_{LL}	Stat. Uncertainty
North	0.0 - 2.0	Drell-Yan	3.8/5	0.85	0.86
	0.0 - 2.0	Heavy flavor	3.8/5	-0.31	0.55
	0.0 - 2.0	Combinatorial	3.8/5	1.29	1.40
South	0.0 - 2.0	Drell-Yan	3.8/5	0.35	0.55
	0.0 - 2.0	Heavy flavor	3.8/5	-0.53	0.41
	0.0 - 2.0	Combinatorial	3.8/5	-0.29	0.96
North	2.0 - 10.0	Drell-Yan	3.9/5	-0.45	0.86
	2.0 - 10.0	Heavy flavor	3.9/5	-0.97	0.48
	2.0 - 10.0	Combinatorial	3.9/5	0.97	1.45
South	2.0 - 10.0	Drell-Yan	10.1/5	-0.29	0.59
	2.0 - 10.0	Heavy flavor	10.1/5	0.44	0.36
	2.0 - 10.0	Combinatorial	10.1/5	1.00	1.16

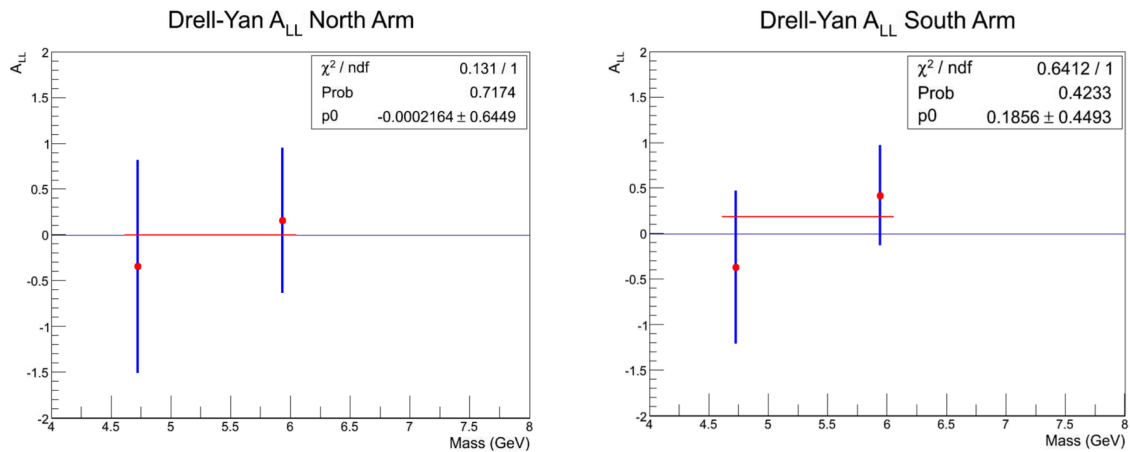


Figure 6.7: Drell-Yan A_{LL} in two mass bins

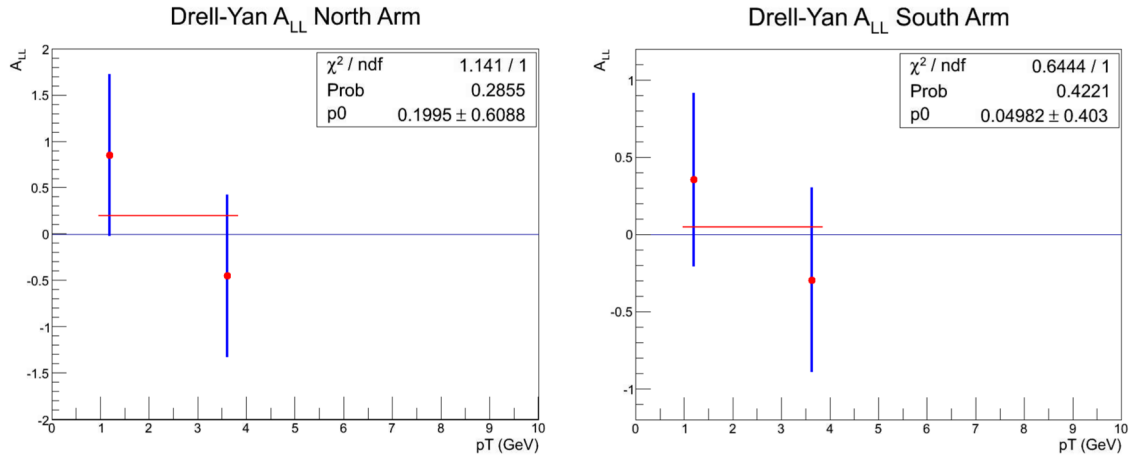


Figure 6.8: Drell-Yan A_{LL} in two pT bins

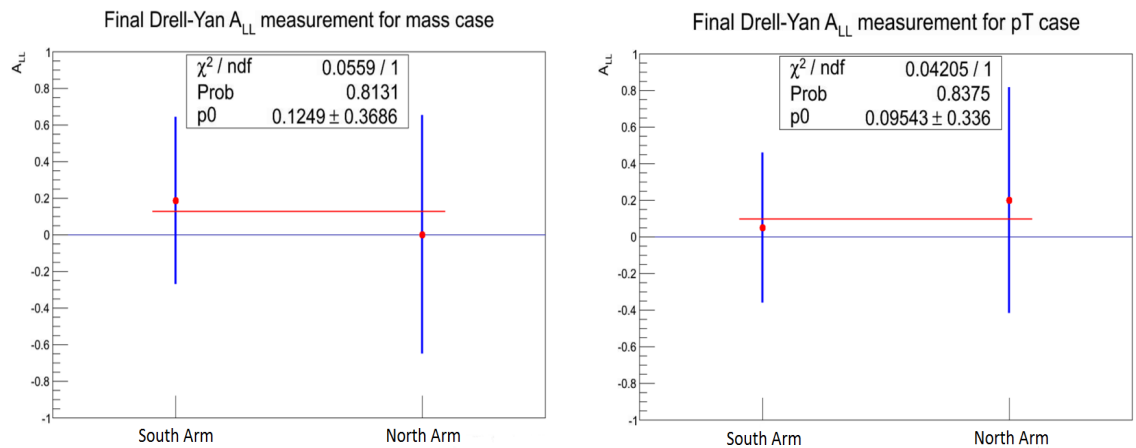


Figure 6.9: Drell-Yan A_{LL} after combining two bins for both methods

As a byproduct of the Drell-Yan A_{LL} measurement, the heavy flavor and combinatorial asymmetries were obtained and plotted in Figure 6.10 and Figure 6.11.

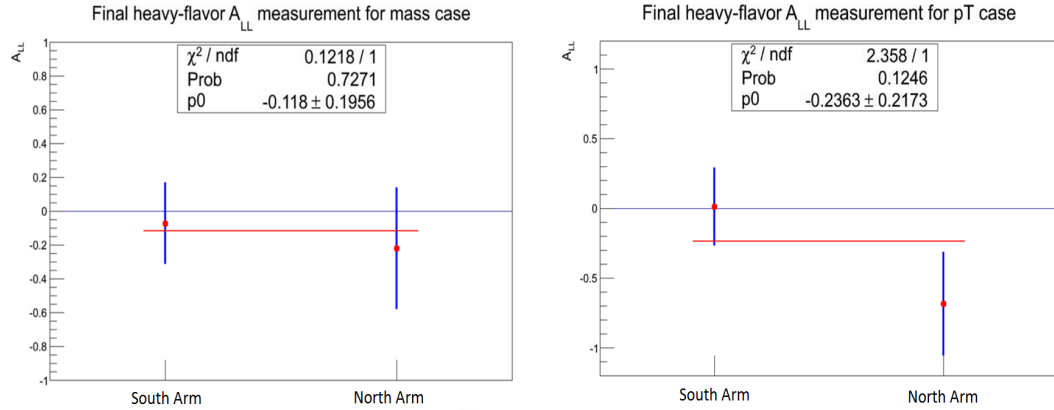


Figure 6.10: Heavy flavor background A_{LL} from two methods

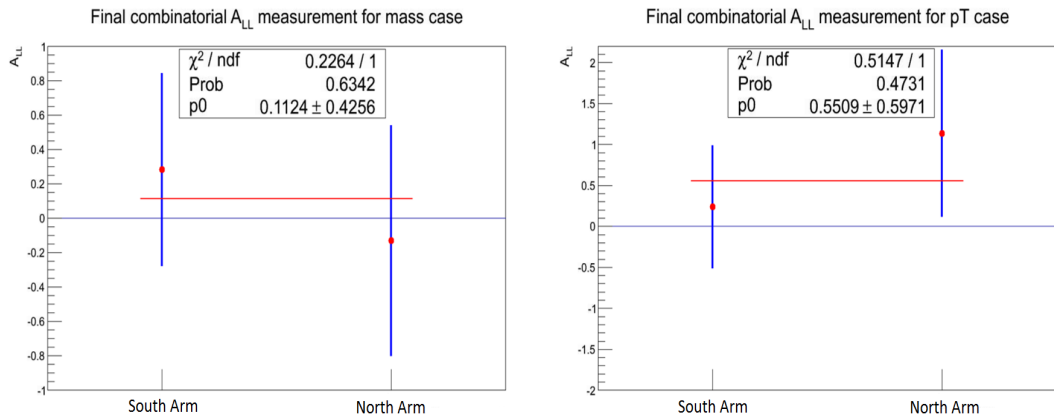


Figure 6.11: Combinatorial background A_{LL} from two methods

6.3 Systematic uncertainty and final results

There are many factors that could affect the systematic uncertainty of the Drell-Yan A_{LL} measurement. Among all of them, the largest contribution come from the uncertainties of signal and background fractions. In order to estimate the change of asymmetry due to the errors in fractions, the signal fractions in each region was changed by adding/subtracting the uncertainty (by one sigma) and measured the asymmetries. Similarly the background fractions were changed one at a time and observed the changed in asymmetries. The systematic uncertainty which can be existed due to the fractions was measured as 2.32×10^{-2} .

Further the simulation 2-D distribution shapes (template functions) also create an uncertainty on the signal and background fractions. The method to address this issue throughout this study was to estimate the uncertainty by comparing the Tracklet vs. Mass results with the Tracklet vs. pT results. The systematic uncertainty from using the mass as a variable in 2-D fitting was measured as 2.9×10^{-2} from this method. But these uncertainties are negligible when compared to the statistical uncertainty of the A_{LL} measurement.

One of the other sources for the systematic uncertainty comes from the variation of detector efficiency within a data group in which the asymmetry is calculated. In this analysis, all the fills were combined to a single set of data due to the shortage of enough statistics for fill by fill analysis. However this uncertainty

was also expected to be negligible when compared to the statistical uncertainty.

According to the Equation 6.6 other sources contributing to the systematic uncertainty are the relative luminosity R and the average beam polarizations, P_B and P_Y .

In this analysis, the BBC trigger counts with a vertex cut of 30 cm along the beam line was used to count the luminosity. In PHENIX, Zero Degree Calorimeter (ZDC) is used to check whether there is an unmeasured physics asymmetry in BBC count rate. A double spin asymmetry of the ZDC/BBC luminosity ratio is defined as:

$$A_{LL}^R = \frac{1}{P_B P_Y} \frac{r_{ZDC/BBC}^{++} - r_{ZDC/BBC}^{+-}}{r_{ZDC/BBC}^{++} + r_{ZDC/BBC}^{+-}} \quad (6.6)$$

where $r_{ZDC/BBC}^{++} = N_{ZDC}/N_{BBC}$.

A_{LL}^R and its statistical uncertainty is taken as a systematic uncertainty for the relative luminosity R which is mainly caused by spin dependence of the luminosity counter. A_{LL}^R is also corrected for event pileup, which is caused by having more than one p + p binary collision due to high beam intensity and random coincidences of single diffractive events where scaler over-counting or under-counting could occur. This systematic uncertainty was estimated as 4×10^{-3} when using raw scalars for Run 13 which is also negligible compared to the statistical uncertainty.

Further, for the RHIC 2013 data set, the systematic uncertainty from the aver-

age beam polarization was measured to be $6.5\% \times A_{LL}$ for all A_{LL} measurements.

After considering the systematic uncertainties, final Drell-Yan A_{LL} measurement can be given as

$$A_{LL}^{DY} = 0.12 \pm 0.37(\text{stat.}) \pm 0.04(\text{syst.}) \quad (6.7)$$

7 DISCUSSION AND CONCLUSIONS

RHIC has been one of the pioneering facility providing the measurements for determining the polarized parton distribution functions within the last decade.

J/ψ and π^0 asymmetry measurements at RHIC were used in constraining the gluon polarization (Δg) whereas the $W^{+/-}$ asymmetry measurements were used to constrain the sea quark polarization ($\Delta \bar{u}$ and $\Delta \bar{d}$). In this thesis, Drell-Yan longitudinal double spin asymmetry (A_{LL}^{DY}) which is another measurement to access the $\Delta \bar{u}$ in PHENIX experiment at RHIC is presented.

Drell-Yan production at PHENIX experiment in forward/backward rapidity regions in longitudinally polarized $p+p$ collisions at $\sqrt{s} = 510$ GeV was considered in this study. The invariant mass of the observed dimuon pair was between 4.5 GeV to 8 GeV. This is the fist measurement of Drell-Yan production at a polarized hadron collider experiment in the world. Further, this is the first asymmetry measurement at a new kinematic region of momentum fraction x , as low as 0.002, done in order to constrain the uncertainty on the \bar{u} polarization in polarized PDFs.

After the track quality cuts, the measured signal fraction in Run 13 dimuon data set for north arm was $0.26 \pm 0.03(stat.) \pm 0.07(syst.)$ and $0.27 \pm 0.03(stat.) \pm 0.06(syst.)$ for south arm. The total number of Drell-Yan events observed was ≈ 1100 . It can be seen that the results for two arms are consistent with each other and it was observed that the data was dominated by the heavy flavor backgrounds.

Drell-Yan A_{LL} after combining all the mass and tracklet bins to a single mass bins from 4.5 to 8 GeV was measured as $0.12 \pm 0.37(stat.) \pm 0.04(syst.)$. Since the statistics were limited, the statistical uncertainty dominates in this measurement.

However these measurements are made trusting the Monte Carlo simulation (PYTHIA6) shapes of mass and tracklet distributions for each kind of process. Hence the main source of the systematic uncertainty can be coming from the simulated distribution shapes. But the cross-check using the pT distributions instead of mass distribution showed a consistency of the results. And also simulated tracklet distributions could be trusted since the simulated tracklet distribution matched well with the data for the J/ψ process as discussed in section 3.5. Further, observing the change in the asymmetry when changing the signal fraction by its statistical and systematic uncertainties indicated only a slight change in the A_{LL}^{DY} value which is negligible when compared to its statistical uncertainty. However it is suggested to cross-check the results by generating the simulations using a different particle generator like MC@NLO.

In future it is possible to measure the A_{LL}^{DY} with a smaller uncertainty at PHENIX with the improvement of the polarization of the beams and the luminosity. Further, the template functions can be improved by obtaining more simulated events for each kind of process.

REFERENCES

- [1] R. Mann, An Introduction to Particle Physics and the Standard Model, Florida, USA: CRC Press (2010)
- [2] D. J. Griffiths, Introduction to Elementary Particles, New York, USA: Wiley (1987)
- [3] K. A. Olive et al. (Particle Data Group), Chin. Phys. C, 38, 090001 (2014)
- [4] J. Hauptman, Particle Physics Experiments at High Energy Colliders, Weinheim, Germany: Wiley-VCH (2011)
- [5] D. H. Perkins, Introduction to High Energy Physics, 4th ed., Cambridge, UK: Cambridge University Press (2000)
- [6] A. Bettini, Introduction to Elementry Particle Physics, 1st ed., Cambridge, UK: Cambridge University Press (2010)
- [7] R. Feynman, Phys. Lett. 23, 14151417 (Dec. 1969)
- [8] http://www.nobelprize.org/nobel_prizes/physics/laureates/1969/
- [9] http://www.nobelprize.org/nobel_prizes/physics/laureates/1990/
press.html
- [10] P. M. McKee, The Spin Structure of the Proton From SLAC Experiment E155, SLAC Report-622, (2000)
- [11] J. Gao et al., Phys. Rev. D 89, 033009 (Feb. 2014)

- [12] J. Ashman et al., Phys. Lett. B 206, 364370 (May 1988)
- [13] L. W. Alvarez, F. Bloch, Phys. Rev. 57, 111 ((1940))
- [14] M. Gell-Mann, Phys. Lett. 8, 214 (1964)
- [15] K. Nishijima, Prog. Theor. Phys. Vol. 13 No. 3 (1955) pp. 285-304
- [16] **(PDG2012)** J. Beringer et al., Phys. Rev. D86, 010001 (2012)
- [17] **(DSSV)** D. de Florian, et al. (DSSV), Phys. Rev. D80:034030 (2009)
- [18] COMPASS Collaboration, Phys. Lett. B690, 227-235 (Oct. 2010)
- [19] S. D. Drell and T. M. Yan, Phys. Rev. Lett. 25, 316 (1970)
- [20] Close F. E., Sivers D. Phys. Rev. Lett. 39:1116 (1977)
- [21] P. L. McGaughey et al. Annu. Rev. Nucl. Part. Sci., 49:217 (1999)
- [22] R. Feynman, Phys. Rev. Lett. 23, 1415 (1969)
- [23] J. D. Bjorken, Phys. Rev. 179, 1547 (1969)
- [24] R. P. Feynman, The Behavior of Hadron Collisions at Extreme Energies, New York, USA: Gordon & Breach (1969)
- [25] J. D. Bjorken, E. A. Paschos, Phys. Rev. 185, 1975 (1969)
- [26] A. Zelenski et al., Hyperfine Interactions 127, 475 (2000),
10.1023/A:1012682104479

- [27] **(PHENIX)** K. Adcox et al., NIM A499 469-479 (2003)
- [28] **(STAR)** K. Adcox et al., NIM A499 624-632 (2003)
- [29] **(PHOBOS)** B. Bak et al., NIM A499 437-468 (2003)
- [30] **(BRAHMS)** K. Adcox et al., NIM A499 603-623 (2003)
- [31] Y. S. Derbenev et al., Part. Accel. 8, 115 (1978)
- [32] S. R. Mane, et al., J. Phys. G: Nucl. Part. Phys. 31 (2005) R151-R209
- [33] M Anerella et al., Nucl. Instrum. Meth. A 499, 280315 (Mar. 2003)
- [34] S. H. Lee, “Thesis”, (2013)
<https://www.phenix.bnl.gov/phenix/WWW/publish/shlee/ThesisSHLEE.pdf>
- [35] M. Kim, RIKEN Accel. Prog. Rep. 48(2015), <http://www.rarf.riken.jp/researcher/APR/APR048/pdf/102.pdf>
- [36] O. Jinnouchi et al., RHIC/CAD Accelerator Physics Note 171 (2004)
- [37] H. Okada et al., Phys. Lett. B638, 450 (2006), nucl-ex/0502022
- [38] A. Zelenski et al., Nucl. Instrum. Meth., vol. A 536, pp. 248-254 (2005)
- [39] K. O. Eyser et al., presented at the AIP Conference Proceedings, vol. 915, pp. 916919, arXiv:0612020v1 [arXiv:nucl-ex]
- [40] C. Aidla, Measurement of the Transverse Single-Spin Asymmetry for Mid-rapidity Production of Neutral Pions in Polarized p+p Collisions at 200 GeV Center-of-Mass Energy (Doctoral dissertation). Columbia University (2006)

- [41] http://www.phenix.bnl.gov/WWW/muon/design_books/mutr_design/nomenclature.html
- [42] V. Dzhordzhadze, MuID for the PHENIX Experiment, WWW Seminar Document
https://www.phenix.bnl.gov/WWW/intro/detectors/focus/focus_muid.pdf
- [43] A. Meles, “Thesis”, (2014) <https://www.phenix.bnl.gov/phenix/WWW/publish/abraham1/MelesThesis.pdf>
- [44] A. Key, “Thesis”, (2014) http://physics.unm.edu/Fields/group/Key_dissertation.pdf
- [45] H. Oide, “Thesis”, (2012) https://www.phenix.bnl.gov/phenix/WWW/talk/archive/theses/2013/Oide_Hideyuki-thesis.pdf
- [46] B. Hong, Nucl. Instrum. Meth., vol. A 602, pp. 644648 (2009)
- [47] S. S. Adler et al., Nucl. Instrum. Meth. A 499 560-592 (2003)
- [48] S. S. Adler et al., Nucl. Instrum. Meth. A 499 593-602 (2003)
- [49] A. Airapetian et al., Phys. Rev. D 71, 012003 (2005)
- [50] A. Taketani et al., Nucl. Instrum. Meth. A 623, 374376 (2010)
- [51] C. Aidala et al., Nucl. Instrum. Meth. A 755, 4461 (2014)
- [52] <http://www.opensciencegrid.org>
- [53] The PHENIX Collaboration, PHENIX Beam Use Proposal for RHIC Run-13 and Run-14 (May 2012)

- [54] RHIC Spin Group, “Polarimetry-H-jet-Run13”,
<https://wiki.bnl.gov/rhicspin/Polarimetry/H-jet/Run13>
- [55] **(PHENIX)**M. Beaumier, C. Gal, M. Kim, S. Park, R. Seidl, I. Yoon., “Run 13 Spin Database Quality Assurance”, the PHENIX collaboration analysis note No. 1125 (2014)
- [56] T. Sjöstrand, S. Mrenna, and P. Z. Skands, PYTHIA 6.4 Physics and Manual”, JHEP, vol. 05, p. 026 (2006)
- [57] P. V. C. Hough, Method and means for recognizing complex patterns. U.S. Patent 3,069,654, Dec. 18 (1962)
- [58] R. O. Duda, P. E. Hart, Communications of the ACM 15, 1115 (Jan. 1972)
- [59] S. S. Adler et al., Nucl. Instrum. Meth. A 499 593-602 (2003)
- [60] **(PHENIX)** H. Yu, J. Huang, M. Liu, X. Wang, Double Helicity Asymmetry in J/ψ Production in Polarized p+p Collisions at $\sqrt{s} = 510$ GeV in Run13, the PHENIX collaboration analysis note No. 1194 (2016)